

Nanostructured Diluted Magnetic Semiconductors within Mesoporous Silica

DISSERTATION

zur Erlangung des
Doktorgrades

des Fachbereichs
Biologie, Chemie und
Geowissenschaften

der Justus-Liebig-
Universität Gießen

vorgelegt von

Felix Brieler

aus Kiel

Gießen, Juni 2005

Die vorliegende Arbeit entstand in der Zeit vom 1. März 2000 bis 31. März 2001 am Institut für Anorganische und Angewandte Chemie der Universität Hamburg und in der Zeit vom 1. April 2001 bis 24. Juni 2005 am Institut für Anorganische und Analytische Chemie der Justus-Liebig-Universität Gießen in der Arbeitsgruppe von Prof. Dr. Michael Fröba.

Gutachter:
Prof. Dr. Michael Fröba
Prof. Dr. Siegfried Schindler

Hiermit versichere ich, die vorliegende Arbeit eigenständig und ausschließlich unter Verwendung der angegebenen Hilfsmittel und Quellen durchgeführt zu haben. Die Arbeit wurde zuvor keiner Prüfungsbehörde in gleicher oder ähnlicher Form vorgelegt.

Gießen, 28. Juni 2005

Felix Brieler

Nothing is impossible – not if you can imagine it.
That's what being a scientist is all about.

Prof. Hubert J. Farnsworth, *Like Father, like Clone*

Contents

1. Introduction	1
1.1. Mesoporous silica	1
1.2. Semiconductor nanoparticles	7
1.2.1. Chemistry in confined spaces	7
1.2.2. Nanostructured diluted magnetic semiconductors.....	9
1.3. Aim of this work.....	13
2. Experimental.....	15
2.1. Synthesis of mesoporous host structures	15
2.1.1. Synthesis of MCM-41 silica (3 nm pores)	15
2.1.2. Synthesis of SBA-15 silica (6 and 9 nm pores).....	15
2.2. Synthesis of DMS compounds within mesoporous hosts.....	16
2.3. Characterisation methods.....	18
2.3.1. Powder X-ray diffraction (P-XRD)	18
2.3.2. Physisorption measurements	18
2.3.3. Transmission electron microscopy (TEM).....	20
2.3.4. X-ray absorption spectroscopy (XAS)	21
2.3.5. Infrared and Raman spectroscopy.....	22
2.3.6. Photoluminescence spectroscopy (PL/PLE)	23
2.3.7. Electron paramagnetic resonance spectroscopy (EPR).....	26
3. Results	32
3.1. Mesoporous host structures.....	32
3.1.1. Powder X-ray diffraction	32
3.1.2. Nitrogen physisorption.....	34

3.1.3.	Transmission electron microscopy	40
3.1.4.	Conclusions	41
3.2.	Host/guest compounds.....	42
3.2.1.	Powder X-ray diffraction	42
3.2.2.	Nitrogen physisorption.....	44
3.2.3.	Transmission electron microscopy	48
3.2.4.	Infrared spectroscopy	50
3.2.5.	Raman spectroscopy	51
3.2.6.	X-ray absorption spectroscopy	56
3.2.7.	Band gap and optical properties	62
3.2.8.	Magnetic properties of nanostructured DMS compounds.....	72
3.2.9.	Magnetic properties of nanostructured binary MnS	92
3.2.10.	Conclusions	98
4.	Summary	100
5.	Zusammenfassung (German summary).....	105
6.	References	110
	Appendix.....	118

1. Introduction

Porous materials play a special role in material science because of their wide applicability in size- and shape-selective applications. The IUPAC nomenclature divides porous substances into three different classes: materials with micropores (< 2 nm), mesopores (2-50 nm) and macropores (> 50 nm) [1]. The most prominent members from the group of microporous substances are zeolites, in the synthesis of which single, solvated organic molecules or ions act as templates for the formation of a regular arrangement of micropores with a narrow pore size distribution and with crystalline pore walls. In the macroporous region porous gels and glasses with much broader pore size distributions are known. The gap between micro- and macropores was closed when researchers of Mobil Oil Company reported the synthesis of mesoporous materials with a narrow pore size distribution by using self-assembled arrays of amphiphilic molecules (lyotropic liquid crystals) as structure directing agents^a (SDAs) [2,3]. Their removal leads to mesoporous solids with adjustable pore sizes ranging from 2 to 10 nm. The very regular pore arrangements and narrow pore size distributions of these new materials, denoted as M41S phases, are almost comparable to microporous zeolites [4]. Due to their larger pores and high surface areas these new materials are of great interest for different fields of materials science, such as catalysis [5-7], sorption [8-15] or host/guest chemistry [16].

1.1. Mesoporous silica

The original concept for the synthesis of mesoporous silica was based on an electrostatic templating route where the cationic long-chain tetraalkylammonium micelles (S^+) act as structure directors for the anionic inorganic precursors (I^-) on the mesoscopic scale. This assembly, which is driven by electrostatic and steric interactions

^a A template leads to one particular, structurally unique (crystalline) product while a structure directing agent gives one or more periodically ordered, but usually amorphous structures with respect to the short-range atomic structure.

leading to charge-matching at the organic-inorganic interface, was extended to further combinations of ion pairs, including charge-reversed (ST^+) and counter-ion mediated (S^+XT^+ and $S^-X^+I^-$) synthetic pathways [17,18]. To change the charge of the inorganic building blocks, the pH of the synthesis mixture has to be changed from basic (I^- , MCM-materials^a) to acidic conditions (I^+ , SBA-materials^b). Also neutral surfactants (S^0), like primary long-chain (C_8 to C_{18}) alkylamines, can be utilised to form mesopores in a neutral (pH = 7) synthesis with neutral inorganic precursors (I^0 , HMS^c-materials) [19], or non-ionic surfactants (N^0), like different polyethylene oxides (PEO), can be used as SDAs in a synthesis procedure based on hydrogen bonding interactions between the SDA and the inorganic precursor (I^0 , MSU-materials^d) [20]. The utilisation of polymers finally lead to a new material denoted as SBA-15 with pore sizes of up to 30 nm [21]. In contrast to the strong ionic interaction in the electrostatic templating route, the neutral and the non-ionic surfactants interact with the inorganic building blocks via weak hydrogen bonds. Compared to electrostatically templated mesoporous silica, these materials exhibit thicker framework walls, smaller X-ray scattering domain sizes and substantially improved mesoporosity.

In the synthesis procedure of SBA-15 so-called Pluronics^e were used as SDAs. Pluronics are triblock copolymers, consisting of two blocks of polyethylene oxide (PEO) and, in between these two, one block of polypropylene oxide (PPO), resulting in a $PEO_x-PPO_y-PEO_x$ polymer. The PEO parts of the block copolymer are more hydrophilic than the PPO part, therefore the whole polymer is capable of building micelles in solution. Many different compositions of the PEO and PPO blocks are possible, resulting in a variety of Pluronics with different properties in terms of *e.g.* solubility or aggregate state. In *Figure 1-1* different types of Pluronics are compiled in the so called "Pluronic-grid" of the BASF corporation. Depending on the length of the building blocks x and y , different aggregate states of the resulting polymer are possible. For a typical synthesis of SBA-15 silica Pluronic P-123 is most commonly used. The

^a MCM stands for *Mobils Composition of Matter*.

^b SBA stands for *Santa Barbara*.

^c HMS stands for *Hexagonal Mesoporous Silica*.

^d MSU stands for *Michigan State University*.

^e Pluronic[®] is a registered trademark of the BASF company.

first two digits (or first digit in a two-digit number) in the numerical designation, multiplied by 300, indicates the approximate molecular weight of the hydrophobe part (vertical axis at the left of the grid). The last digit, when multiplied by 10, indicates the approximate ethylene oxide content in the molecule, read from the horizontal axis. Pluronic P-123 therefore consists of 30 % PEO and the PPO part has a molecular weight of 3600 g/mol.

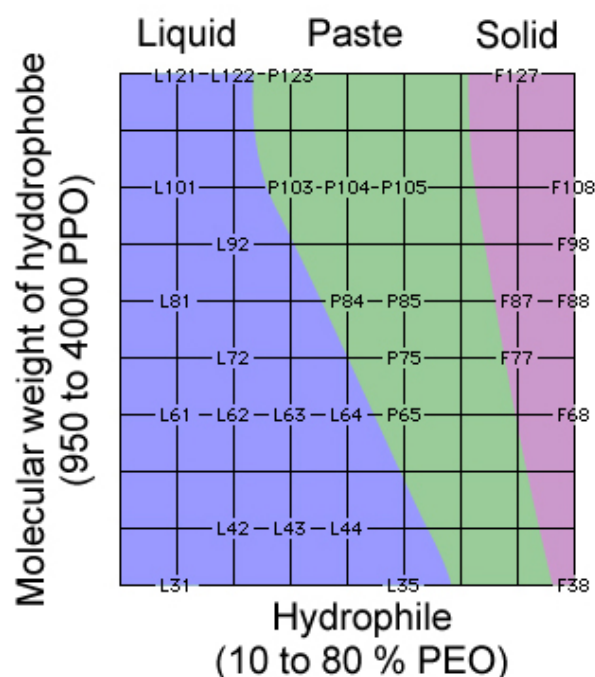


Figure 1-1: Pluronic-grid, © BASF corporation.

Extended information and a more comprehensive description on the variety of different synthetic pathways for mesoporous materials were given in various publications within the last years [5,6,16,22-29].

Originally, the M41S family was divided into three subgroups: a hexagonal (space group $p6mm$, MCM-41), a cubic (space group $Ia3d$, MCM-48) and a lamellar phase (MCM-50). MCM-50 cannot be obtained in a porous form, because the separated layers collapse upon surfactant removal. Only the other two structures yield stable porous materials after solvent extraction or thermal decomposition (calcination) of the SDA. Since the first report from 1992, a variety of other periodic structures have been

synthesised: 2D hexagonal ($p6mm$) FSM-16^a [30], SBA-3 [18,31], and SBA-15 (in which the mesopores are additionally interconnected by micropores) [32]; cubic ($Pm3n$) SBA-1 [18]; cubic ($Pm3m$) SBA-11 [33]; cubic ($Im3m$) SBA-16 [33,34]; 3D hexagonal ($P6_3/mmc$) SBA-2 [31] and other structures. *Figure 1-2* gives a comparison of some of these structures.

The hexagonal MCM-41 silica phase with its one-dimensional channel system is a promising host structure for the formation of nanoparticles or even nanowires [35], whereas the cubic MCM-48 silica phase with its three-dimensional pore system is a very interesting matrix to immobilise catalytically active species [36].

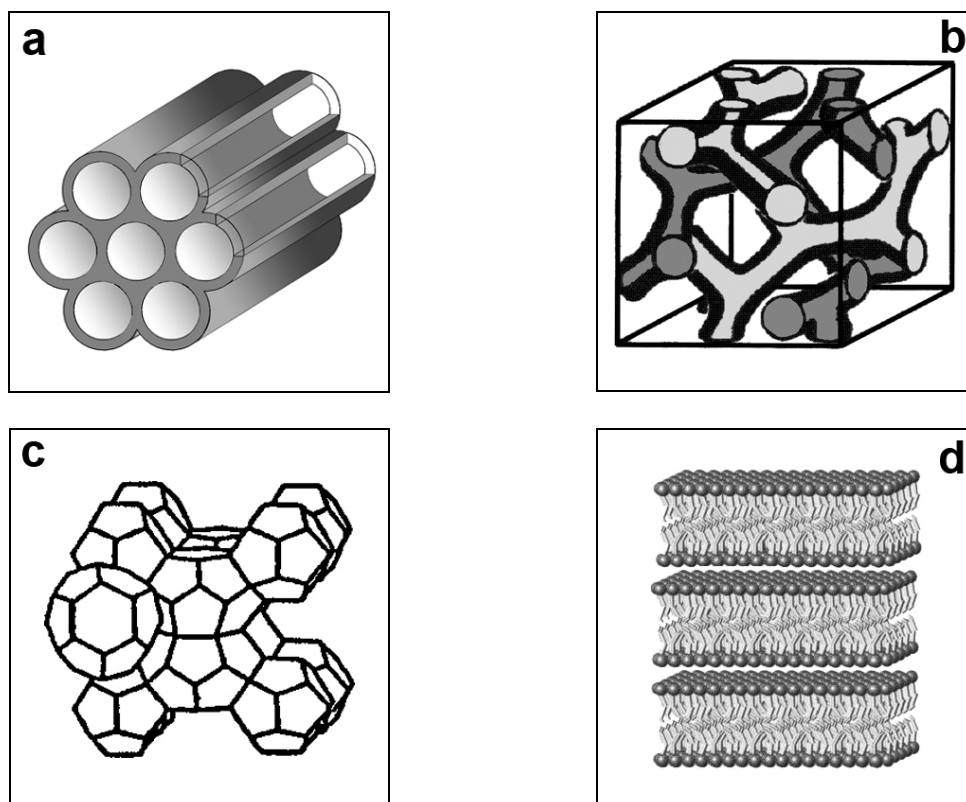


Figure 1-2: Comparison of different phases observed in mesoporous materials. a) 2D-hexagonal ($p6mm$, MCM-41, FSM-16, SBA-3 and SBA-15), b) cubic ($Ia3d$, MCM-48), c) cubic ($Pm3n$, SBA-1) and d) lamellar (MCM-50).

A mechanism for the electrostatic templating route of mesoporous materials was proposed in 1995 as so-called "cooperative templating" (CT) mechanism [37] and is shown as a scheme in *Figure 1-3*. Starting from a solution of surfactant molecules

^a FSM stands for *Folded Sheet Mechanism*.

(which may be present as single solvated molecules or micelles) and another solution of the inorganic precursor (A) an ion exchange occurs upon mixing the two solutions. Ion pairs, consisting of inorganic anions and surfactant cations, are formed (B). After a self-organisation process in which larger aggregates and finally a lyotropic liquid crystal are formed, condensation of the inorganic precursor takes place (C). The properties of the surfactant in solution are considerably altered due to the presence of different anions. In case of the hexadecyltrimethylammonium bromide (cetyltrimethylammonium bromide, CTAB) – the commonly used surfactant in the first syntheses – the bromide is exchanged for anionic silicate species during the synthesis. The fact that the mesostructures can be synthesised with surfactant concentrations far below the critical micelle concentration (cmc) shows the strong influence of the inorganic species [38,39].

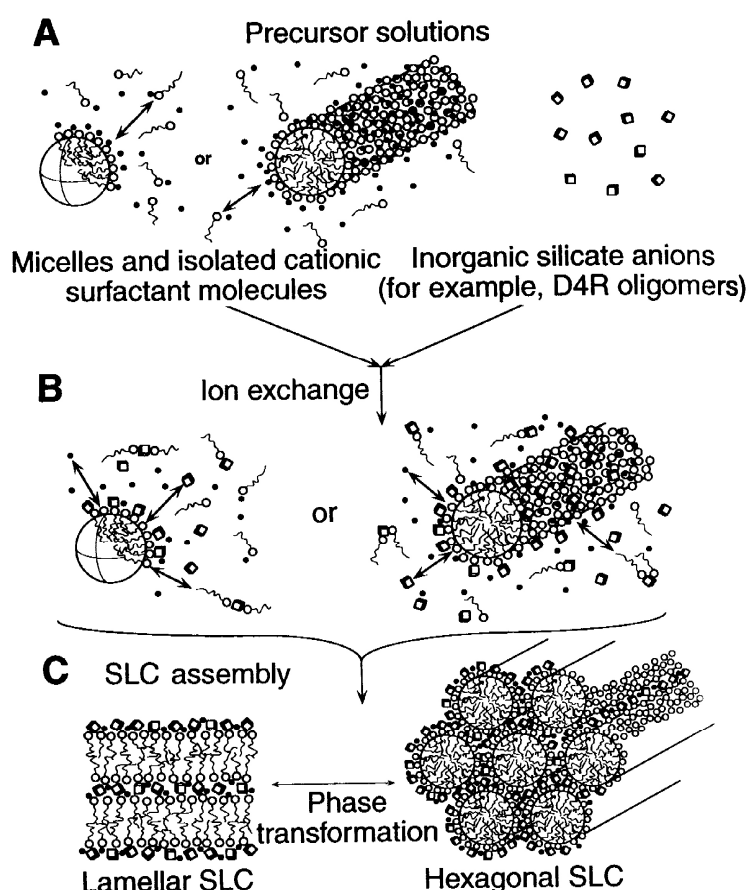


Figure 1-3: "Cooperative templating" (CT) mechanism [37].

An alternative synthesis for preparing mesoporous silica was described in 1990 before the syntheses of the M41S phases were published [40]. This synthesis utilised the

layered silicate kanemite, which consists of single layers of SiO_4 tetrahedra. The surfactants molecules are intercalated between the galleries of the layers ("folded sheet mechanism"), hence transforming this material into the mesostructured material [30,41]. A so-called "true liquid crystal templating" route was described in 1995, when Attard et al. used a surfactant solution with a much higher concentration, so that the liquid crystalline phase had already formed before the addition of the inorganic precursor was carried out. This lyotropic liquid crystal then serves as the actual structure director. After hydrolysis and condensation of the inorganic building blocks, an inorganic solid which is a direct moulding of the structure of the surfactant molecules is obtained [42].

One interesting point in the synthesis of mesoporous materials is the fact that the pore size can be controlled very easily just by varying the nature of the structure directing agent (SDA). At first, in the syntheses of the M41S family long-chain tetraalkylammonium halides were used as SDAs. By varying the chain length of the hydrophobic alkyl group (usually containing 12 to 22 carbon atoms) the pore size can be altered very precisely in the range of about 1 nm [3,14]. The overall pore size is limited to about 4 nm when using these kind of surfactants, though. The utilisation of swelling agents offered the possibility to expand the pore sizes to about 10 nm, but always accompanied with a broadening of the size distribution and an overall loss of structural order which was achieved in the first instance. Recently, block copolymers were used to synthesise large-pore mesoporous materials exhibiting cubic $Ia3d$ symmetry [43] as well as $Fm3m$ symmetry [44] with pore sizes of up to 12 nm.

The synthesis of SBA-15 silica offers the possibility to fine-tune the pore size just by varying the synthesis temperature [21]. Pore diameters up to than 10 nm can be achieved with a narrow size distribution. When going to higher mean diameters the distributions broaden though. With auxiliary chemicals it is even possible to prepare SBA-15 silica with pore sizes of over 40 nm [45].

Synthesising mesoporous materials with well defined pore diameters, *i.e.* narrow pore size distributions, is the first step to prepare reasonable hosts for the intra-pore synthesis of nanoparticles.

1.2. Semiconductor nanoparticles

1.2.1. Chemistry in confined spaces

The fabrication of ordered assemblies of semiconductor particles in the nanometre scale is a challenge in material science which has become more and more important over the last decades. With highly ordered arrays of well size-defined particles in a specific range of only a few nanometres available the understanding of the unusual dependence of electronic, optical and magnetic properties on size and shape of those nanoparticles has increased significantly. Most of the procedures to obtain 1D- or 2D-nanostructures, *i.e.* quantum dots and quantum wells, require non-equilibrium growth conditions, which can be realised by molecular beam epitaxy under ultra high vacuum. In order to fabricate 3D quantum wires the easiest way is to start with two-dimensional quantum wells and to use a subsequent etching procedure.

The direct chemical synthesis of a nanoparticle can only be realised by the utilisation of size-limiting matrices, which serve as a kind of "mini-reactor". Narrow particle size distributions can be obtained if a high quality of this nano-reactor is achieved. As hosts for a size-limited synthesis only a few possibilities are worth considering: firstly the utilisation of reverse micelles ("water-in-oil" droplets), which are already used widely in the synthesis of nanoparticles [46-55], and secondly the use of a porous substance which does not react with the precursors for the actual synthesis. In the large group of different porous substances, anodised porous alumina [56] and mesoporous materials [16], for instance, seem to be the most promising approach for nanoparticle syntheses since the size range, in which the pores – and therefore the nanoparticles – can be synthesised, covers a large scale of nanometres.

In the case of reverse micelles the size of the micelle is governed by the volume of the water molecules inside and by the surfactant molecules at the surface of the micelle, *i.e.* the space inside the micelle where the chemical reaction or coprecipitation takes place can be varied for example by changing the amount of water in the original solution [57]. One of the surfactants often used to form reverse micelles is sodium di(2-

ethylhexyl) sulfosuccinate, mostly denoted as Aerosol OT or Na(AOT). In a typical synthesis (see *Figure 1-4*), two micellar solutions, having the same water content (that is to say the same micelle size) and each containing one of the reactants, are mixed. When two of these micelles collide, they exchange their water contents in a micellar exchange process and the desired reaction occurs. After a few microseconds the previously formed "double-micelle" dissociates to form two independent reverse micelles, one containing the product while the other is only filled with water.

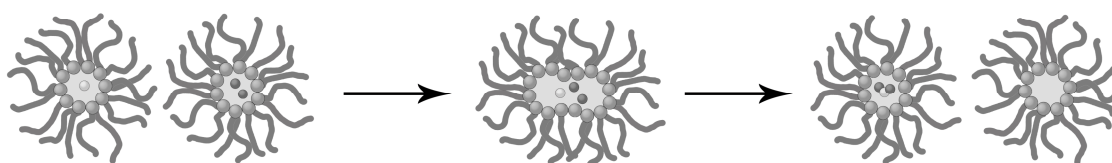


Figure 1-4: Micellar exchange process (redrawn from Ref. 57).

In the case of mesoporous materials as hosts for the synthesis of nanoparticles the narrow size distribution of the guest species is achieved by a narrow pore size distribution of the respective host material. In the last twelve years it has been a major goal in the synthesis of mesoporous substances to obtain materials which contain a high degree of long range order on the one hand and a narrow pore size distribution on the other. The quality of mesoporous materials has risen from poorly ordered so-called "disordered mesoporous foams" to high quality materials which have very sharp pore size distributions. The high degree of long range order can be pointed out via TEM investigations. A perfect arrangement of the pores over 300 nm and more is state of the art [7].

At this, introducing the precursor compounds into the pores of the respective size-limiting matrices is the mayor problem in the synthesis. The utilisation of reverse micelles has the advantage of a two phase system. Using a precursor which is only soluble in one of the phases (in this case water) prevents forming the desired materials outside the mini-reactor and results in a very defined synthesis exclusively inside the size limiting matrix.

In the case of mesopores as the size limiting matrix though, the formation of bulk materials outside the pore system can never be fully avoided. Only after the synthesis one can estimate the amount of bulk material formed during the synthesis. Wet impregnation techniques are the most commonly used procedures to introduce guest molecules into the pores of the host material. Drying the impregnated materials is the crucial step in the synthesis to prevent forming bulk material on the outer surface of the host structure. After the introduction of the precursor the other reactants have to be introduced via the gas phase, which is to prevent the extraction of the first precursor from the pores and the consecutive precipitation outside the pores if the second reactant is introduced in a liquid form. *Figure 1-5* gives a schematic representation of a mesopore directed synthesis of nanoparticles.

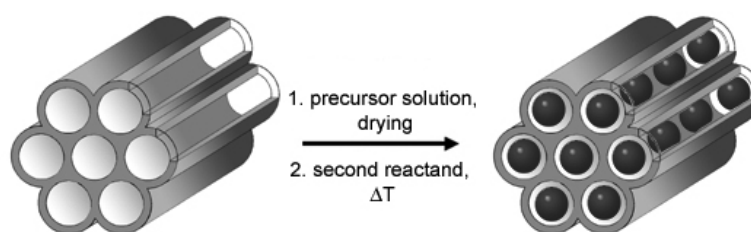


Figure 1-5: Schematic representation of nanoparticle synthesis inside a mesoporous host.

One of the most investigated semiconductor nanoparticle is cadmium sulphide, CdS [46,47,55]. The occurring quantum confinement, which is mostly reflected by a blue-shift of the band gap energy, has been discussed extensively [58-65]. Other nanoscale semiconductor compounds, such as III/V semiconductors (*e.g.* GaAs or InP) or other II/VI semiconductors (*e.g.* CdSe, CdTe, ZnS, ZnSe, ZnTe), have also been studied in great detail (see recent reviews [54,66-69]).

1.2.2. Nanostructured diluted magnetic semiconductors

The synthesis of the so called "diluted magnetic semiconductor" (DMS) nanostructures is of great interest as semiconducting and magnetic properties are combined in one and the same nanostructure. These materials are obtained, when a

cation A of a binary semiconductor AB is randomly substituted by a magnetic ion M, leading to a $A_{1-x}M_xB$ formula (see *Figure 1-6*).

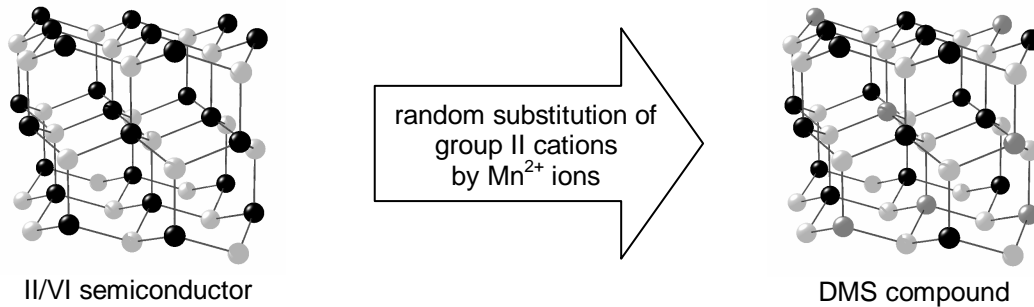


Figure 1-6: Schematic representation of the formation of a DMS compound (wurtzite structure).

Physical properties, like for example band gap energy or magnetism, are now not only a function of the particle size but also of the doping level x . Therefore ordered arrays of nanometre sized magnetic semiconductors are promising components for new devices in magneto- or spin electronics (*e.g.* magnetic hard disk media, non-volatile computer memory chips) [70].

An early review on doped II/VI semiconductors was given by Brandt and Moshalkov [71]. Later on, the investigations were extended towards different magnetic ions as dopands in the II/VI host material, like Fe [72,73], Co [74,75] and Cr [76,77]. Even the narrow gap IV/VI DMS became attractive, and various magnetic ions as dopands have been investigated (*e.g.* Mn [78], Eu [79] or Gd [80]). Rare-earth doped II/VI semiconductors have never reached the concentration of solid solutions, but remained rather in the doping regime. The main interest in those materials was exploiting the luminescence properties of the internal transitions rather than the magnetic properties [81]. Very recently a review on the dependence of the electronic and magnetic properties on the particle size of manganese doped nanostructured II/VI semiconductors was presented [82].

In the following a brief overview on manganese doped II/VI semiconductor nanostructures will be given. More detailed accounts on bulk magnetic semiconductors are given in the reviews on II/VI [71,83-85] and III/V [86-88] based materials.

II/VI semiconductors can form different crystal structures and for almost every compound more than one structure is known. The most prominent ones are zinkblende and wurtzite (each known for ZnS and CdS), both containing tetrahedrally coordinated metal cations, but the zinkblende structure consists of a cubic lattice, whereas the wurtzite structure is hexagonal. The binary compound MnS can form a rocksalt structure (with a light-pink colour), which converts at room temperature slowly into green the wurtzite phase. *Figure 1-7* depicts the different crystal structure types.

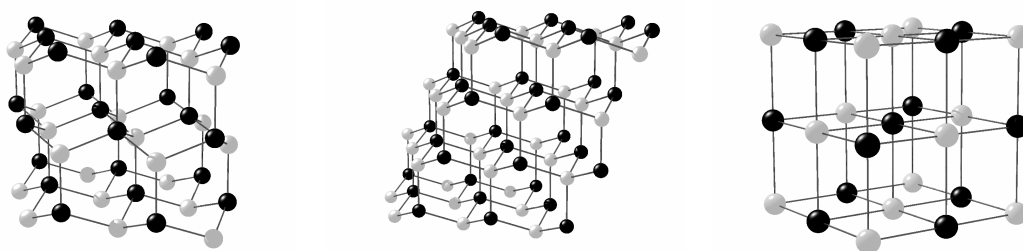


Figure 1-7: Crystal structures of wurtzite (left), zinkblende (middle) and rocksalt (right).

The solubility of Mn^{2+} in the II/VI semiconductor is a synthetical problem, which has to be addressed. Although the widest range of concentrations, compared to *e.g.* Fe, Co or Cr, can be achieved with Mn, there are miscibility gaps. In *Figure 1-8* the solubility limits of Mn^{2+} in II/VI semiconductors are shown. The crystal structure of the ternary compound with low Mn-concentration is always zinkblende or wurtzite. At high concentrations also rocksalt or NiAs structures are known.

The first preparation of manganese doped ZnS nanoparticles with particle sizes ranging between 3.5 nm and 7.5 nm was reported by Bhargava et al. in 1994 [89]. The quantum dots were synthesised by a precipitation approach in which diethylzinc and diethylmanganese in a toluene solution were treated with H_2S . In the case of liquid solution precipitation or self-organised growth methods the particle size distribution is not very well defined though, in particular, there is no sharp upper limit for the size. Very similar results were also found in other approaches [90-93]. Contrary to these approaches are syntheses of nanostructures within a nano-reactor such as reverse micelles or mesoporous materials. The existence of a sharp upper limit is desired in

most investigations of the effects of reduced dimensions on the magnetic properties as the largest particles usually determine the results.

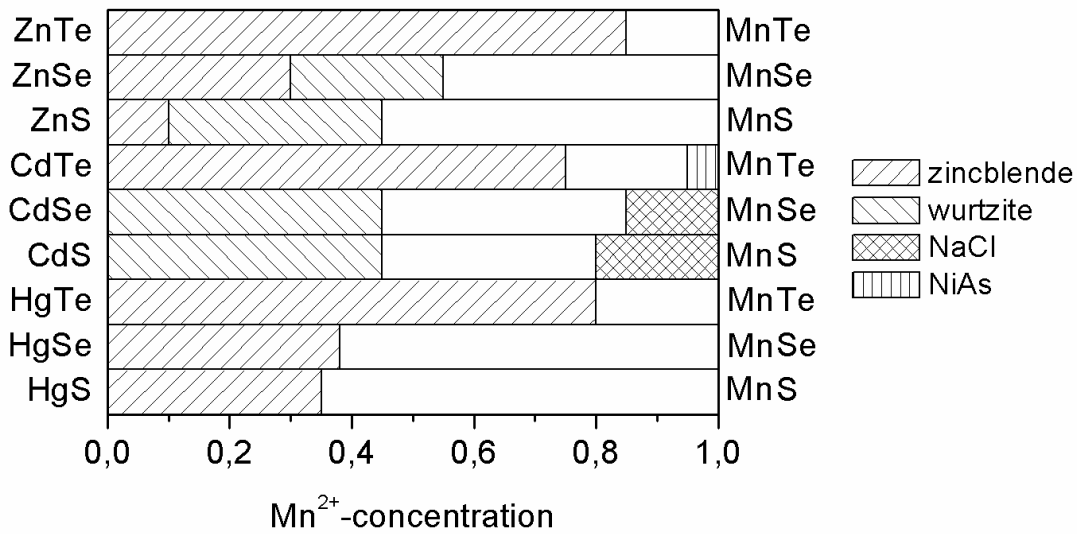


Figure 1-8: Solubility limits of Mn^{2+} in II/VI semiconductor compounds and corresponding crystal structures.

A synthesis of $Cd_{1-x}Mn_xS$ nanoparticles with a very sharp size distribution was reported by the group of Pileni by applying the reverse micelle technique [94,95]. The obtained particle sizes could be varied from an average size of about 1.8 nm to 3.2 nm and the reported manganese contents were $0 \leq x \leq 0.23$.

DMS nanoparticles were also synthesised inside mesoporous host structures. $Cd_{1-x}Mn_xS$ was firstly incorporated inside the 3 nm wide pores of MCM-41 silica in 2002 [96]. First, calcined MCM-41 silica was impregnated with an aqueous solution of cadmium and manganese acetate in the desired molar ratio. Afterwards the precipitate was filtered off, thoroughly dried and treated with H_2S at $T \leq 100$ °C. Powder X-ray diffraction and nitrogen physisorption proved the preservation of the host structure after the intra pore formation of the guest species and showed that the reaction had only taken place inside the pores and no bulk material was formed. The complete transformation of the acetates to the sulphides was proved by infrared spectroscopy. Similar results were obtained for other host/guest system based syntheses of nanoparticles, like $Cd_{1-x}Mn_xSe$ within MCM-41 silica [97] and $Cd_{1-x}Mn_xS$ within mesoporous thin films [98].

A more detailed discussion on the size dependence of electronic, magnetic and optical properties was given in 2004, when the DMS compound $\text{Zn}_{1-x}\text{Mn}_x\text{S}$ was synthesised inside mesoporous hosts with different pore sizes [99,100]. For an accurate study three different mesoporous materials, each with cylindrical pores, were used: MCM-41 silica with 3 nm pores and furthermore two SBA-15 silica structures with 6 and 9 nm pores, respectively. A very high degree of order of the host materials was achieved and proved by X-ray diffraction, sorption analysis and TEM investigations.

The intra-pore formation of the nanoparticles was carried out the same way as described for the $\text{Cd}_{1-x}\text{Mn}_x\text{Y}$ ($\text{Y} = \text{S}, \text{Se}$) nanoparticle preparation, only this time the impregnation/conversion cycle was repeated several times to achieve a better filling of the pores. Again, no bulk material was formed outside the respective pore system and the mesostructure was still found to be intact after the synthesis.

1.3. Aim of this work

The aim of this work was the synthesis and characterisation of high quality hexagonal mesoporous silica matrices and the synthesis and characterisation of manganese doped II/VI semiconductor nanostructures inside the pore structures.

In order to study in detail the effects of miniaturisation on the properties of the incorporated DMS materials, high-quality mesoporous host matrices with pore sizes in the range of 2-10 nm and narrow pore size distributions had to be synthesised, so the size dependence could be investigated thoroughly.

The wet impregnation technique of the mesoporous host structures followed by a thermal treatment with hydrogen sulphide was applied to prove the capability of this synthesis method for producing highly ordered arrays of DMS nanostructures with high size selectivity.

The size dependent changes in the physical properties of the nanostructured materials were investigated with respect to the electronic qualities, *i.e.* the band gap of

the semiconductor, the optical behaviour, *i.e.* energy transfer between the semiconductor band states and the $3d$ levels of the manganese, and the magnetic characteristics, *i.e.* phase transitions between different magnetic states.

2. Experimental

2.1. Synthesis of mesoporous host structures

2.1.1. Synthesis of MCM-41 silica (3 nm pores)

The syntheses of the pristine MCM-41 silica materials were carried out by mixing reactands with the following relative molar composition: 1.0 silicon dioxide (Cab-O-Sil) : 0.25 hexadecyltrimethylammonium bromide (CTABr) : 0.2 tetramethylammonium hydroxide (TMAOH, 25 % in water) : 35 H₂O.

0.25 mol hexadecyltrimethylammonium bromide (Merck) was dissolved in 35 mol water by stirring and heating to 65 °C. 0.2 mol tetramethylammonium hydroxide (Merck) and, under vigorous stirring, 1 mol SiO₂ (Riedel-de-Haen) were added. The mixture was kept stirring at 65 °C for 30 minutes, transferred into a Teflon-lined steel autoclave and stored at room temperature for 24 hours. The autoclave was then statically heated to 150 °C for 24 hours. The resultant white precipitate was filtered and washed several times with warm deionised water. Drying at room temperature under vacuum gave a white powder. The removal of the surfactant was carried out by storing the product for 24 h at 120 °C, followed by statically heating to 550 °C (heating rate 1 °/min) or by calcination in flowing air at 550 °C for 24 hours (heating rate 1 °/min).

2.1.2. Synthesis of SBA-15 silica (6 and 9 nm pores)

The syntheses of the pristine SBA-15 silica materials were carried out by mixing reactands with the following relative molar composition: 1.0 tetraethylorthosilicate (TEOS) : $17.95 \cdot 10^{-3}$ Pluronic P-123 : 3.27 HCl : 187.5 H₂O

0.8 g P-123 (Aldrich) were dissolved in 24 g of water and 2.86 g of concentrated hydrochloric acid at 35 °C on a water bath. After the addition of 1.6 g TEOS (Merck) the reaction mixture was stirred for 24 hours at 35 °C. The resulting gel was transferred into a Teflon-lined steel autoclave and heated up to 80 °C for 24 hours to obtain 6 nm

pores and up to 140 °C for 24 hours to obtain 9 nm pores. The resulting white powder was washed three times with deionised water and the surfactant was removed by calcination in flowing air at 550 °C for 24 hours (heating rate 1 °/min).

2.2. Synthesis of DMS compounds within mesoporous hosts

The intra-pore formation of the different semiconductor compounds was carried out applying the wet impregnation technique. Metal acetate solutions were used as precursors. The impregnation step was followed by a thermal conversion of the incorporated acetates with H₂S to the respective sulphides, or with H₂Se to the respective selenides.

The impregnation procedure was carried out by stirring 0.5 g of the porous host material (MCM-41 silica or SBA-15 silica) in a 0.5 molar solution of zinc acetate (Merck) and manganese acetate (Merck) with the desired ratio of Zn/Mn for 10 minutes. No further tuning on the pH value was carried out. *Table 2-1* summarises all relevant parameters. The dispersion was separated by centrifugation. The residue was dried in vacuum and stored in a H₂S or H₂Se atmosphere, respectively, at 100°C for 24 hours. The impregnation/conversion cycle was carried out twice for MCM-41 silica as the host structure, three times for SBA-15 silica with 6 nm wide pores and four times for SBA-15 silica with 9 nm pores. After the complete impregnation/conversion cycle the sample was washed free of remaining acetate by stirring in 20 ml of deionised water for 30 min.

The conversion of the acetates to the sulphides or selenides, respectively, was proved by FT-IR spectroscopy exhibiting no corresponding C=O bands.

Table 2-1: Relative ratios of the amounts of metal acetates and water used for the differently high manganese doped DMS compounds. All mixtures result in a total concentration of the respective metal cations of 0.5 mol/L.

doping level x	amount Cd acetate	amount Mn acetate	amount water
0	1.333 g	0 g	10 ml
1	2.639 g	0.025 g	20 ml
5	2.532 g	0.123 g	20 ml
10	2.399 g	0.245 g	20 ml
15	2.265 g	0.368 g	20 ml
20	2.132 g	0.490 g	20 ml
25	1.999 g	0.613 g	20 ml
30	1.866 g	0.735 g	20 ml
100	0 g	1.226 g	10 ml
doping level x	amount Zn acetate	amount Mn acetate	amount water
0	1.098 g	0 g	10 ml
1	2.173 g	0.025 g	20 ml
5	2.085 g	0.123 g	20 ml
10	1.975 g	0.245 g	20 ml
15	1.866 g	0.368 g	20 ml
20	1.756 g	0.490 g	20 ml
25	1.646 g	0.613 g	20 ml
30	1.536 g	0.735 g	20 ml
100	0 g	1.226 g	10 ml

2.3. Characterisation methods

2.3.1. Powder X-ray diffraction (P-XRD)

Powder X-ray diffraction (P-XRD) patterns were recorded with a Bruker/AXS D8 advance diffractometer using filtered Cu-K α radiation in θ/θ geometry in reflection mode. The diffractometer was equipped with variable slits on the tube and detector side and a secondary monochromator. The data were taken in a step scan mode with $\Delta 2\theta = 0.02^\circ$ and a counting time of 1 s per step as standard configuration.

2.3.2. Physisorption measurements

Physisorption is based on the weak bond of an inert gas particle on a surface with adsorption heats of about 5 - 10 kJ/mol. In the case of mesoporous materials the binding force is of a van-der-Waals-type, whereas in the case of microporous materials the adsorptions heats of up to 25 kJ/mol are extended in the chemisorption area. Different types of isotherms and hysteresis loops can appear. In *Figure 2-1* the characteristic types of isotherms are shown. Type I is typical for a solely microporous material with a high specific surface area; type II is characteristic for a non-porous or macroporous substance. Isotherms of the type III are undesirable and appear if the interaction between adsorbens and surface is too weak. Their occurrence can mostly be avoided by choosing a different kind of adsorbens. Mesoporous materials with a narrow pore size distribution cause the isotherm type IV. Type V is, like type III, unwanted and occurs also if the adsorbens-surface interaction is too weak. Type VI, finally, is a sequence of type II isotherms and is caused by consecutive monolayer adsorption on uniform non-porous substances.

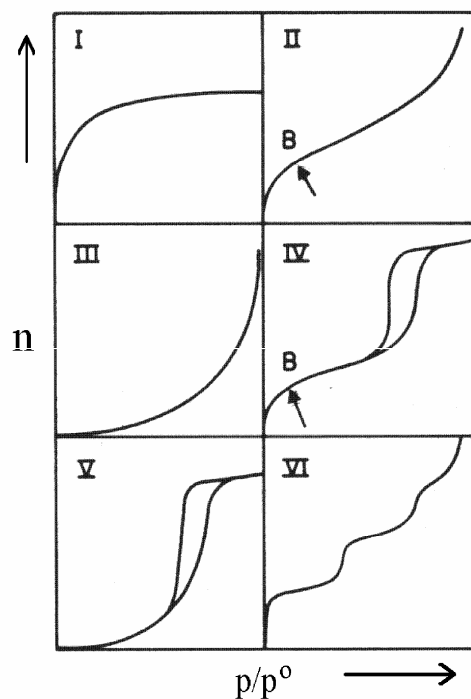


Figure 2-1: Diagram of the characteristic types of isotherms [1].

While measuring adsorption isotherms hysteresis loops can occur due to capillary condensation. *Figure 2-2* gives an overview of the different possible types.

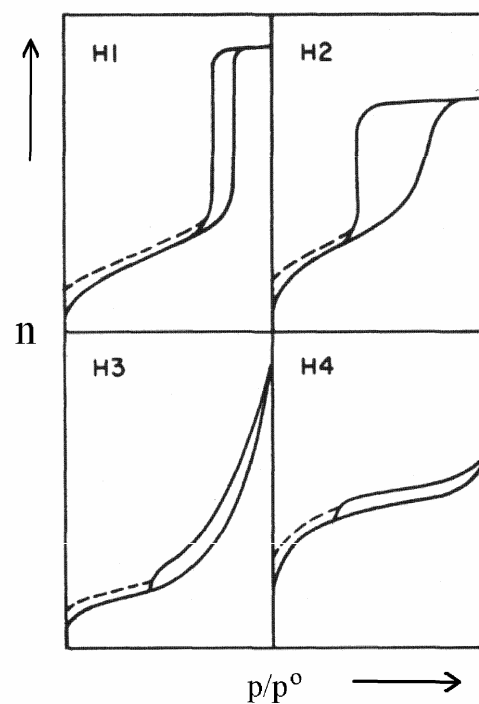


Figure 2-2: Overview of the different types of hysteresis loops [1].

The hysteresis loop H1 is attributed to a mesoporous substance with a narrow pore size distribution, H2 is characteristic for a mesoporous material with a broader distribution or with non-cylindrical pores. Larger slit pores cause the hysteresis loop of type H3, microporous slit pores cause type H4.

Specific surface areas and pore diameters were determined by nitrogen adsorption/desorption measurements at 77 K using a Quantachrome Autosorb 6 instrument. Nitrogen (purity 99.999 vol%), used as adsorbent, and helium (purity 99.999 vol%), used as backfill gas, were supplied by Messer Griesheim. Before each sorption measurement the sample was outgassed at 120 °C for at least 24 hours under vacuum.

The surface areas were calculated applying the theoretic equation of Brunauer, Emmet and Teller (BET) [101] for relative pressures between 0.03 and 0.2-0.3, depending on the number of data points that were appropriate for a linear fit.

For the calculation of the mean pore diameter the model by Barrett, Joyner and Halenda [102] was used for all samples, despite of the fact, that this well established theory is actually only valid for materials with pores > 4 nm and underestimates the diameter of smaller mesopores by approximately 1 nm [103,104]. However, it is an appropriate method for determining changes in the pore size distributions [14] and is the only model which is independent on the kind of adsorbent.

All calculations were achieved with the AUTOSORB 1 software for Windows, Version 1.5 (January 9, 2004).

2.3.3. *Transmission electron microscopy (TEM)*

For electron microscopic measurements the samples were crushed in ethanol and the ground material was dispersed on a holey copper grid. The transmission electron micrographs were recorded on a Philips CM 300 UT instrument operating at 300 kV.

2.3.4. X-ray absorption spectroscopy (XAS)

X-ray absorption spectroscopic measurements were carried out at the storage ring DORIS III (HASYLAB, DESY, Hamburg, Germany) at the beamline A1, which was equipped with a silicon (111) double-crystal monochromator. The Mn, Zn and Cd K-edge spectra were recorded at room temperature in fluorescence mode. Each spectrum was calibrated against the first inflection point of the corresponding K-edge of a reference metal foil, which was measured simultaneously. Freshly prepared sulphides (precipitated with H_2S from an aqueous solution of the respective metal acetate) were used as a reference for the guest compounds. All samples were measured as pressed polyethylene pellets in which the metal content was adjusted to give an absorption jump $\Delta\mu_d = 0.4 - 0.9$.

The reduction of the raw data takes place in different steps. First, an energy calibration of the measured spectra has to be carried out (*Figure 2-3 a*). Therefore, a reference compound with an exactly defined edge energy is measured beside the actual sample. After that, a background correction of the entire spectrum (carried out with a Victoreen-fit) and a normalisation of the edge jump is executed (*Figure 2-3 b*). To compare different measurements, the spectra have to be converted into a form which is independent on the original edge energy. This is implemented by a transformation to the k-space (*Figure 2-3 c*). By means of a spline function, the atomic absorption coefficient $\mu_0(k)$ is then adapted to the spectrum in k-space. After this so called μ_0 -fit, the EXAFS oscillations are obtained in a $\chi(k)$ -function (*Figure 2-3 d*). By a Fourier transformation of these EXAFS oscillations a radial distribution function is obtained, in which the shells of the neighbouring atoms are visible as discrete peaks (*Figure 2-3 e*). This radial distribution function can now be fitted with proposed crystal structure parameters of the respective material.

For data analyses the programs FEFF 7.01 [105] and WinXAS [106] were used.

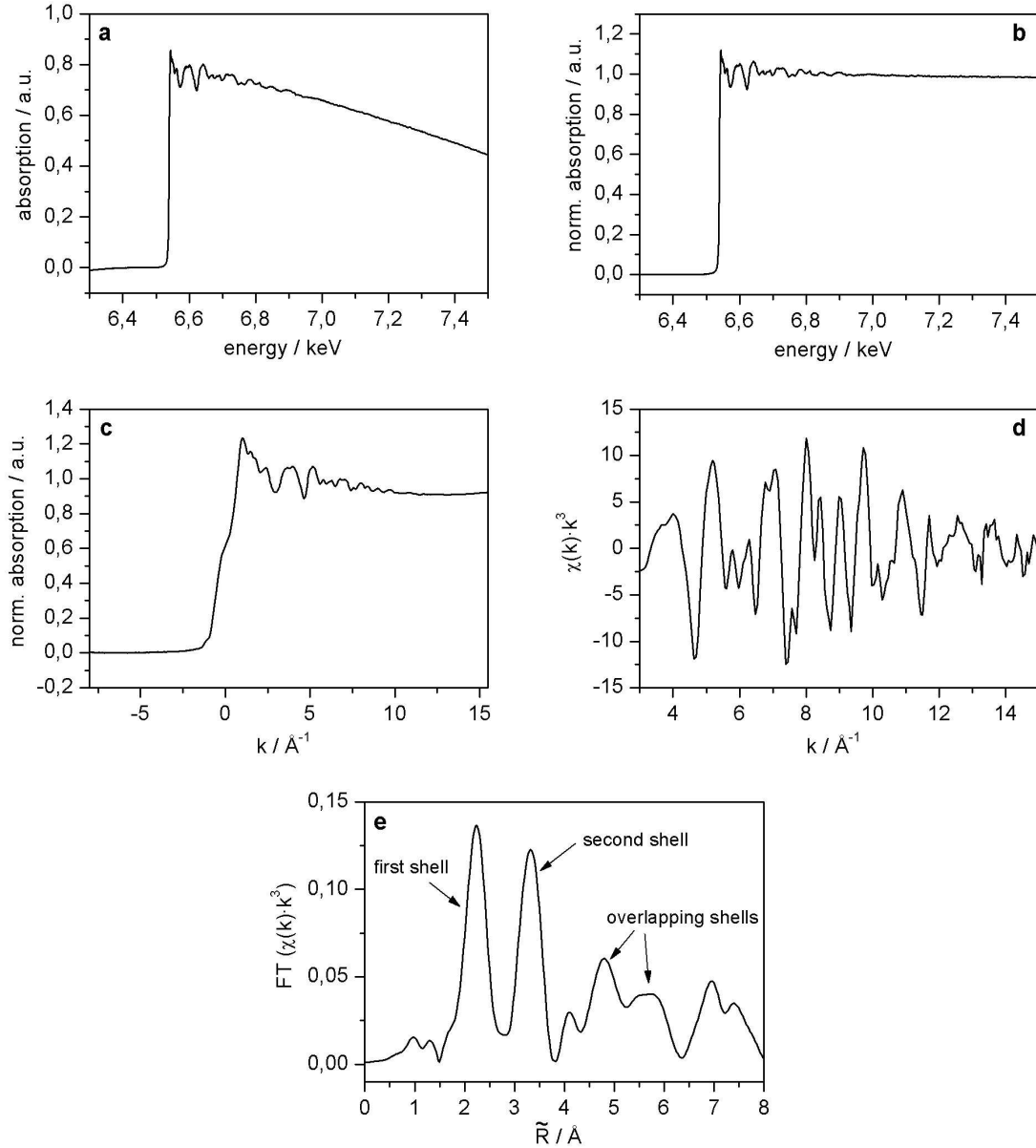


Figure 2-3: Processing of the raw EXAFS-data: (a) energy calibrated spectrum; (b) background corrected and normalised spectrum; (c) spectrum after conversion to the k -space; (d) $\chi(k)$ -function (after the μ_0 -fit); (e) radial distribution function.

2.3.5. Infrared and Raman spectroscopy

Infrared spectroscopy was carried out using a Perkin-Elmer FT-IR 1720 in the range from 400-4000 cm^{-1} in shuttle mode.

Phonon Raman spectra were obtained at room temperature. An argon-ion laser (Coherent Innova Sabre) operating single line at 364 nm (for the Zn samples) and at 488 nm (Cd samples) with an output power of about 100 mW was used for excitation. A

triple Raman spectrometer was used for light dispersion and detection. It consisted of a subtractive double stage (ISA 1680B) employed as band pass and a 1.25 m monochromator stage (Spex 1250m) equipped with a nitrogen-cooled CCD (ISA Spectrum One) for detection.

2.3.6. Photoluminescence spectroscopy (PL/PLE)

Photoluminescence (PL) is a method for the determination of energetic transitions within semiconductors and isolators. By irradiation of a sample with monochromatic light of an energy $E_i = h\nu_i$, which is higher than the band gap energy E_g , electrons are promoted from the valence to the conduction band. The formed electron-hole-pairs are mobile within the bands and recombine after a short period of time in a photon-emitting transition. The energy of the emitted photon E_h resembles the difference of the two energy band states within the sample (*Figure 2-4*).

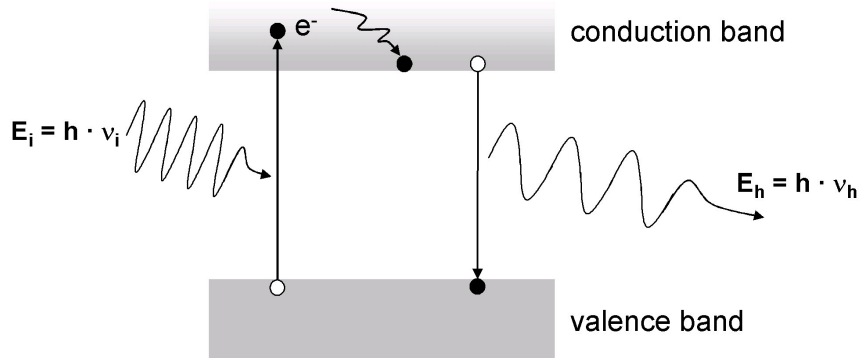


Figure 2-4: Schematic representation of the basic processes in photoluminescence.

Therefore PL measurements are a very effective method for investigations of electronic properties of materials. When performing photoluminescence excitation (PLE) spectroscopy the intensity of a specific emission band in dependence on the irradiation wave length is measured, while the irradiation intensity is kept constant.

In the case of a manganese-doped II/VI semiconductor the 3d band states of the Mn^{2+} are located in the band gap region of the semiconductor. Therefore very complex

optical processes can occur. *Figure 2-5* shows a schematic diagram of the possible transitions observable in widegap (II,Mn)VI semiconductors.

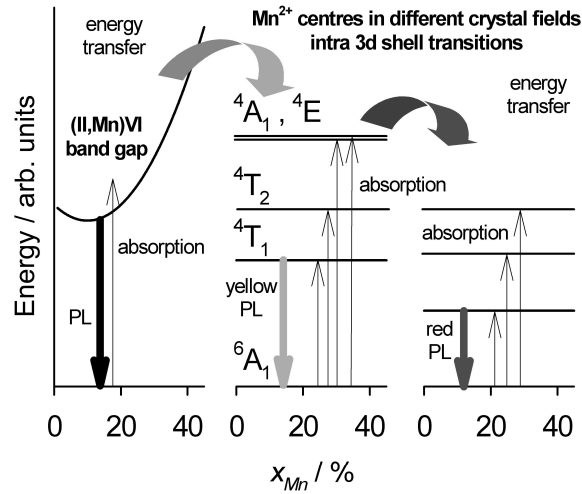


Figure 2-5: Schematic diagram of the optical processes observable in widegap (II,Mn)VI semiconductors. The abscissa values are the same for all three graphs.

The semiconductor band states with a direct band gap transition and the 3d shells of the Mn^{2+} ions with their internal transitions form subsystems of the (II,Mn)VI semiconductor which are coupled by energy transfer processes. In addition to semiconductor band gap related luminescence and absorption, luminescence and absorption bands due to the intra-3d-shell transitions of the Mn^{2+} ions are observed. The states within the 3d shell are strongly affected by the crystal field of the lattice site of the corresponding Mn^{2+} ion. The majority of the Mn^{2+} ions are incorporated on cation sites with a tetrahedral crystal field. The lowest state is the ${}^6\text{A}_1$ state originating from the ${}^6\text{S}$ state of the free ion, and the next higher states are ${}^4\text{T}_1$, ${}^4\text{T}_2$, ${}^4\text{A}_1$ and ${}^4\text{E}$ originating from the ${}^4\text{G}$ state of the free ion. Absorption processes can take place between the ${}^6\text{A}_1$ ground state and the excited states. A yellow luminescence between the ${}^4\text{T}_1$ first excited state and the ${}^6\text{A}_1$ ground state is observed for all widegap (II,Mn)VI compounds, independent of Mn concentration. In addition, there are a few Mn^{2+} ions on other sites. These "defect" sites show a different crystal-field splitting between the states of the 3d shell, and this leads to other absorption and luminescence bands. A prominent example is the red Mn^{2+} luminescence. Energy-transfer processes can take

place between the band states and the Mn^{2+} 3d shells, as well as between Mn^{2+} 3d shells corresponding to different sites.

In *Figure 2-6* the experimental setup is shown.

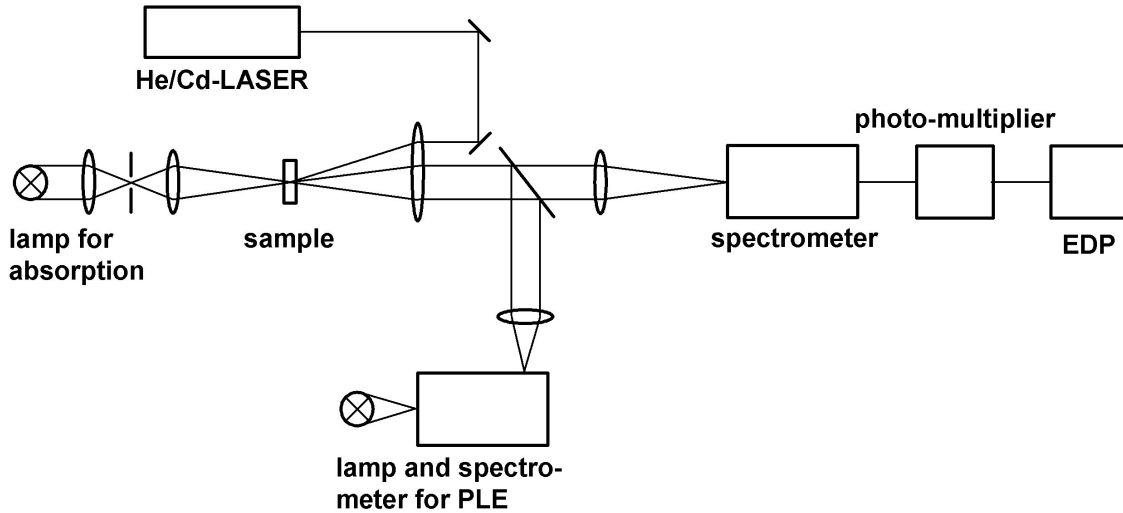


Figure 2-6: Schematic diagram of the PL/PLE experimental setup.

The photoluminescence-based optical measurements were carried out in the temperature range from 10 K to 300 K (Cd samples) and at 10 K (Zn samples) with the specimen mounted in a contact-gas He-cryostat (Cryovac K 1104 C). Tuneable monochromatic excitation light with a band width of 5 nm was provided either by a tungsten lamp (for PLE measurements) or by a deuterium lamp (for PL measurements) followed by a 0.32 m monochromator (ISA Triax 320). The sample luminescence was detected using a 0.5 m spectrometer (Zeiss) with a resolution better than 1 nm equipped with a GaAs photomultiplier (Hamamatsu).

For the Zn samples the PL measurements were carried out by exciting the specimen with the 325 nm light (3.81 eV) of a HeCd laser (Kimmon IK series) or with the lamp system set to 470 nm (2.63 eV). The PL signal was then detected in the range from 500 nm to 700 nm. For the PLE measurements the PL intensity was detected at 600 nm varying the wavelength of the excitation light from 270 to 580 nm.

For the Cd samples the PL measurements were carried out by exciting the specimen with 420 nm light (2.95 eV) and detecting the PL signal in the range from 450 to

900 nm. For the PLE measurements the PL intensity was detected either at 580 nm or at 700 nm varying the wavelength of the excitation light from 350 to 560 nm and 350 to 680 nm, respectively.

2.3.7. *Electron paramagnetic resonance spectroscopy (EPR)*

EPR spectroscopy is a technique which offers access to aspects of structure, of molecule and lattice dynamics and of reaction dynamics of material systems. It is based on measurements of the magnetic moment of an electron, the electron spin. Already in 1896 Zeeman discovered the splitting of lines in an optical spectrum by applying a magnetic field. This so-called "normal Zeeman effect" can be explained with the orbital angular momentum of the electrons, but later on anomalous Zeeman effects with more complicated splitting patterns were observed. In 1920 Stern and Gerlach showed with a basic experiment of the early quantum mechanics, that the magnetic moment of an electron in a magnetic field can only acquire discrete orientations. These results and the anomalous Zeeman effect were interpreted to that effect that a, to that point unknown, quantum number of the electron had to exist. This number is characteristic for the angular momentum of the electron, its spin. This spin should not be imagined as a self-rotation of the electron, in reality the electron spin is a quantum mechanical angular momentum which has no analogue in classical physics [107].

If an electron is exposed to a magnetic field, its magnetic moment causes an energy term, which is dependent on the magnetic quantum number m_S of the electron spin

$$E = m_S g_e \mu_B B_0 \quad \text{Equation 2-1}$$

with μ_B = Bohr magneton and B_0 = magnetic field strength.

The g-value of an electron can be determined experimentally and is a correction factor for relativistic effects. The g-value of a free electron is $g_e = 2.002319315$.

In EPR spectroscopy energies are often stated in frequency or magnetic field units rather than in wave numbers (*Equation 2-2*). *Figure 2-7* shows the typical scopes of these energies in comparison with the NMR frequencies.

$$1 \text{ G} = 0.1 \text{ mT} = 2.8 \text{ MHz} = 9.34 \cdot 10^{-5} \text{ cm}^{-1} = 1.12 \cdot 10^{-3} \text{ J mol}^{-1} \quad \text{Equation 2-2}$$

The measurement is carried out by applying a continuous or pulsed electromagnetic field to the sample. If the field energy complies with the energy difference between two states with $\Delta m_s = 1$, resonance absorption of the field energy occurs. The resonance frequency is dependant on the environment of the electron spin. A coupling between the spin and orbital angular momentum leads to deviation of the g-value from that of a free electron. Furthermore the magnetic moment of the observed electron spin interacts with other magnetic moments within the sample, which are associated with other electron or nuclear spins. Also an excited electron spin can give away its energy to the atomic lattice in a relaxation process. By careful observation of these processes information on structure and dynamic can be obtained.

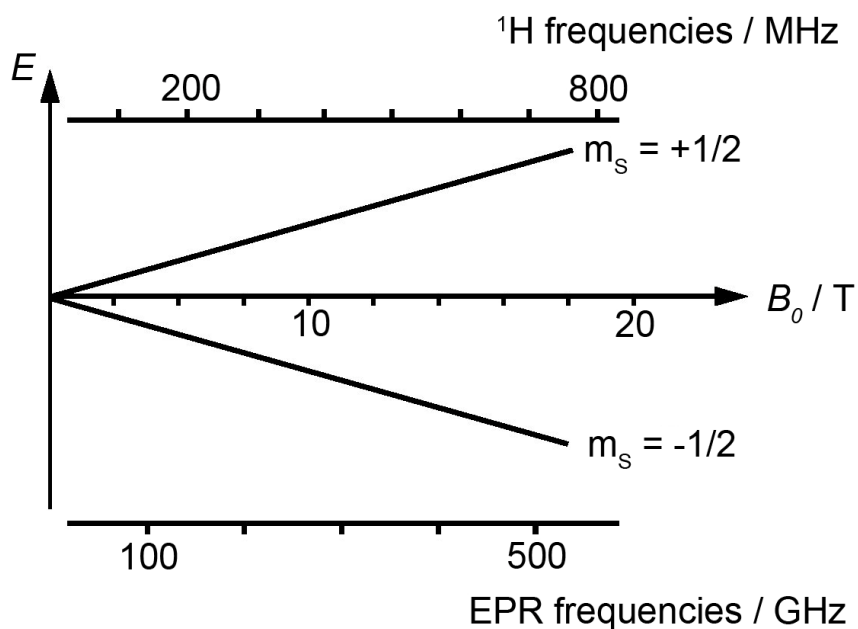


Figure 2-7: Splitting pattern of the energy levels of an electron spin in a magnetic field and comparison of the NMR and EPR frequencies.

The electron spin is related to another important property of materials, the magnetic susceptibility. When an external magnetic field H_0 is applied to a substance a magnetic induction B_0 arises within the structure. In vacuum it can be written as $\vec{B}_0 = \mu_0 \vec{H}_0$, with μ_0 = induction constant. When a substance is introduced into the field, the magnetic induction can be written as

$$\vec{B} = (1 + \chi_m) \mu_0 \vec{H} \quad \text{Equation 2-3}$$

χ_m is called the magnetic susceptibility and can be divided in diamagnetic ($\chi_m < 0$) and paramagnetic ($\chi_m > 0$) susceptibility. A diamagnetic contribution to the total susceptibility is always present, arising from the magnetic moments of the nucleus, the nuclear spins. If the electron spins do not mutually merge themselves due to spin coupling the substance is called paramagnetic. Only in this case an EPR signal is observable. The paramagnetic susceptibility is much larger than the diamagnetic and is dependent on the temperature (Curie-Weiss behaviour). If the electron spins strongly couple, so called ferro- or antiferromagnetic ordering can develop. In the former case the spins tend to orient themselves parallel in the absence of the magnetic field, in the latter case they align anti-parallel.

Mn^{2+} is the most important ion with d^5 electron configuration for EPR spectroscopy. Its total angular momentum is $J = 5/2$ which splits in a magnetic field B to $2J+1$ states (*Figure 2-8*). The transitions compliant with the selection rule $\Delta m_S = \pm 1$ can be detected via EPR.

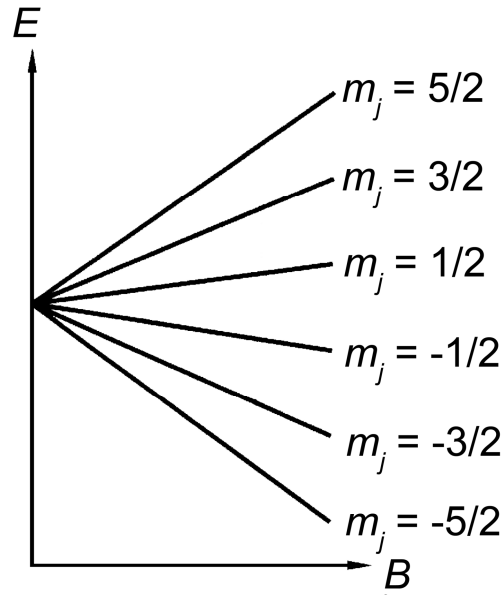


Figure 2-8: Zeeman splitting of the $2J+1$ states of Mn^{2+} in a magnetic field.

The interaction between the $I = 5/2$ spin of the manganese nucleus with the $S = 5/2$ spin of the electrons results in a hyperfine structure. Every m_S state splits into $2I+1$ hyperfine states (Figure 2-9) and an additional selection rule arises, given with $\Delta m_I = 0$. The allowed transitions within hyperfine coupled Mn^{2+} are therefore given by $\Delta m_I = 0$ and $\Delta m_S = \pm 1$, forbidden transitions are those with $\Delta m_I = \pm 1$ and $\Delta m_S = \pm 1$.

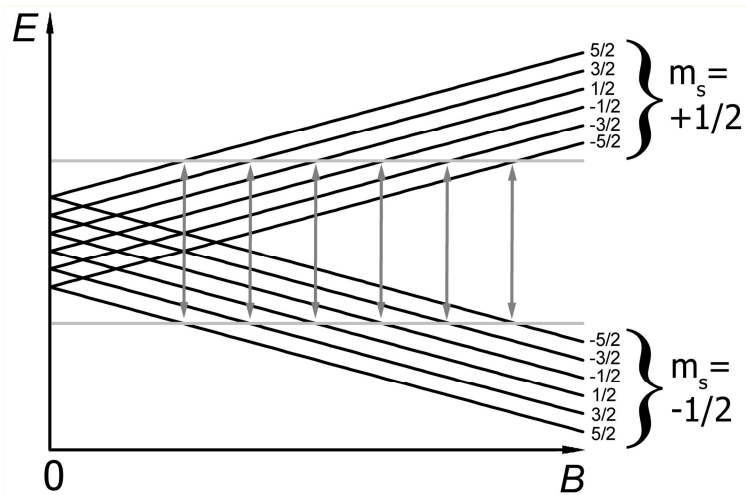


Figure 2-9: Hyperfine coupling between the Mn^{2+} nucleus and the electrons.

With no Mn-Mn interaction within the respective specimen, *i.e.* with only a little amount of manganese in the sample, the spectrum would consist of a sextet of sharp lines which can be satisfactorily described with a Lorentzian shape. With increasing

Mn^{2+} concentration the inter-manganese interaction becomes stronger, resulting in one broad Lorentzian shaped background. Depending on the strength of the Mn-Mn interactions the real spectrum can therefore consist of a superposition of the sextet from the hyperfine coupled Mn^{2+} over the background due to strong inter-manganese interactions (*Figure 2-10*).

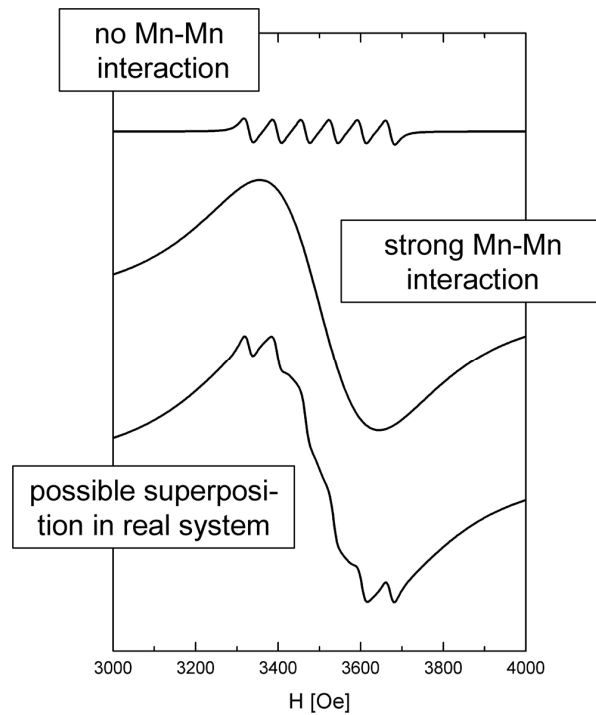


Figure 2-10: Dependence of the spectra on the strength of the Mn-Mn interactions.

A schematic representation of the experimental setup for EPR measurements is given in *Figure 2-11*.

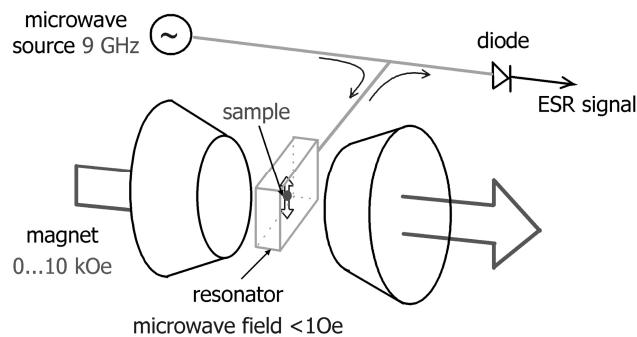


Figure 2-11: Schematic representation of the EPR measurement setup.

Electron paramagnetic resonance (EPR) measurements were performed using a Bruker Eleksys 500 CW spectrometer at X-band frequencies (9.48 GHz) and magnetic

fields up to 1 Tesla at temperatures between 4 K and 200 K in a continuous-flow He cryostat. As the signal-to noise ratio is improved by a lock-in technique with field modulation, the EPR spectra represent the field derivative of the microwave power absorbed by the sample from the transverse magnetic microwave field as a function of the external static magnetic field.

3. Results

3.1. Mesoporous host structures

3.1.1. Powder X-ray diffraction

Powder X-ray diffraction is one of the main characterisation methods for mesoporous materials. *Figure 3-1* shows typical XRD patterns of high-quality hexagonally ordered mesoporous silica. The samples were synthesised using CTABr (MCM-41 silica) as SDA or Pluronic P-123 (SBA-15 silica), respectively and calcined in air at 550 °C after the synthesis.

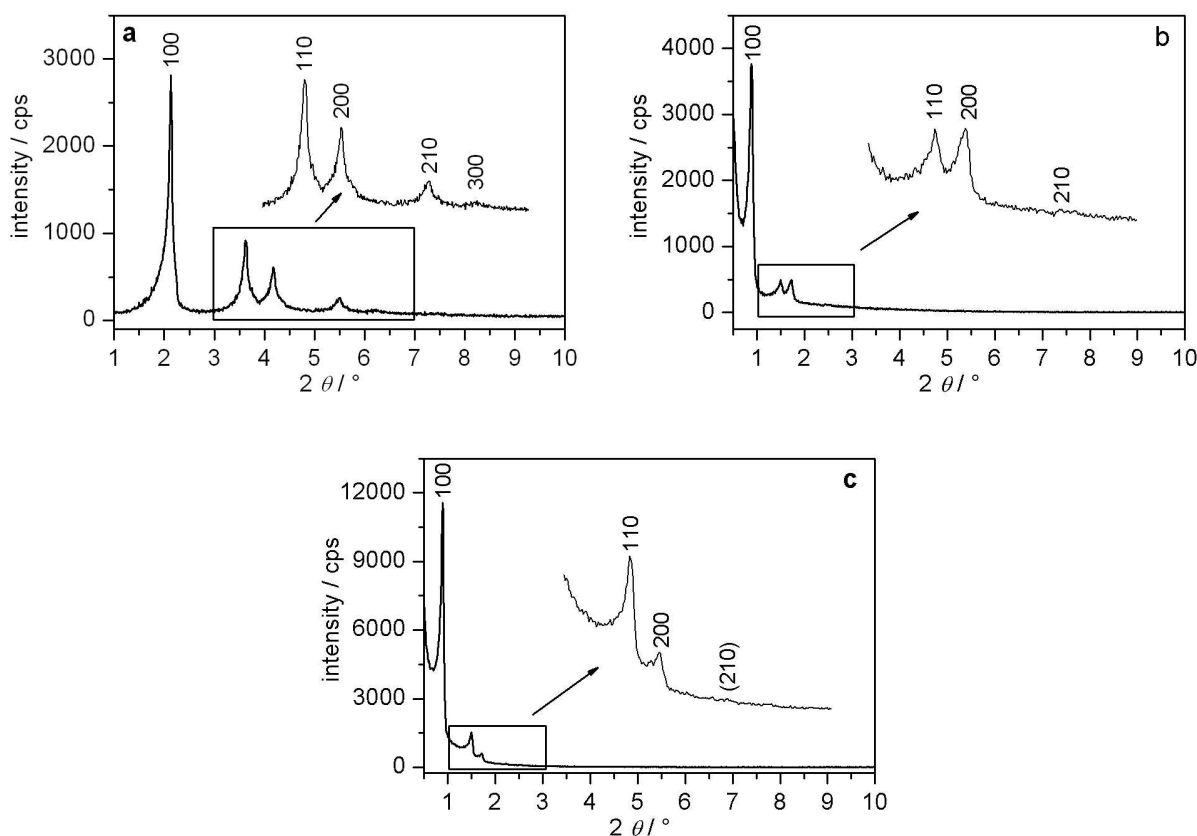


Figure 3-1: P-XRD patterns of (a) MCM-41 silica (3 nm), (b) SBA-15 silica (6 nm) and (c) SBA-15 silica (9 nm).

The main diffraction peak at approximately $2\theta = 2^\circ$ (MCM-41 silica) or $2\theta = 0.8^\circ$ (SBA-15 silica) arises from the (100) plane of the material and shows the high degree of

long-range order. In *Table 3-1* all detected peaks in the P-XRD patterns with the respective d values are listed.

Table 3-1: Miller indices hkl , $2 \theta_{hkl}$, d_{hkl} values and calculated unit cell parameter a for the different mesoporous host structures.

sample	hkl	$2 \theta_{hkl} / ^\circ$	d_{hkl} / nm	a / nm
MCM-41 (3 nm)	100	2.11	4.17	4.82
	110	3.62	2.44	
	200	4.17	2.12	
	210	5.48	1.61	
	300	6.29	1.40	
SBA-15 (6 nm)	100	0.87	10.09	11.65
	110	1.49	5.91	
	200	1.71	5.16	
	210	2.44	3.65	
SBA-15 (9 nm)	100	0.88	9.98	11.52
	110	1.48	5.96	
	200	1.70	5.18	
	210	(2.25)	(3.93)	

The similarity of the d_{100} values for the two different SBA-15 materials can be explained as follows: The difference in the pore size is not reflected in the d value, because in almost the same amount the pore size increases, the pore wall thickness t_{pw} decreases, resulting in a very similar unit cell parameter a , and hence in a very similar d value. This is effect will also be discussed later on, when the results of the nitrogen physisorption measurements are presented (see *Table 3-2*).

The calcination procedure does not only yield a porous material, it is also responsible for a shrinkage of the unit cell of the respective material. This is apparent

from *Figure 3-2*, where a comparison of the P-XRD patterns of MCM-41 silica before and after calcination is given. The calcination process at high temperatures leads to a further condensation of the silanol groups within the silica wall of the structure. This effect can be seen in the decrease of the d value of the (100) plane and hence in the decrease of the unit cell parameter a^a .

In addition, the intensity of the diffraction peak is increased after the surfactant removal. This is due to a decrease of the destructive interference between the scattering power of the pore walls and the pore itself, which is filled with the surfactant. This effect will be discussed more thoroughly in *Chapter 3.2.1*.

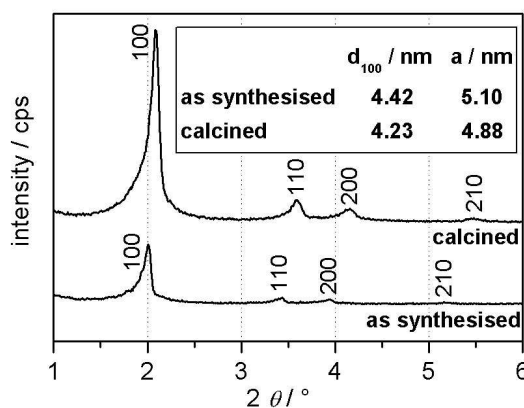


Figure 3-2: Comparison of the P-XRD patterns of MCM-41 silica as synthesised and after calcination.

3.1.2. Nitrogen physisorption

Apart from X-ray diffraction studies physisorption measurements are the most powerful tool for the investigation of the pore system of mesoporous materials. Upon the variety of gases which can be applied as adsorptive in this method the most commonly used is nitrogen. The evaluation of the specific surface areas is mostly carried out applying the BET theory [101] and the pore size distributions are usually calculated with the BJH algorithm [102]. The BJH calculation is based on the Kelvin equation and underestimates the mean pore diameter of small mesopores by the

^a $a = \frac{2}{3} \sqrt{3} \cdot d_{100}$

magnitude of at least 1 nm, as mentioned in *Chapter 2.3.2*. Nevertheless, it allows the determination of relative changes of the pore size distributions. The application of other methods which correct the underestimation of the BJH method, like for instance non-local density functional theory (NLDFT) [108,109], would be better for the pristine mesoporous silica phases, but inappropriate for the host/guest compounds. The NLDFT method is based on calculated isotherms with a given pore geometry (*e.g.* cylindrical) and pore wall surface (*e.g.* SiO₂), *i.e.* based on defined and known pore wall/adsorptive interactions. In the case of host/guest compounds these conditions are not fulfilled. Nevertheless, comprehensive studies have shown that the BJH method gives appropriate results to determine the differences between different mesoporous materials [14,110], and it can be applied by all commercially available physisorption computer programs. Therefore this method was chosen for the determination and comparison of the pore sizes of all mesoporous compounds in this work.

Figure 3-3 shows the nitrogen physisorption isotherms and the corresponding pore size distributions of MCM-41 silica (3 nm) and two SBA-15 silica materials (6 and 9 nm). All materials show a type IV isotherm after the IUPAC nomenclature [111], which is characteristic for mesoporous materials. The strong increase in the adsorbed volume is due to pore condensation during the adsorption process. For the two SBA-15 materials a hysteresis loop of the type H1 is observed between adsorption and desorption branch, whereas no hysteresis loop is observable for MCM-41 silica, because the pore diameter of this material is smaller than in SBA-15 silica materials. Pore condensation in MCM-41 silica materials takes place at values $p/p_0 < 0.4$. The lower closure point for nitrogen physisorption hysteresis at 77 K is $p/p_0 = 0.42$, which was originally considered the limit of the thermodynamic stability of the liquid nitrogen meniscus, hence no hysteresis is visible for MCM-41 silica. Theoretical studies [112] and computer simulations [113] indicate that the pore wall roughness and details of the fluid-wall interaction may also be significant for the disappearance of nitrogen physisorption hysteresis in MCM-41 silica materials (see also *Reference 14*).

An H1 hysteresis is typical for a material with cylindrical mesopores with a narrow pore size distribution. In the right part of *Figure 3-3* the distributions are shown. All three materials exhibit sharp distributions, with larger pores the distributions broaden though.

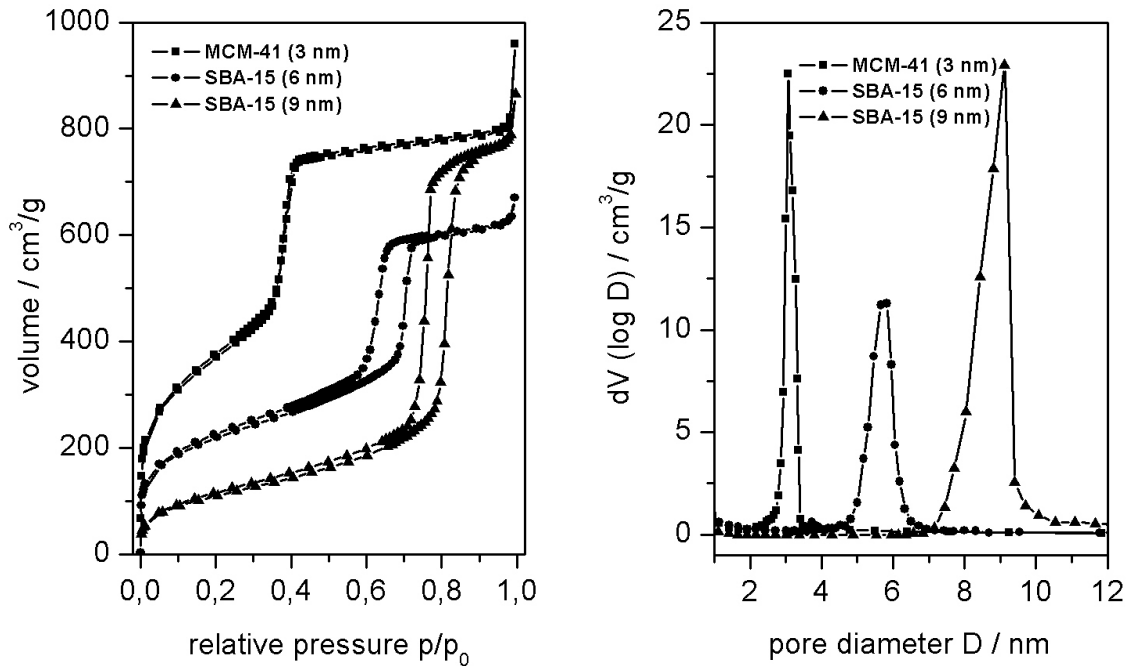


Figure 3-3: Nitrogen physisorption isotherms (77 K) of MCM-41 silica (3 nm), SBA-15 silica (6 nm) and SBA-15 silica (9 nm) (left); and corresponding pore diameter distributions calculated by BJH from the desorption branch (right).

The specific surface areas A_s and the mean pore diameter D_p calculated from the maximum of the pore size distribution are compared to the d values, the unit cell parameter a and the pore wall thickness t_{pw} in *Table 3-2*. The pore wall thickness t_{pw} is calculated after $t_{pw} = a - D_p$. The determination of the unit cell parameter a is not absolutely accurate with measurements on a standard powder X-ray diffractometer. Also the determination of the pore diameter D_p may have a significant error, as pointed out earlier. However, as long as the obtained values are not regarded as absolute values, they can be used for comparative investigations.

The pore wall thickness of MCM-41 silica is considerably lower than for the SBA-15 materials. This is a result of the different synthesis conditions, for the

hydrolysis and condensation behaviour of ionic silica species in aqueous solution is strongly determined by the pH value. MCM-41 silica is synthesised in a basic approach, whereas SBA-15 silica comes from an acidic synthesis mixture.

Table 3-2: d_{100} values, calculated unit cell parameter a and pore characterisation by nitrogen physisorption data for MCM-41 silica (3 nm), SBA-15 silica (6 nm) and SBA-15 silica (9 nm).

sample	d_{100} / nm	a / nm	A_s / m ² /g	D_p / nm	t_{pw} / nm
MCM-41 (3 nm)	4.17	4.82	1108	3.08	1.74
SBA-15 (6 nm)	10.09	11.65	753	5.80	5.85
SBA-15 (9 nm)	9.98	11.52	401	9.07	2.45

The synthesis of SBA-15 silica with different pore sizes only varies in the synthesis temperature and not in the initial mixture, hence the same amount of silica is available for the different structures. The increase in the pore size is accompanied with a decrease of the pore wall thickness t_{pw} , so the unit cell parameter a remains almost unaffected by this. In both SBA-15 structures the unit cell is about 10 nm large.

The fact that higher temperatures or longer reaction times result in larger pore sizes (and thus in thinner silica walls) is caused by the temperature dependence of the hydrophilicity of the PEO block in the Pluronic polymer [21,114]. The PEO parts are expected to interact more strongly with the silica and thus be more closely associated with the inorganic wall than the more hydrophobic PPO blocks. The PEO chain may exist in a large number of conformations, which have different energies. The conformation of an EO group which is gauche around the C–C bond and anti around the C–O bond has the lowest energy of all conformers (*Figure 3-4*, top). This low-energy conformation, which is dominant at low temperatures, has a large dipole moment. With

increasing temperature, other conformations with smaller or no dipole moments like the anti-anti-anti conformation (*Figure 3-4*, bottom) will become more important [115].

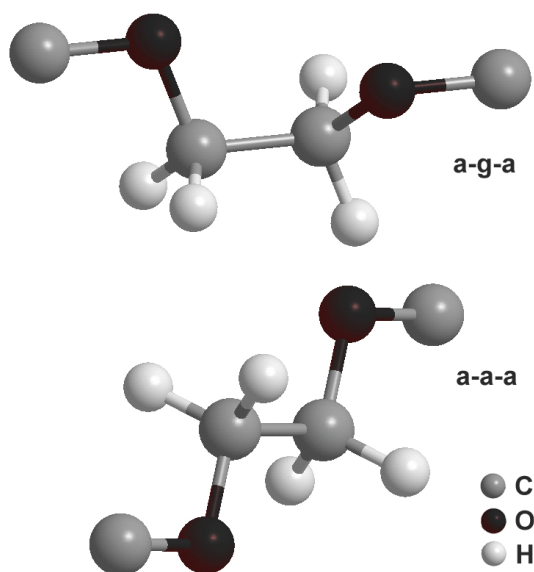


Figure 3-4: Different conformations of an EO group have different stabilities and polarities. The upper anti-gauche-anti conformation has a lower energy and is more polar than the lower anti-anti-anti conformation [115].

Thus, at higher temperatures, the PEO blocks become more hydrophobic, resulting in increased hydrophobic domain volumes, smaller length of PEO segments associated with the silica wall and hence in increased pore sizes (*Figure 3-5*).

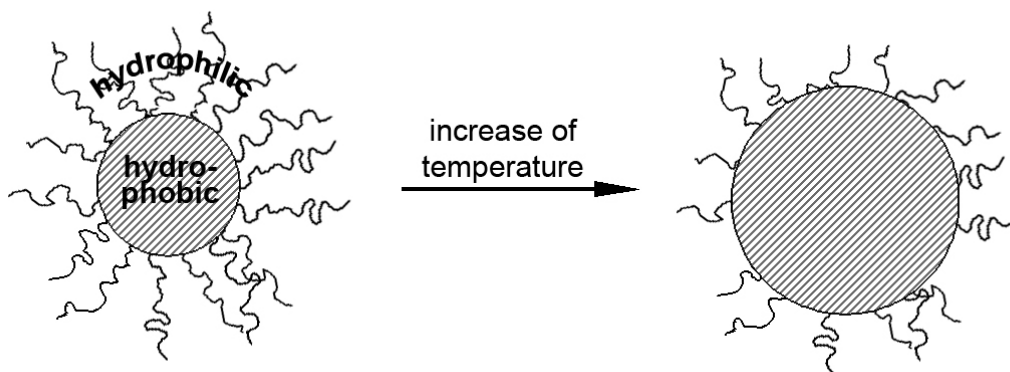


Figure 3-5: Increase of the hydrophobic domain volume of a block copolymer micelle in solution due to increase of the temperature.

To investigate the influence of temperature and duration of the hydrothermal treatment on the pore size of SBA-15 silica more thoroughly, further syntheses were carried out. While the initial synthesis mixture was kept the same, the temperature of the hydrothermal treatment was raised from 60 °C up to 140 °C (at temperatures higher than 140 °C the Teflon from the autoclave is decomposing) and the synthesis at 140 °C was carried out for 24, 48 and 72 hours. In *Figure 3-6* the nitrogen physisorption isotherms together with the BJH pore size distribution of the different synthesis approaches are shown. It can clearly be seen, that an increase in the temperature results in an increase of the pore diameter. Also an increase of the duration of the synthesis at a constant temperature results in an increase of the pore diameter, but not in the same amount as the temperature. With increasing pore diameter the distributions broaden though.

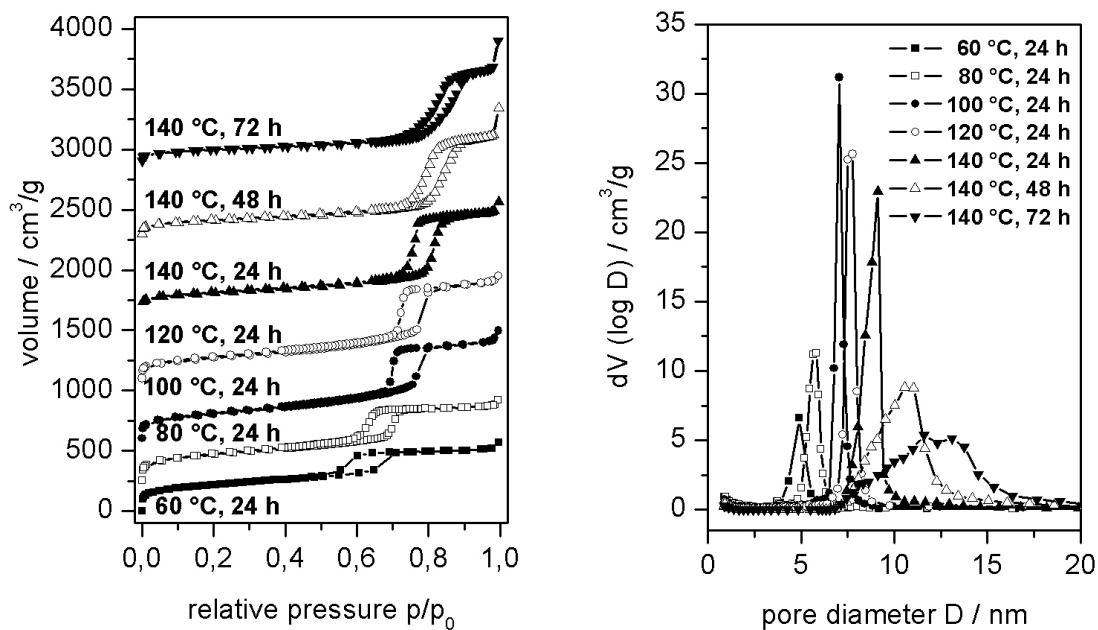


Figure 3-6: Nitrogen physisorption isotherms (left) and BJH pore size distributions (right) of different SBA-15 synthesis approaches. An offset of 250, 600, 1100, 1700, 2300 and 2900 cm³/g was added to the volumes of the approaches at $T > 60$ °C.

Figure 3-7 depicts the change of the pore diameter depending on the synthesis temperature. In the range of 60-140 °C a linear fit gives a slope of 0.05 nm and a y-intercept of 1.68 nm and yields a good agreement with the experimental data. A

prediction of the pore size of SBA-15 silica over a range of about 5 nm within a narrow error margin is now possible even before the synthesis is carried out. This opens the door for a much more reasonable synthesis of well-defined host materials in the field of host/guest chemistry.

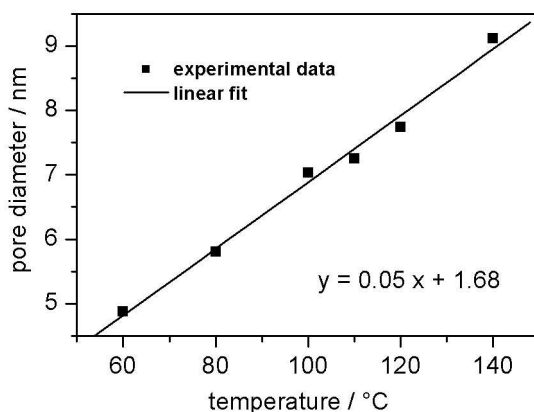


Figure 3-7: Change of pore diameter with increasing temperature of the hydrothermal treatment during the synthesis of SBA-15 silica with linear fit.

3.1.3. Transmission electron microscopy

Transmission electron microscopy (TEM) is another powerful tool to investigate mesoporous structures. The results from powder X-ray diffraction and physisorption are substantiated by TEM analysis. All pictures (*Figure 3-8*) were taken after the calcination process and show a perfect arrangement of the pores over several hundreds of nanometres. All materials are stable even after the harsh condition applied during the calcination process. Furthermore, EDX analyses show that the amount of manganese within the nanostructured samples is in good agreement with the amount of manganese which was started with in the initial synthesis mixture (see also *Table 2-1*).

It is also visible that the calculated values for the pore diameter D_p and the pore wall thickness t_{pw} (*Chapter 3.1.2*) are in good agreement with the micrographs.

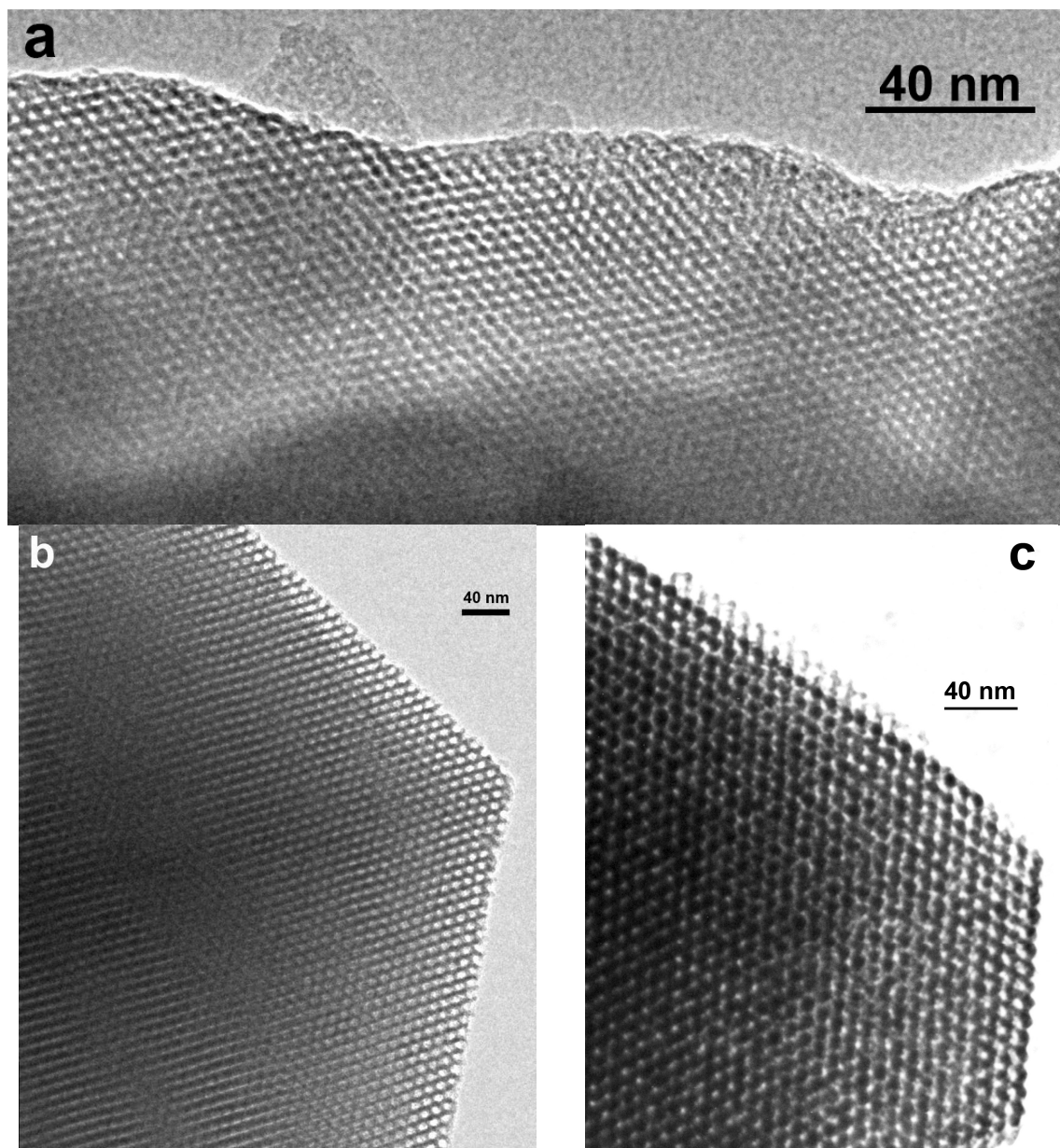


Figure 3-8: Transmission electron micrographs of (a) MCM-41 silica (3 nm), (b) SBA-15 silica (6 nm) and (c) SBA-15 silica (9 nm).

3.1.4. Conclusions

In Chapter 3.1 the successful syntheses of different mesoporous materials with varying pore diameters were shown.

Powder X-ray diffraction proved the high long-range order of the synthesised MCM-41 and SBA-15 silicas. Nitrogen physisorption measurements indicated that the structures have high specific surface areas and all materials exhibit cylindrical pores

with a narrow pore size distribution. The pore diameter of SBA-15 silica strongly depends on the temperature and duration of the hydrothermal treatment of the initial synthesis mixture.

With this kind of highly ordered and stable material available the conduction of further syntheses with MCM-41 and SBA-15 silica as host structures is a promising approach for the formation of highly size-defined nanoparticles inside the respective pore systems.

3.2. Host/guest compounds

3.2.1. Powder X-ray diffraction

In *Figure 3-9* the P-XRD patterns, taken after each impregnation/conversion cycle of the intra-pore formation of various DMS compounds in different mesoporous hosts, are shown. In all samples the main diffraction peak of the mesoporous host matrix is still visible after the respective impregnation/conversion cycles, which is an indication for the preservation of the mesoporous hosts. With every impregnation/conversion cycle the intensity of the X-ray reflections decreases, accompanied by a slight shift to smaller d spacings (exemplarily shown for *Figure 3-9 c*). The latter effect can be attributed to the thermal treatment which is associated with the impregnation/conversion procedure. Thus, like after the calcination process, the connectivity within the silica is increased, resulting in a small contraction of the overall host structure. The effect, that mesoporous structures contract upon calcination or treatment in acidic solutions, is consistent with literature reports [116].

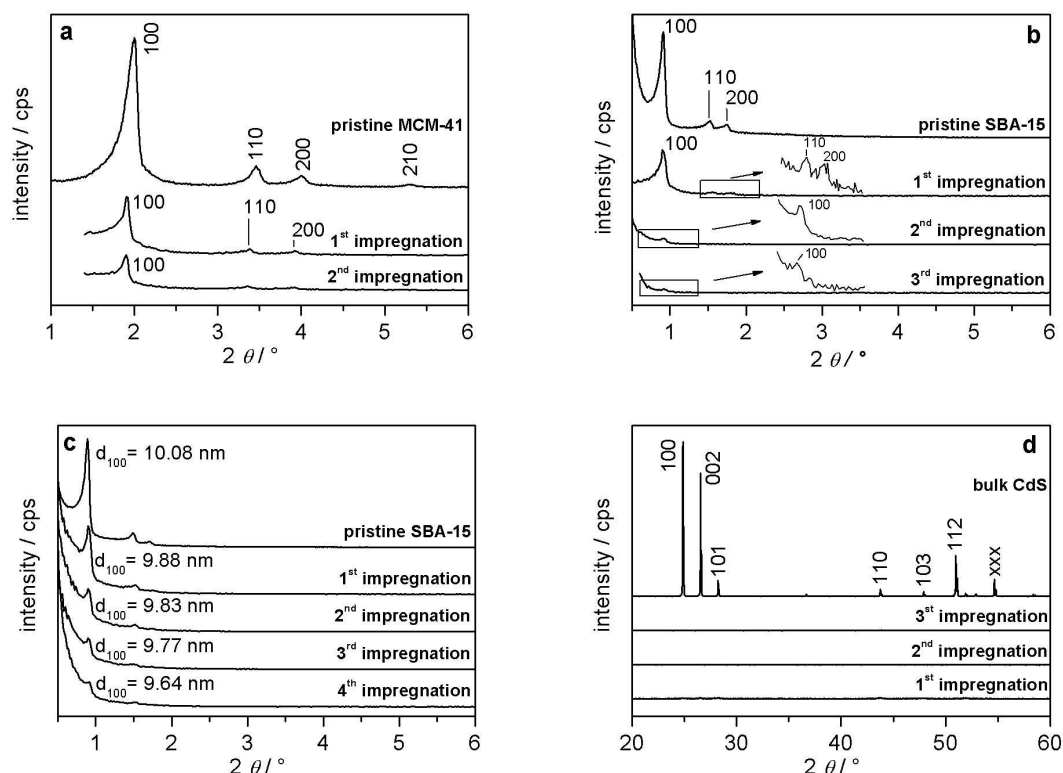


Figure 3-9: P-XRD patterns taken at different steps of the synthesis of (a) $\text{Zn}_{0.9}\text{Mn}_{0.1}\text{S}$ in MCM-41 silica (3 nm), (b) $\text{Cd}_{0.95}\text{Mn}_{0.05}\text{S}$ in SBA-15 silica (6 nm), (c) $\text{Zn}_{0.8}\text{Mn}_{0.2}\text{S}$ in SBA-15 silica (9 nm) and (d) high angle region of $\text{Cd}_{0.95}\text{Mn}_{0.05}\text{S}$ in SBA-15 silica (6 nm) together with bulk CdS.

The loss in intensity of the X-ray peaks corresponds to increasing destructive interference by subsequent filling of the pores with the respective sulphides. The introduction of scattering material into the pores leads to an increased phase cancellation between the scattering from the silica walls and the pore regions. Therefore the intensities for the Bragg reflections are reduced. First theoretical models have shown that this phase relationship is very sensitive and that the degree of cancellation is mainly determined by the scattering contrast between the framework and the pores [117]. The reverse effect is responsible for the increase of the reflex intensities in the pristine mesoporous material after the calcination process (see *Chapter 3.1.1*).

Apart from the typical reflections of the mesoporous host materials, no additional peaks are observed in the 2θ region between 20 and 60° for all samples (see *Figure 3-9 d*). This is an indication that no crystalline sulphides have been formed outside the respective pore structures. In the case of the 3 nm particles inside the pores of MCM-41

silica the crystals are simply too small to give X-ray reflections (assuming they are of spherical shape). For 9 nm particles inside the respective pore system of SBA-15 silica very broad Bragg reflections can be observed in some cases, but they still have a too low signal-to-noise ratio for the determination of the particles size according to Scherrer's formula.

3.2.2. Nitrogen physisorption

In *Figure 3-10* the nitrogen physisorption isotherms at 77 K for three different host/guest compounds are shown. All isotherms are of type IV, typical for mesoporous materials [1]. This is a proof for the preservation of the mesoporous hosts after the respective impregnation/conversion cycles. A well defined step occurs at $p/p_0 = 0.3-0.4$ for the 3 nm samples, at $p/p_0 = 0.5-0.7$ for the 6 nm samples and at $p/p_0 = 0.7-0.9$ for the 9 nm samples, associated with the filling of the mesopores due to capillary condensation. Especially in the case of the 6 nm samples a change of the hysteresis type from H1 to H2 can be observed. This is caused by an inhomogeneous filling of the mesopores with the respective guest compound and the thereby caused less uniform remaining pore size (see also *Chapter 2.3.2*). Depending on the number of impregnation/conversion cycles the amount of adsorbed nitrogen decreases accompanied with a shift of the inflection point to smaller values of p/p_0 . Both effects can be attributed to the introduction of the sulphides into the mesopores. The reduced amount of physisorbed nitrogen is caused by a smaller surface area, while the occurrence of the step at lower relative pressure is indicative of smaller pore sizes.

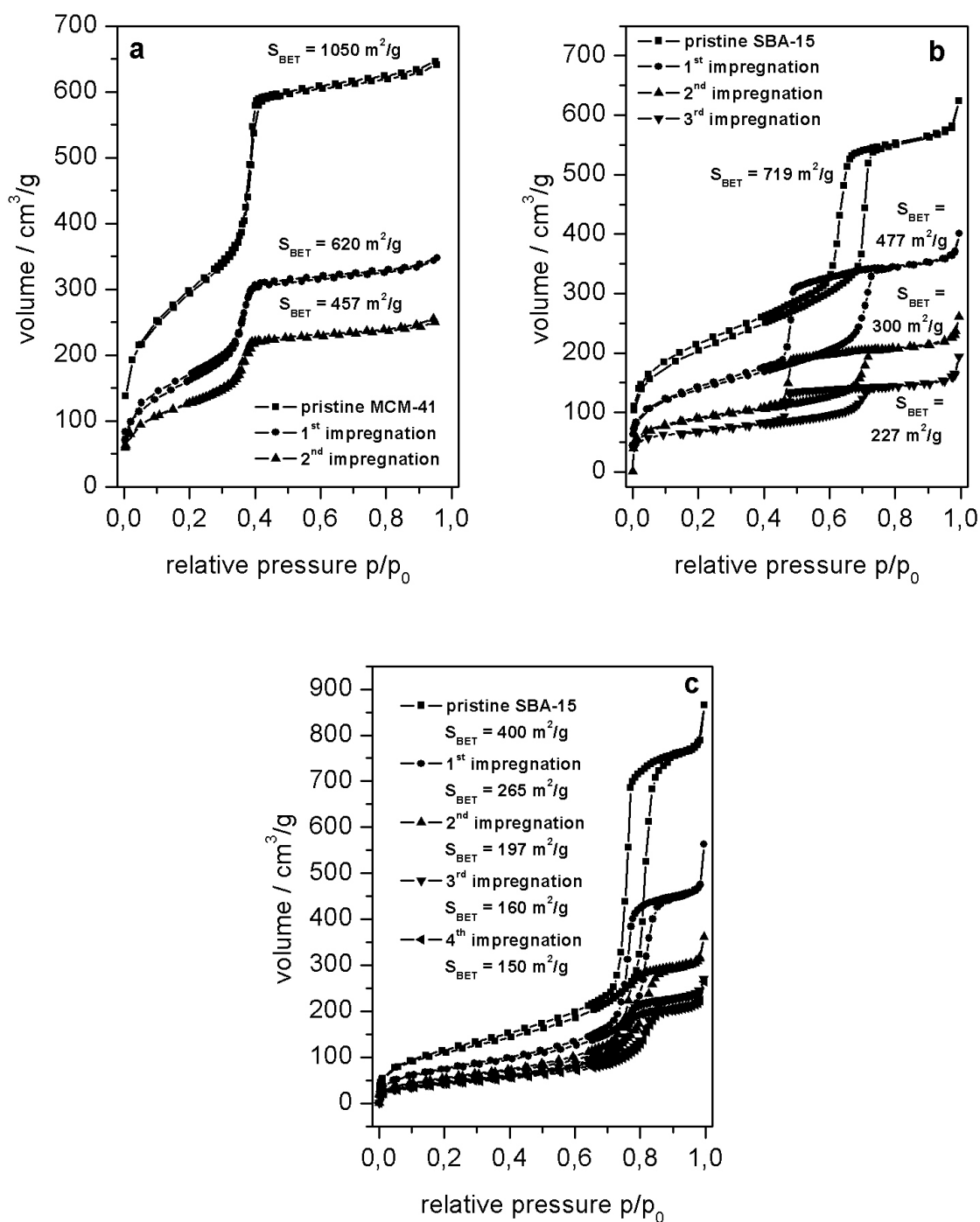


Figure 3-10: Nitrogen physisorption isotherms (77 K) at different steps of the synthesis of (a) $\text{Cd}_{0.9}\text{Mn}_{0.1}\text{S}$ in MCM-41 silica (3 nm), (b) $\text{Cd}_{0.99}\text{Mn}_{0.01}\text{S}$ in SBA-15 silica (6 nm) and (c) $\text{Zn}_{0.95}\text{Mn}_{0.05}\text{S}$ in SBA-15 silica (9 nm).

The calculated surface areas after each impregnation/conversion cycle are listed in the respective figures. At this point it must be kept in mind that the introduction of the heavy sulphides itself causes a reduction of the surface area of the mesoporous matrices.

The largest reduction of the inner surface occurs with the first impregnation step due to a better mobility of the acetates within the pores at the beginning.

In the case of the 6 nm samples a strong broadening of the hysteresis loop can be observed caused by the so-called "cavitation" phenomenon. This is observed, when smaller pores ("necks") are interconnecting wider mesopores (with pore sizes > 5 nm) [118]. In the case of nitrogen physisorption measurements these necks have to exhibit pore sizes < 4 nm for this effect to take place. Due to the introduction of the nanoparticles into the 6 nm mesopores this condition is fulfilled to that effect, that the pore texture is altered and constrictions with widths smaller than 4 nm are created, which then control the accessibility of the 6 nm mesopores. In the case of the 3 nm and the 9 nm samples, this effect is negligible, because the pores are too small, or too large, respectively, for this effect to be relevant. The difference between "cavitation" and "pore blocking" is determined by a critical width of the necks or constrictions. Pore blocking appears if this critical width is > 4 nm (for nitrogen physisorption measurements). In that case the width of the necks determines, at which relative pressure the evaporation of the fluid from within the necks and the pores takes place, *i.e.* "pore liquid" and "neck liquid" evaporate at the same time. Therefore the desorption pore size distribution can only give a statement about the width of the necks.

In the case of "cavitation" the metastable "pore liquid" evaporates before a relative pressure is reached at which the "neck liquid" can do so. This results in the formation of "bubbles" (from the "pore liquid") which diffuse through the still liquid-filled necks. The evaporation of the "neck liquid" then takes place at a lower relative pressure. In the case of cavitation controlled desorption no statement can be made about the pore size when calculating it from the desorption branch. This becomes obvious in the following, when the pore size distributions of the different host/guest compounds are analysed.

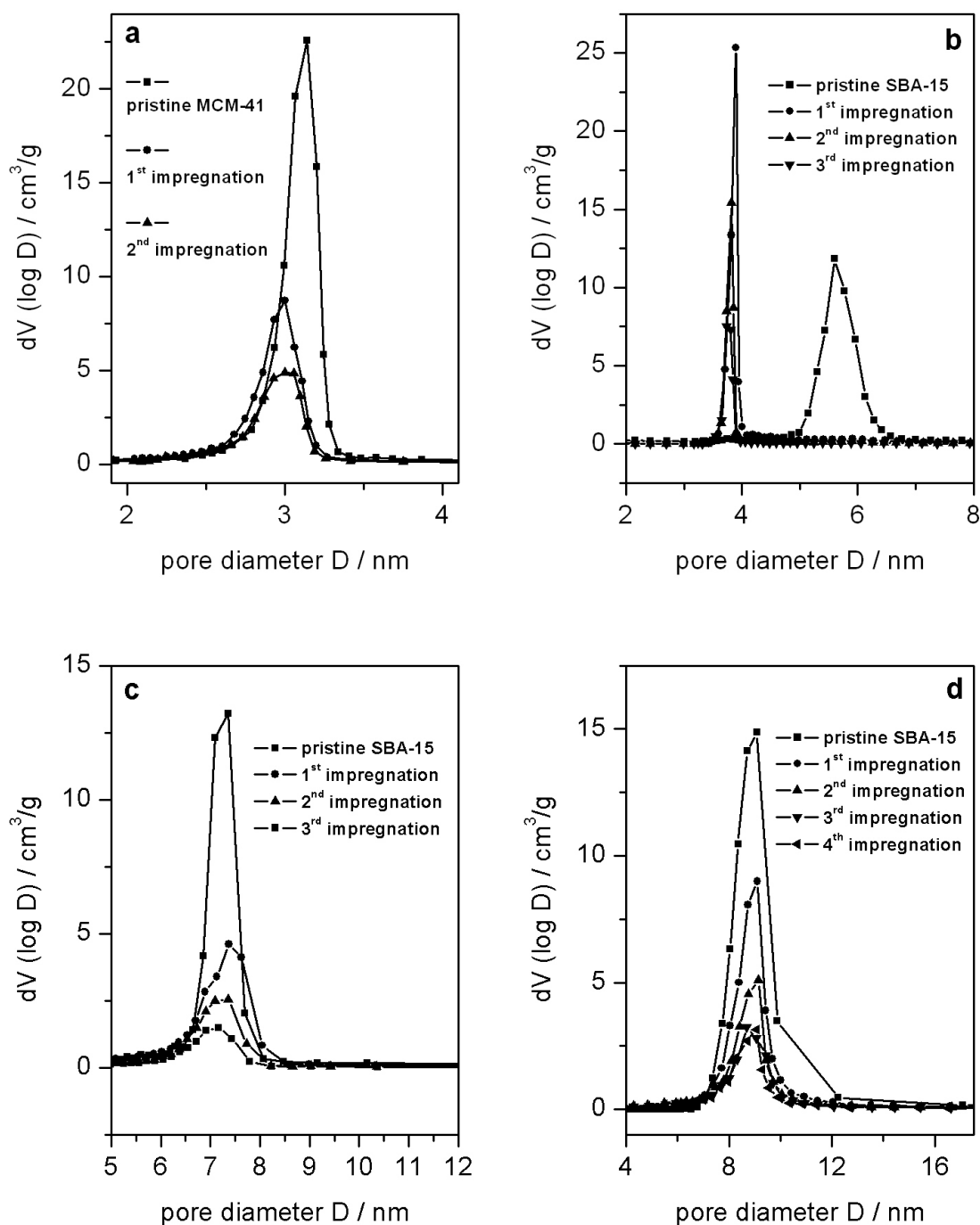


Figure 3-11: BJH pore size distributions of the nitrogen physisorption data at different steps of the synthesis of (a) $\text{Cd}_{0.9}\text{Mn}_{0.1}\text{S}$ in MCM-41 silica (3 nm), (b) and (c) $\text{Cd}_{0.99}\text{Mn}_{0.01}\text{S}$ in SBA-15 silica (6 nm) and (d) $\text{Zn}_{0.95}\text{Mn}_{0.05}\text{S}$ in SBA-15 silica (9 nm). All distributions calculated from the desorption branch, except (c) from the adsorption branch of the respective isotherms.

During the different impregnation cycles the reduction of the inner surface is accompanied with a broadening of the pore size distribution and a small decrease of the pore diameter (Figure 3-11). This is understandable, because at first, small particles are

formed mainly at the pore walls, leading to a small decrease of the pore diameter. With each following impregnation cycle the particles grow and the pores are slowly filling. Hence, the number of freely accessible pores is decreasing. In the case of the 6 nm samples though, a dramatic decrease of the pore diameter is observed after the first impregnation, when calculating the pore size distribution from the desorption branch of the sorption isotherm (*Figure 3-11 b*). The calculated value of the pore size is not trustworthy though, because in this case the desorption is controlled by the widths of the cavitations (which are caused by the incorporation of the nanoparticles). When calculating the pore size distribution from the adsorption branch this effect is avoided. Normally the calculation of the pore size from the adsorption branch is not an appropriate method, because the adsorption branch is not measured in thermodynamic equilibrium, whereas the desorption branch is [119]. This results in a calculation of too large pore sizes (in this case the pore size is about 6 nm large, whereas the calculation from the adsorption branch results in a value of larger than 7 nm). However, it allows the comparison of the pristine mesoporous silica material and the host/guest compounds. It can be seen, that the behaviour observed for the 3 nm and 9 nm samples is the same for the 6 nm series, when comparing the adsorption pore size distribution (*Figure 3-11 c*).

3.2.3. Transmission electron microscopy

In *Figure 3-12* transmission electron micrographs of different host/guest compounds are shown. All pictures reveal that the hexagonal order of the host structures has been maintained after the respective impregnation/conversion cycles.

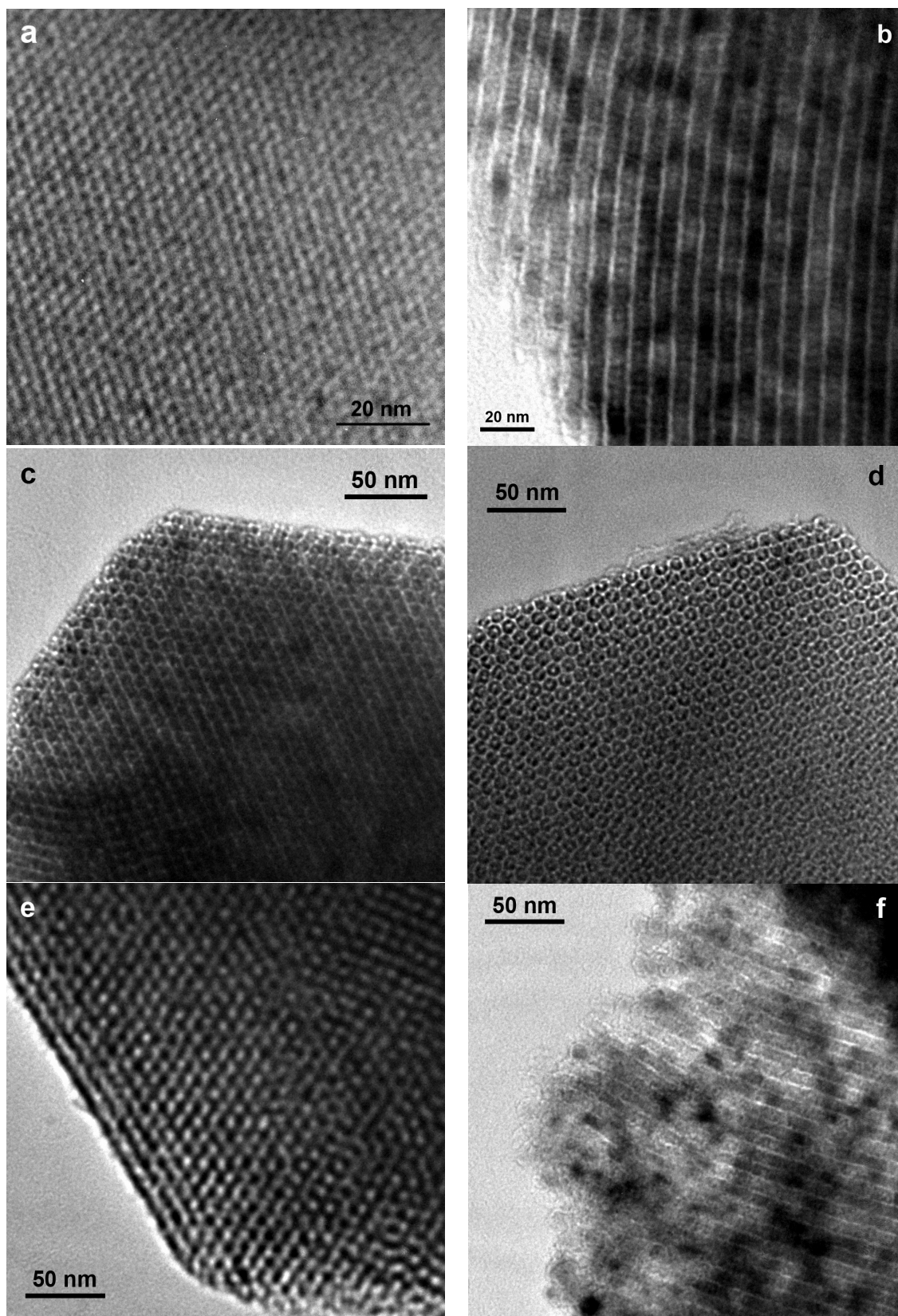


Figure 3-12: Transmission electron micrographs of (a) $\text{Cd}_{0.99}\text{Mn}_{0.01}\text{S@MCM-41}$ silica (3 nm), (b and c) $\text{Cd}_{0.99}\text{Mn}_{0.01}\text{S@SBA-15}$ silica (6 nm), (d) MnS@SBA-15 silica (6 nm), (e) MnS@SBA-15 silica (8 nm) and (f) $\text{Zn}_{0.8}\text{Mn}_{0.2}\text{S@SBA-15}$ silica (12 nm).

The TEM images in *Figure 3-12 b* and *f* are cross sectional views of the host/guest compounds. The narrow ‘white’ lines represent the SiO₂ walls of the pore systems. The dark regions are the respective DMS nanoparticles. This view perpendicular to the pores reveals that the aligned pore channels are filled with the DMS compounds. It can clearly be seen that single ‘sphere-like’ nanoparticles are present, but also that there is a tendency of these nanoparticles to agglomerate to denser ‘wire-like’ structures. There is no evidence for larger particles being formed outside the pore system, *i.e.* the entire DMS compound is confined inside the channels of the mesoporous host.

3.2.4. Infrared spectroscopy

To confirm the fact, that the conversion of the acetates to the sulphides by thermal treatment in an H₂S atmosphere is a quantitative process, infrared spectra taken after the various preparation steps during the impregnation/conversion cycle were recorded (*Table 3-3* summarises the relevant IR bands). It can be seen that the spectra of the MCM-41 silica/metal acetate host/guest compound is almost a sum of the mesoporous silica and the bulk metal acetate spectra (*Figure 3-13*).

Table 3-3: Observed IR bands and corresponding type of modes.

wavenumber / cm ⁻¹	type of mode
1570/1558 ^a	ν_{as} C=O
1423/1446 ^a	ν_{s} C=O
1229	δ Si–O
1084	ν Si–O
802	δ Si–O
460	δ Si–O

^a The first value applies to cadmium acetate, the second to zinc acetate.

After the H_2S /thermal treatment the symmetrical and asymmetrical $\text{C}=\text{O}$ valence vibration bands of the acetate ($1420\text{--}1580\text{ cm}^{-1}$) have vanished. Potentially formed acetic acid is removed by washing the samples with a certain amount of water for 30 minutes. As there are no phonon modes of the respective sulphides above 400 cm^{-1} , this suggests the quantitative conversion of the acetates to the sulphides within the pore structure.

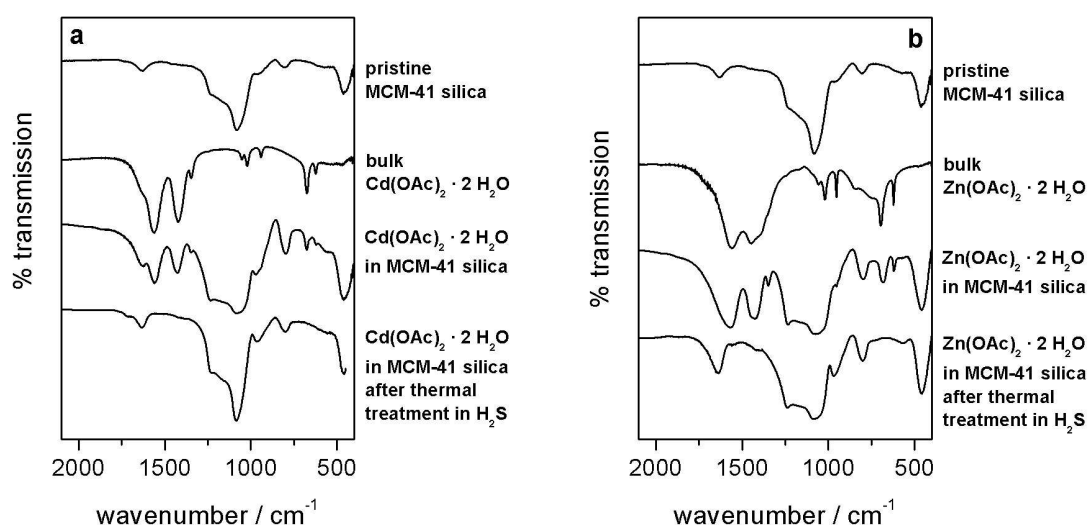


Figure 3-13: IR spectra taken at different steps of the synthesis of (a) CdS confined in MCM-41 silica and (b) ZnS confined in MCM-41 silica.

3.2.5. Raman spectroscopy

Figure 3-14 depict Raman spectra in the vicinity of the LO (longitudinal optical) phonon of bulk $\text{Zn}_{1-x}\text{Mn}_x\text{S}$ and $\text{Zn}_{1-x}\text{Mn}_x\text{S}@SBA-15$ (6 nm), respectively, with x ranging from 0.01 to 0.2. The Raman spectra of bulk $\text{Zn}_{1-x}\text{Mn}_x\text{S}$ are well understood [120]. The feature at about 350 cm^{-1} corresponds to the LO-phonon mode from the centre of the Brillouin zone (reciprocal vector $q \approx 0$). This mode slightly shifts to lower frequencies, broadens with increasing Mn-content x and develops a shoulder on the low-frequency side. The LO-phonon mode of ZnS transforms continuously into that of MnS, *i.e.* the $\text{Zn}_{1-x}\text{Mn}_x\text{S}$ system shows a one-mode behaviour. The only weak dependence of the LO-phonon frequency on x is explained by the similarity of the LO-phonon frequencies of ZnS and MnS. A value of 343 cm^{-1} has been determined for the

LO-phonon frequency of tetrahedrally coordinated MnS by IR reflectivity measurements [121]. It can be seen that with increasing x additional modes develop in the range between 310 cm^{-1} and 330 cm^{-1} . These modes arise from the X- and L-points of the Brillouin zone, where the corresponding density of states is large, and become Raman-active by Mn substitution, which perturbs the translational symmetry. The Raman spectra of the $\text{Zn}_{1-x}\text{Mn}_x\text{S}@SBA-15$ (6 nm) also show clearly the LO-phonon mode. The phonon mode is considerably broadened compared to the corresponding bulk modes, but with increasing x also develops a shoulder on the low-frequency side. Furthermore, there is no indication of the Mn-induced X,L-modes at lower Raman shifts. The strong broadening of the LO-phonon mode and the absence of the Mn-induced X,L-modes are due to the reduced dimensions of the nanoparticles. The reduction of the lateral dimensions should eventually lead to a break-down of the concept of lattice periodicity and reciprocal space. The Mn-induced modes result from the density of states with high q -values which become ill-defined and thus unobservable when the concept of reciprocal space breaks down.

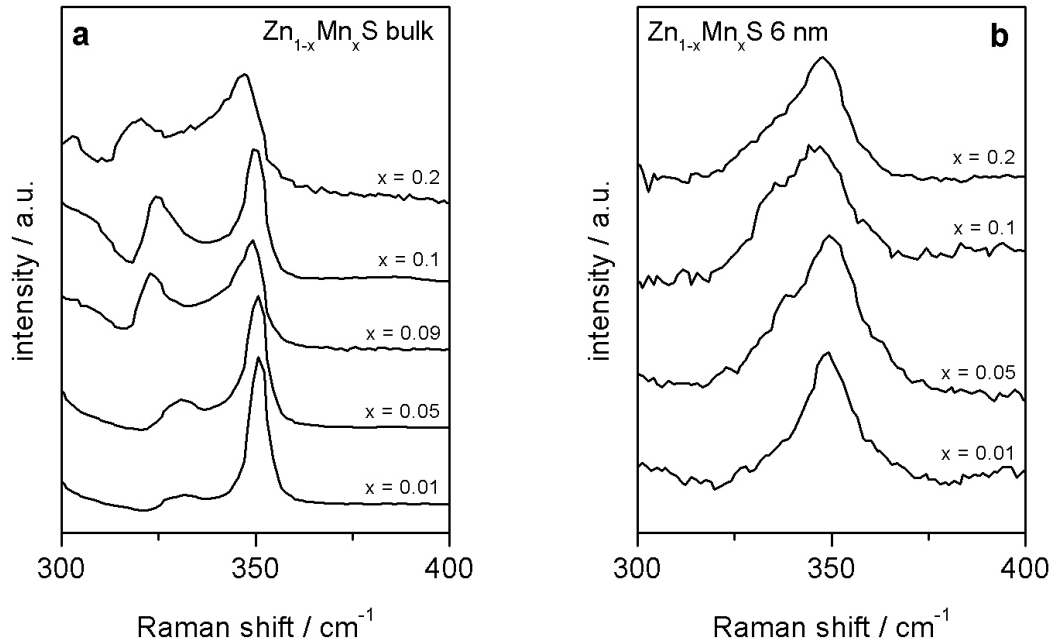


Figure 3-14: Raman spectra of (a) bulk $\text{Zn}_{1-x}\text{Mn}_x\text{S}$ of various x in the vicinity of the LO phonon and (b) $\text{Zn}_{1-x}\text{Mn}_x\text{S}@SBA-15$ silica (6 nm) in the vicinity of the LO phonon at $T = 300\text{ K}$ and laser excitation at 364 nm (3.41 eV).

The reduction of the lateral dimensions of the semiconductor structure leads to phonon confinement. This results in an additional contribution of phonons with small non-zero q to the mode with $q = 0$ [122]. This effect is a common characteristic of II/VI nanoparticles [123-125]. The admixture of modes of higher q usually leads to a red-shift of the peak position and to a broadening and concomitantly to a low-frequency wing of the LO-phonon mode as its frequency usually decreases with increasing q . These features of phonon confinement are observable in *Figure 3-15 a*. It shows the LO-phonon spectra of bulk $\text{Zn}_{0.99}\text{Mn}_{0.01}\text{S}$, $\text{Zn}_{0.99}\text{Mn}_{0.01}\text{S}@SBA-15$ silica (6 nm) and $\text{Zn}_{0.99}\text{Mn}_{0.01}\text{S}@MCM-41$ silica (3 nm). The spectra of the $\text{Zn}_{0.99}\text{Mn}_{0.01}\text{S}$ nanoparticles are strongly red-shifted and broadened with respect to the bulk reference. As expected, both effects are more significant for $\text{Zn}_{0.99}\text{Mn}_{0.01}\text{S}@MCM-41$ (3 nm) than for $\text{Zn}_{0.99}\text{Mn}_{0.01}\text{S}@SBA-15$ (6 nm).

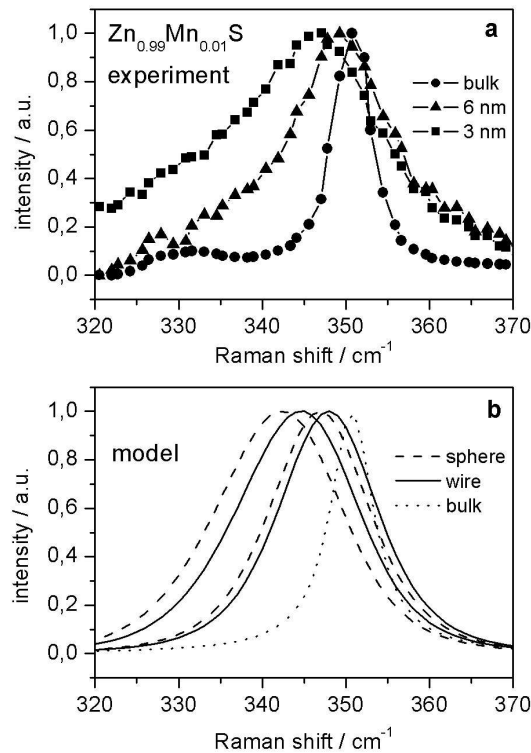


Figure 3-15: a) Raman spectra in the vicinity of the LO phonon of bulk $\text{Zn}_{0.99}\text{Mn}_{0.01}\text{S}$, $\text{Zn}_{0.99}\text{Mn}_{0.01}\text{S}@SBA-15$ (6 nm) and $\text{Zn}_{0.99}\text{Mn}_{0.01}\text{S}@MCM-41$ silica (3 nm). $T = 300$ K and laser excitation at 364 nm (3.41 eV). b) Lorentzian fit of the LO-phonon of bulk $\text{Zn}_{0.99}\text{Mn}_{0.01}\text{S}$. Calculated LO-phonon lineshapes for spherical $\text{Zn}_{0.99}\text{Mn}_{0.01}\text{S}$ nanoparticles and cylindrical $\text{Zn}_{0.99}\text{Mn}_{0.01}\text{S}$ wires with diameters of 3 nm and 6 nm.

The confined-phonon model introduced by Campbell and Fauchet yields different results for wire-like cylindrical and spherical nanoparticles [122]. The model assumes that the $q = 0$ phonon can be described by the lattice-periodic part of bulk material $u(q=0, r)$ multiplied by an envelope function $\Psi(q=0, r)$. The envelope function is determined by the shape and the dimensions of the nanoparticle. The corresponding lineshape of the LO-phonon in a nanoparticle is given by

$$I(\omega) \cong \int_{1^{st} \text{ Brillouin-zone}} d^3q \frac{|C(0, q)|^2}{(\omega_0 - \omega(q))^2 + (\Gamma_0/2)^2} \quad \text{Equation 3-1}$$

where ω_0 is the frequency of the LO-phonon at $q = 0$; $\omega(q)$ is the (spherical) bulk LO-phonon dispersion; Γ_0 is the full-width at half maximum of the bulk LO-phonon (Lorentzian) lineshape. $C(0, q)$ are the Fourier-coefficients of the envelope function $\Psi(q=0, r)$. Campbell and Fauchet give the following expressions for a sphere and a cylindrical wire of infinite length:

$$\begin{aligned} |C_{\text{sphere}}(0, q)|^2 &\cong \exp\left(-\frac{q^2 d_{\text{sphere}}^2}{16\pi^2}\right) \\ |C_{\text{wire}}(0, q_{\perp}, q_z)|^2 &\cong \exp\left(-\frac{q_{\perp}^2 d_{\text{wire}}^2}{16\pi^2}\right) \delta(q_z) \end{aligned} \quad \text{Equation 3-2}$$

where d_{sphere} and d_{wire} are the diameters of the sphere and the wire, respectively. q_{\perp} and q_z are the q -vectors perpendicular and parallel to the wire axis. Using the $d^3q = 4\pi q^2 dq$ for the sphere and $d^3q = 2\pi q_{\perp} dq_{\perp} dq_z$ for the infinite wire allows one to calculate the LO-phonon lineshape for wire-like and spherical nanoparticles of different diameters using Equation 3-1.

The model was applied to analyse the lineshapes of $\text{Zn}_{0.99}\text{Mn}_{0.01}\text{S}$ nanoparticles shown in Figure 3-15 a. For the phonon-dispersion $\omega(q)$ that along the Δ -direction of the Brillouin-zone of zincblende ZnS bulk was used [126]. To determine Γ_0 , the LO-phonon spectrum of bulk $\text{Zn}_{0.99}\text{Mn}_{0.01}\text{S}$ (Figure 3-15 a) was fitted by a Lorentzian lineshape. The fit (Figure 3-15 b) yielded $\Gamma_0 \approx 6 \text{ cm}^{-1}$. However, the linewidths of the

confined-phonon lineshapes calculated using these parameters are too narrow compared to the experimental results. A better agreement was obtained by using $\Gamma_0 \approx 20 \text{ cm}^{-1}$. It is well known that the linewidths of the bulk LO-phonon are very sensitive to the degree of crystallinity of the material and that the degree of crystallinity itself usually increases with increasing synthesis temperature. Thus, the larger Γ_0 for the $\text{Zn}_{0.99}\text{Mn}_{0.01}\text{S}$ nanostructures reflects simply the differences in the synthesis of the nanostructures and the bulk reference samples used in the Raman experiments. The latter were synthesised at much higher temperatures (about 1000°C). The synthesis temperature of the nanostructures was considerably lower to minimize diffusion of the Mn to the surface, which, in contrast to bulk-material synthesis, is a severe problem in the synthesis of nanostructures because of their larger surface to volume ratio. It is worth noting that the red-shift of the maximum of the confined-phonon lineshape with respect to ω_0 as a function of the diameter exhibits only a weak dependence on Γ_0 for both wires and spheres. *Figure 3-15 b* depicts LO-phonon lineshapes for spherical $\text{Zn}_{0.99}\text{Mn}_{0.01}\text{S}$ nanoparticles and cylindrical $\text{Zn}_{0.99}\text{Mn}_{0.01}\text{S}$ wires with diameters of 3 nm and 6 nm calculated using $\Gamma_0 = 20 \text{ cm}^{-1}$. It demonstrates that with respect to ω_0 the red-shift of the maximum of the confined-phonon lineshape is smaller for wires than for spheres of the same diameter. The red-shifts observed in the experiment show a better agreement with those calculated for wire-shaped nanostructures of the same nominal diameter. The red-shifts calculated for spherical particles are too large. Like already described in *Chapter 3.2.3*, this does not support the concept of "nano-wires" inside the mesoporous matrices, but can be tentatively interpreted as a sign that the average (Zn,Mn)S nanoparticles incorporated into the SiO_2 pores have an elongated spherical or ellipsoidal shape, *i.e.* the lateral extensions are close to the pore diameter and the extensions along the pore axis are larger than the pore diameter.

3.2.6. X-ray absorption spectroscopy

X-ray absorption spectroscopy is the method of choice to distinguish whether the pore system contains two binary sulphides, AS (A = Cd or Zn) and MnS, or the ternary (II,Mn)VI compound, $A_{1-x}Mn_xS$, with the Mn^{2+} ions distributed randomly inside the AS matrix. In order to investigate the local structure around the Mn^{2+} ions, X-ray absorption spectroscopy at the K-edges of manganese, zinc and cadmium was carried out. *Figure 3-16* displays the normalized X-ray absorption near edge structure (XANES) regions of the spectra of $Cd_{0.7}Mn_{0.3}S$ and $Zn_{0.7}Mn_{0.3}S$ confined in 3, 6 and 9 nm pores, recorded at the respective K-edges of Cd, Zn and Mn. The XANES region of the spectra can be used as a “fingerprint” of the respective material. It can clearly be seen, that the spectra of $Cd_{0.7}Mn_{0.3}S$ and $Zn_{0.7}Mn_{0.3}S$ at the K-edges of the Cd and Zn are very similar to the respective binary bulk sulphide (*Figure 3-16 a*). This is an indication that the crystal field around the respective A cation of the nanostructured samples is the same as the bulk binary II/VI compound (CdS or ZnS, respectively).

In contrast to that it can be seen from *Figure 3-16 b*, that exactly the same features in the XANES region of the MnS reference (wurtzite structure) are not found in the spectra of the nanostructured manganese doped II/VI semiconductors. Hence, manganese must be present in the samples, giving rise to the absorption edge at 6539 keV, but the crystal structure around the Mn ions differs from that of the binary bulk MnS. The energy position of the absorption edge is the same for all nanostructured samples as well as the reference MnS, indicating no characteristic valence shift of the incorporated manganese; hence only Mn^{2+} is present in the nanostructured $A_{1-x}Mn_xS$ compounds.

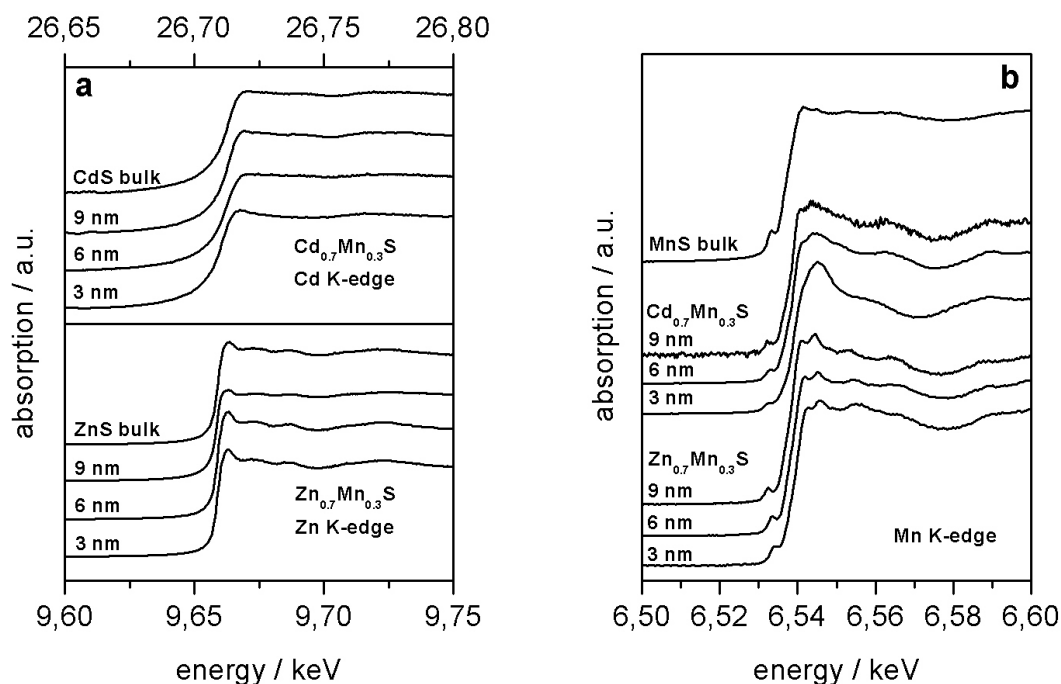


Figure 3-16: Normalised XANES spectra of $\text{Cd}_{0.7}\text{Mn}_{0.3}\text{S}$ and $\text{Zn}_{0.7}\text{Mn}_{0.3}\text{S}$ confined in 3, 6 and 9 nm pores at (a) the Cd K-edge (top) and Zn K-edge (bottom) and (b) at the Mn K-edge, together with the respective binary sulphides CdS, ZnS and MnS (all wurtzite structure).

The results from the XANES region of the X-ray absorption spectroscopy are a first indication for the doping of the II/VI semiconductors with randomly distributed Mn^{2+} ions.

If CdS and ZnS, respectively, are doped with Mn^{2+} ions, the crystal structure of the nanostructured $\text{A}_{1-x}\text{Mn}_x\text{S}$ compounds can only be those of the binary sulphides, that is zincblende or wurtzite. The zincblende structure can be described as consisting of a ccp array of the sulphide anions with the tetrahedral sites filled with the A cations. The wurtzite structure consist of a hcp array of sulphide anions also with the tetrahedral sites filled with the A cations. Thus, both structures consist of ions with tetrahedrally coordinated next neighbours. The atomic distances of the two structure types are very similar in the first three coordination spheres, the difference in the structures is only visible from the coordination number of the third coordination sphere on (Table 3-4 and also Figure 1-7).

Table 3-4: Comparison of the calculated values for the atomic distances (*R*) and coordination numbers (*CN*) for the first three coordination spheres (*CS*) of the respective metal ion (*Cd*, *Zn* or *Mn*) in zincblende and wurtzite structures of *CdS*, *ZnS* and *MnS*.

CdS					ZnS					MnS		
		zincblende (ccp)		wurtzite (hcp)			zincblende (ccp)		wurtzite (hcp)			wurtzite (hcp)
CS	R / Å	CN	R / Å	CN	CS	R / Å	CN	R / Å	CN	CS	R / Å	CN
S	2.52	4	2.53	4	S	2.31	4	2.34	4	S	2.43	4
Cd	4.11	12	4.13	12	Zn	3.78	12	3.82	12	Mn	3.96	12
S	4.82	12	4.85	10	S	4.43	12	4.48	10	S	4.66	12

For a detailed analysis of the local geometry of the Mn^{2+} ions inside the II/VI semiconductor compounds, the EXAFS (extended X-ray absorption fine structure) region of the X-ray absorption spectra recorded at the Mn K-edge of the different host/guest compounds have to be evaluated. After conventional data analyses, *i.e.* energy calibration, background subtraction and normalisation of the edge- jump, the k^3 -weighed data were Fourier transformed using a Bessel window. In *Figure 3-17* the not phase-corrected radial distribution functions of the Mn K-edge spectra of $\text{Cd}_{1-x}\text{Mn}_x\text{S}$ and $\text{Zn}_{1-x}\text{Mn}_x\text{S}$ incorporated within three different pore structures are shown.

The small particle size and a certain degree of disorder in the nanoparticles is the reason for the lack of peaks for the higher coordination spheres in the radial distribution functions. In the case of the $\text{Zn}_{1-x}\text{Mn}_x\text{S}$ samples the first two shells (Mn-S and Mn-Zn) are visible, in the $\text{Cd}_{1-x}\text{Mn}_x\text{S}$ particles even only the Mn-S shell. This restricts the EXAFS evaluation in such a way that no statement can be made about the crystal structure of the nanoparticles, for both eligible structures have the same number of nearest neighbours and very similar atomic distances.

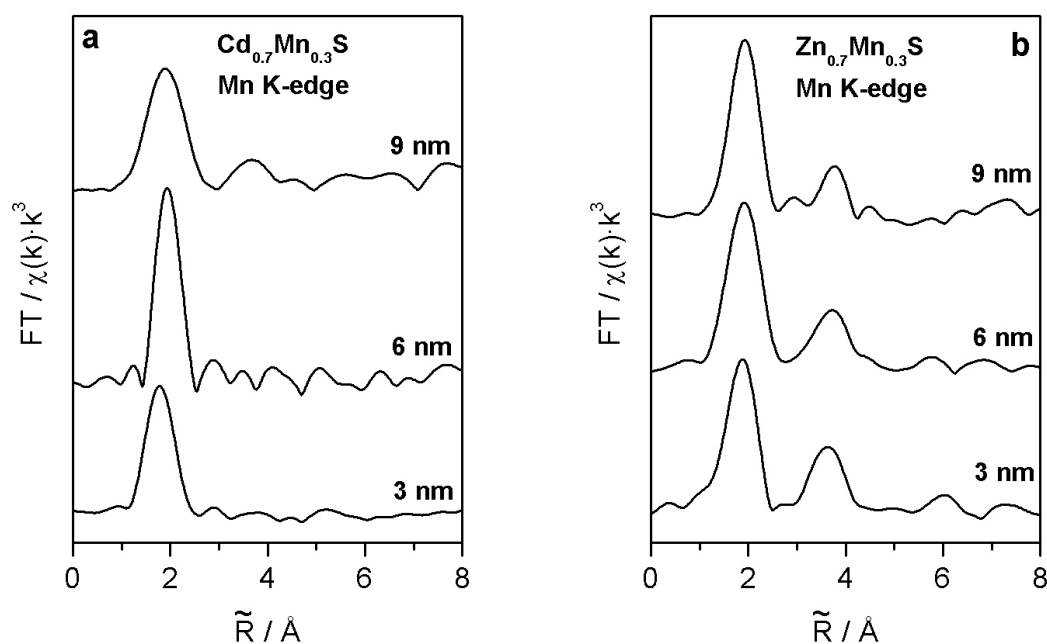


Figure 3-17: Modified radial distribution functions (*m-RDF*, not phase-corrected) of the Mn K-EXAFS spectra of (a) $\text{Cd}_{0.7}\text{Mn}_{0.3}\text{S}$ and (b) $\text{Zn}_{0.7}\text{Mn}_{0.3}\text{S}$ confined in 3, 6 and 9 nm mesoporous silica.

Table 3-5 summarises the fit results for all samples, in Figure 3-18 the fits are shown. The first shell (Mn-S in all nanoparticles) is slightly shifted to smaller distances for all incorporated samples, compared to the Mn-S distance in pure MnS (2.42 Å for wurtzite). For the 3 nm particles the shift is larger than for the 6 and 9 nm samples, indicating a stronger distortion of the crystal structure due to the even more reduced dimensions. In the case of the $\text{Cd}_{0.7}\text{Mn}_{0.3}\text{S}$ nanoparticles the deviation from the distance between cadmium and sulphur, which would be observed for the binary compound (2.53 Å for wurtzite), is strong, whereas in the case of the $\text{Zn}_{0.7}\text{Mn}_{0.3}\text{S}$ nanoparticles the extracted value lies in between the distance of zinc and sulphur in pure ZnS (2.34 Å for wurtzite) and manganese and sulphur in pure MnS. For both nanoparticle series the observed distances are close to the values for binary MnS which is an indication for a distorted local "MnS" geometry around the respective manganese atoms in the ternary compounds.

In the case of the nanostructured $\text{Cd}_{0.7}\text{Mn}_{0.3}\text{S}$ the next-nearest neighbour coordination sphere is not visible, probably due to the large amount of the strongly

absorbing cadmium atoms in the samples and the only small percentage of manganese. For the incorporated diluted magnetic semiconductors $\text{Zn}_{0.7}\text{Mn}_{0.3}\text{S}$ the next-nearest neighbour distance (Mn-Zn) is within a minor deviation again nearly the same as in pure bulk MnS. The corresponding Mn-Mn distance would be 3.96 Å, and a good agreement can be observed for all samples. The associated coordination numbers are only slightly smaller than in MnS. These effects can be explained by a small local disorder in the ZnS matrix arising from the substitution of zinc by manganese leading to a distorted "MnS" geometry.

Table 3-5: Fit results of the Mn K-EXAFS measurements. Abbreviations: N = coordination number, R = atomic distance, $\Delta\sigma^2$ = Debye-Waller factor.

sample	shell	N	R / Å	$\Delta\sigma^2 / \cdot 10^{-3} \text{ Å}^2$
$\text{Cd}_{0.7}\text{Mn}_{0.3}\text{S@MCM-41}$ (3 nm)	Mn-S	4.00	2.36	9.3
$\text{Cd}_{0.7}\text{Mn}_{0.3}\text{S@SBA-15}$ (6 nm)	Mn-S	4.00	2.42	6.2
$\text{Cd}_{0.7}\text{Mn}_{0.3}\text{S@SBA-15}$ (9 nm)	Mn-S	4.00	2.44	9.9
$\text{Zn}_{0.7}\text{Mn}_{0.3}\text{S@MCM-41}$ (3 nm)	Mn-S	4.00	2.38	6.0
	Mn-Zn	11.10	3.95	17.1
$\text{Zn}_{0.7}\text{Mn}_{0.3}\text{S@SBA-15}$ (6 nm)	Mn-S	4.00	2.41	8.3
	Mn-Zn	11.40	3.98	16.6
$\text{Zn}_{0.7}\text{Mn}_{0.3}\text{S@SBA-15}$ (9 nm)	Mn-S	4.00	2.41	6.6
	Mn-Zn	10.24	3.98	16.9

From these results it can be concluded that the amount of manganese ions aggregated at the surface of the nanoparticles is very small, for the fits would not yield such a good congruence with the experimental data if the coordination number was significantly lower than 4, which had to be the case for surface-near manganese atoms. It can be concluded that manganese really substitutes the A cations in the nanocrystalline structure and nanocrystals of a $\text{A}_{1-x}\text{Mn}_x\text{S}$ type are formed.

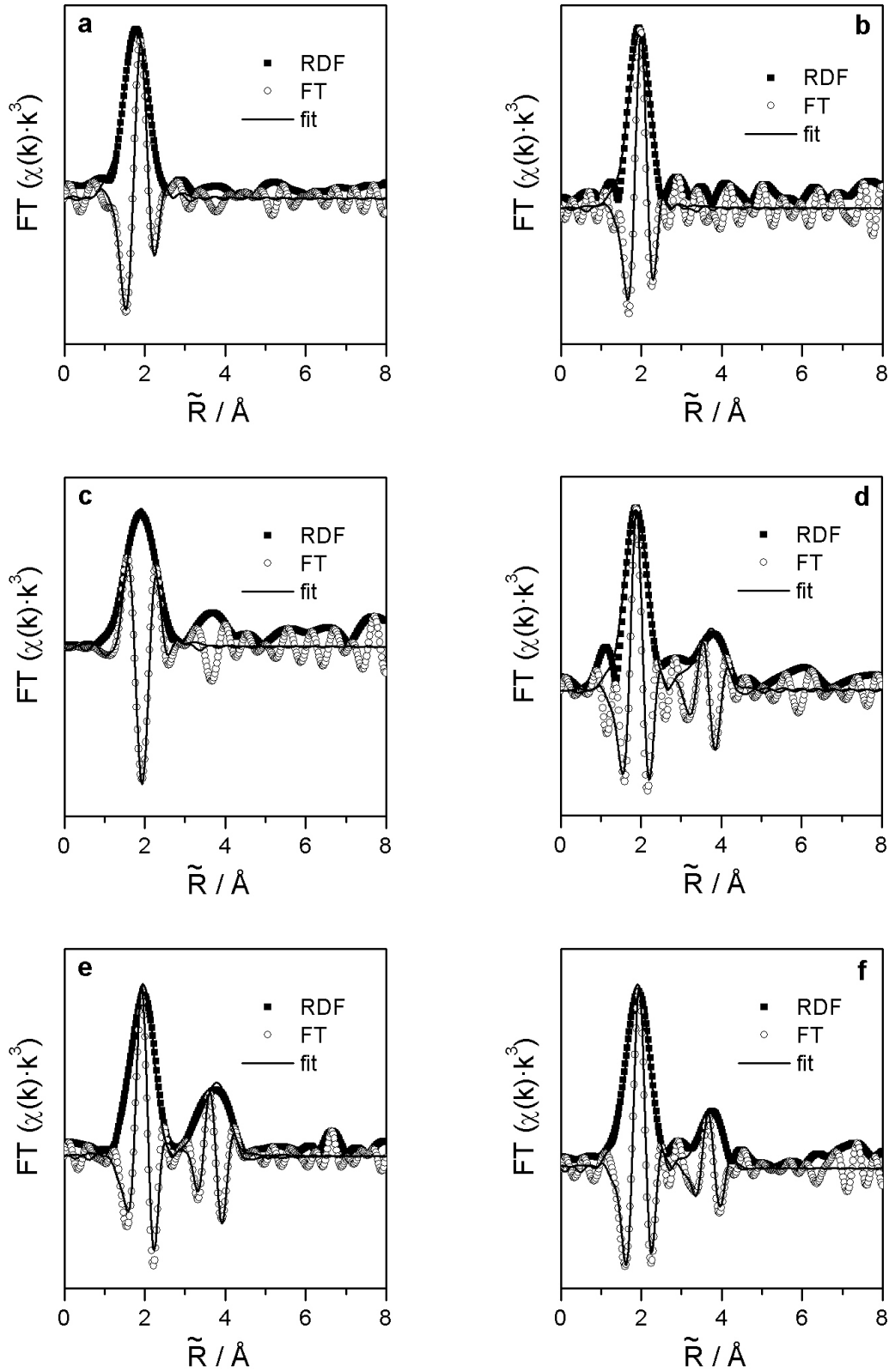


Figure 3-18: Radial distribution functions (RDF), Fourier transforms (FT) and fits of $\text{Cd}_{0.7}\text{Mn}_{0.3}\text{S}$ nanoparticles confined in (a) 3 nm, (b) 6 nm and (c) 9 nm mesoporous silica and of $\text{Zn}_{0.7}\text{Mn}_{0.3}\text{S}$ nanoparticles confined in (d) 3 nm, (e) 6 nm and (f) 9 nm mesoporous silica, regardless of multi-scattering paths. Where possible the fit was carried out for two shells.

However, it is not possible to distinguish whether the nanocrystals are of wurtzite or zincblende structure. For bulk $\text{Zn}_{1-x}\text{Mn}_x\text{S}$ the crystal structure is known to be zincblende for $x < 0.1$ and wurtzite for $0.1 < x < 0.45$. With the passage from bulk to nanocrystals the crystal structure changes though [127,128]. Also there are reports on manganese doped CdS nanoclusters confined in mesoporous silica matrices with both zincblende and wurtzite structure [96,129].

3.2.7. Band gap and optical properties

With photoluminescence (PL) and photoluminescence excitation (PLE) spectroscopy it is possible to measure the band gap variation in dependence on particle size and doping level x . *Figure 3-19* and *Figure 3-20* depict exemplarily the PL and PLE spectra of $\text{Cd}_{1-x}\text{Mn}_x\text{S}@ \text{MCM-41}$ silica (3 nm) and $\text{Zn}_{1-x}\text{Mn}_x\text{S}@ \text{SBA-15}$ silica (6 nm) for different x . The PL spectra (*Figure 3-19*) of the samples with $x > 0.01$ consist basically of one emission band at about 600 nm. This so called yellow PL band originates from the ${}^4\text{T}_1$ to ${}^6\text{A}_1$ transition within the $3d^5$ shell of Mn^{2+} on a cation site with tetrahedral symmetry (see also *Figure 2-5*). It is a common feature in wide-gap manganese doped II-VI semiconductors [84,130,131]. No band-gap related excitonic PL is observable due to the efficient energy transfer from the $\text{Zn}_{1-x}\text{Mn}_x\text{S}$ band states into the Mn^{2+} subsystem.

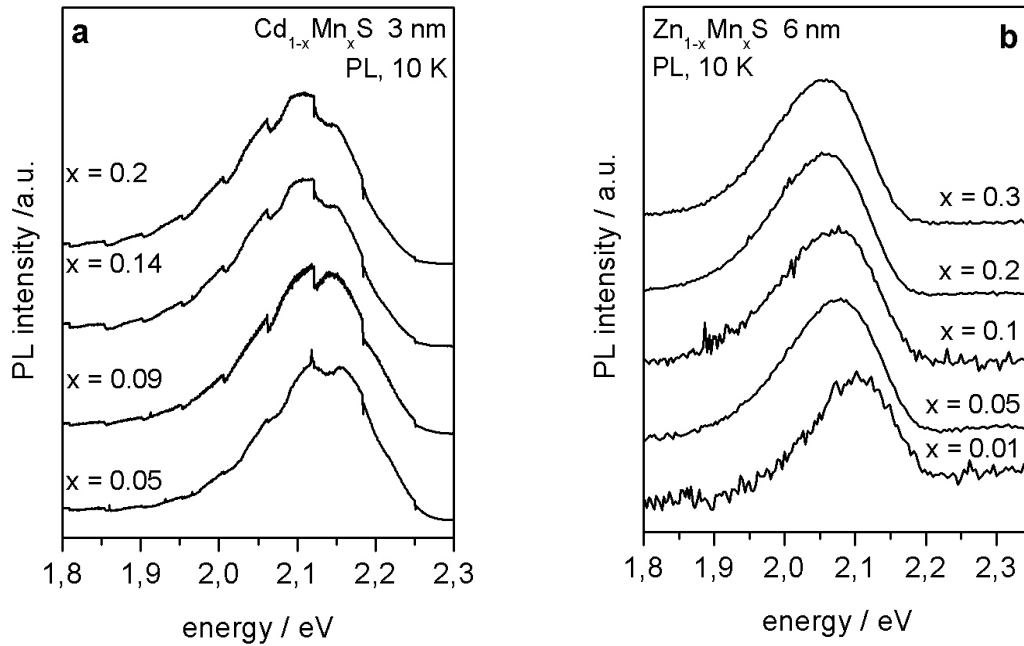


Figure 3-19: (a) PL spectra of $\text{Cd}_{1-x}\text{Mn}_x\text{S}@MCM-41$ silica (3 nm) for various x . (b) PL spectra of $\text{Zn}_{1-x}\text{Mn}_x\text{S}@SBA-15$ silica (6 nm) for various x . $T = 10$ K.

The PLE spectra of the $\text{Zn}_{1-x}\text{Mn}_x\text{S}$ samples (Figure 3-20 b) show a distinct series of peaks. The direct absorption of the $\text{Mn}^{2+} 3d^5$ shell causes the signals at lower energies. They correspond to transitions from the 6A_1 ground state to the higher excited states 4T_1 , 4T_2 and 4E , 4A_1 . The energy positions of the Mn^{2+} internal transitions serve as a probe of the crystal field at the Mn site. Assuming that excitonic recombination processes and the energy transfer into the Mn-system only show a weak dependence on x , the increase in intensity of the internal transitions with respect to the band-gap related feature reflects the increase of the direct absorption of the $3d$ shell of Mn^{2+} with increasing x . It confirms that most of the Mn-ions are incorporated in the $\text{Zn}_{1-x}\text{Mn}_x\text{S}$, *i.e.* that there is no significant Mn-diffusion to the surface. Thus, the results from the X-ray absorption measurements that the Mn^{2+} ions are incorporated on the tetrahedrally-coordinated Zn sites of the ZnS lattice forming a $\text{Zn}_{1-x}\text{Mn}_x\text{S}$ semiconductor, are confirmed. The transition energies of the Mn-internal transitions are approximately independent of x up to $x = 0.3$. The increase in intensity is only due to the increasing overall amount of manganese throughout the series.

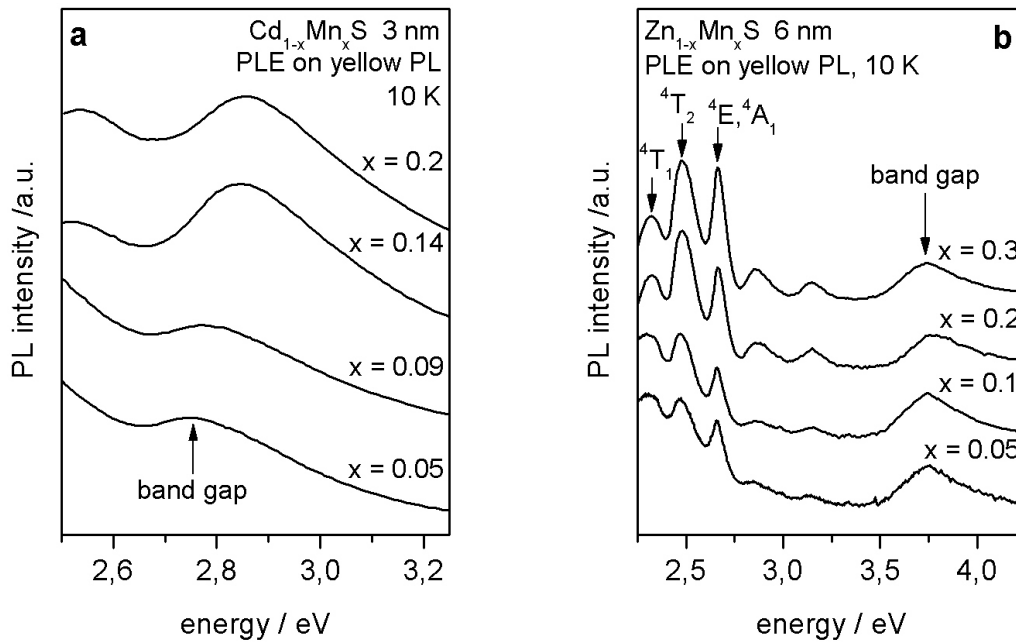


Figure 3-20: (a) PLE spectra of $\text{Cd}_{1-x}\text{Mn}_x\text{S}$ @MCM-41 silica (3 nm) for various x . (b) PLE of $\text{Zn}_{1-x}\text{Mn}_x\text{S}$ @SBA-15 silica (6 nm) for various x . $T = 10$ K.

The broader excitation band at the highest energies is the band-to-band transition of the nanoparticles (Figure 3-20 a and b). This signal is only observed because of the efficient energy transfer from the band states into the $\text{Mn}^{2+} 3d^5$ shell (see also Figure 2-5). The band gap shows quantum confinement, but in the case of the $\text{Zn}_{1-x}\text{Mn}_x\text{S}$ samples only a weak dependence on Mn concentration. This is due to the fact that the band gaps of bulk ZnS and MnS are very similar, 3.78 eV and 3.7 eV, respectively [132,133]. In the case of $\text{Cd}_{1-x}\text{Mn}_x\text{S}$ nanoparticles the dependence of the band gap energy on the doping level x is much more distinctive (see also Figure 3-23), because the difference in the respective band gap energies of the binary compounds is much higher (2.45 eV for CdS) [96, 134].

In Figure 3-21 the PLE spectra of $\text{Cd}_{0.99}\text{Mn}_{0.01}\text{S}$ and $\text{Zn}_{0.7}\text{Mn}_{0.3}\text{S}$ confined within 3, 6 and 9 nm pores are shown. The band gap related feature shifts to higher energy with decreasing particle diameter, *i.e.* shows a quantum confinement effect. However, the energy positions of the Mn^{2+} internal transitions remain unaffected by the particle size, demonstrating again that the energy positions are only determined by the local

tetrahedral crystal field of the Mn site (shown for the $\text{Zn}_{1-x}\text{Mn}_x\text{S}$ samples in *Figure 3-21 b*). Again, the increase in intensity can be explained by the increasing overall amount of manganese, when going from the 3 nm over the 6 nm to the 9 nm particles.

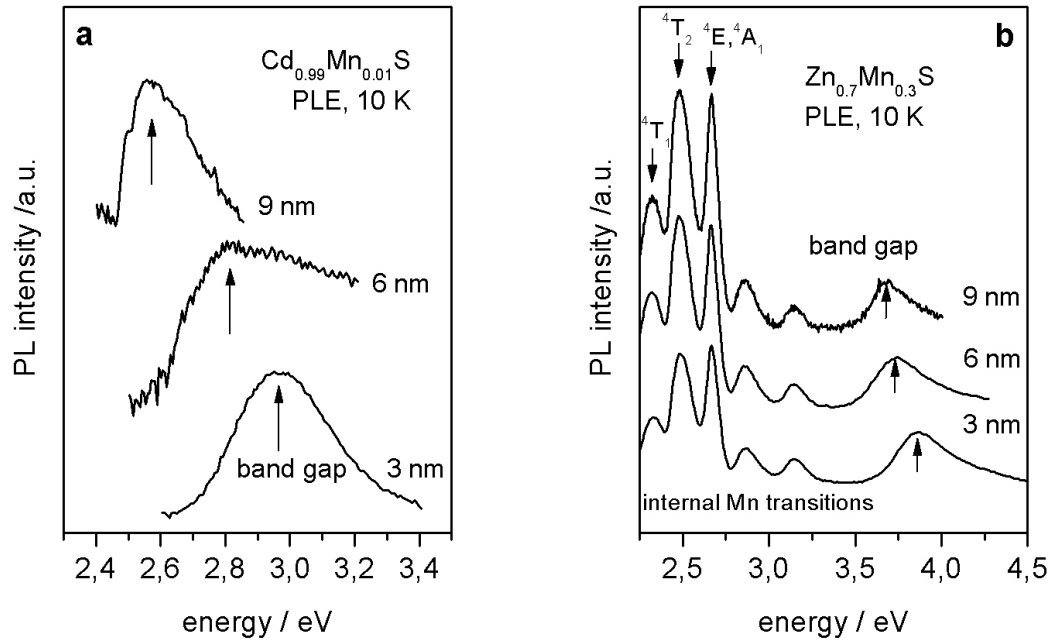


Figure 3-21: PLE spectra of (a) $\text{Cd}_{0.99}\text{Mn}_{0.01}\text{S}$ and (b) $\text{Zn}_{0.7}\text{Mn}_{0.3}\text{S}$ confined within 3, 6 and 9 nm pores of MCM-41 silica and SBA-15 silica, respectively.

The fact that the energy positions of the Mn-internal transitions depend strongly on the crystal field of the Mn-site can be analysed using the Tanabe-Sugano model [135] as a function of the crystal-field parameter Dq with the Racah parameters $B = 50$ meV and $C = 434$ meV. In *Figure 3-22* the calculated energies of the excited states of a $\text{Mn}^{2+} 3d^5$ ion in a T_d symmetric ligand field are depicted as a function of Dq . Comparing the calculated energy positions with the experimentally observed positions allows one to deduce the crystal-field parameter Dq . For the 3 nm and 6 nm $\text{Zn}_{1-x}\text{Mn}_x\text{S}$ particles the best agreement is obtained for $Dq = 0.64$ and in case of the 9 nm particles for $Dq = 0.65$. For bulk $\text{Zn}_{0.9}\text{Mn}_{0.1}\text{S}$ $Dq = 0.64$ was obtained. As Dq is indirectly proportional to the fifth power of the anion-cation distance it can be concluded that the Mn-S bond length in all $\text{Zn}_{1-x}\text{Mn}_x\text{S}$ wires is comparable to that of bulk $\text{Zn}_{1-x}\text{Mn}_x\text{S}$.

within about $\pm 1\%$. The good agreement between experiment and theory also confirms that the majority of the Mn-ions in the nanoparticles are tetrahedrally coordinated.

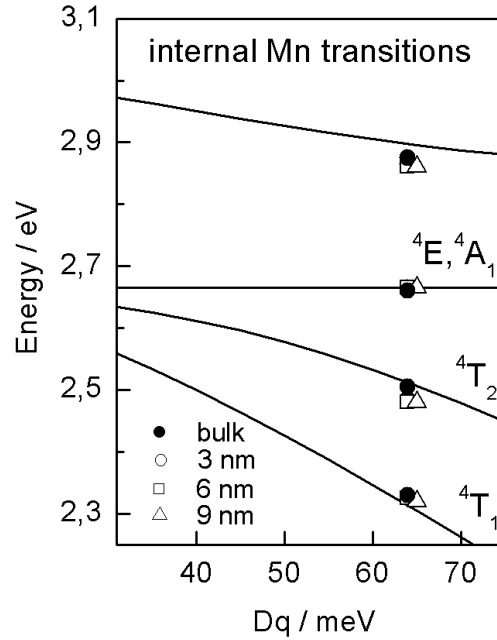


Figure 3-22: Energies of the internal transitions of Mn^{2+} ions in a T_d symmetric crystal field versus the field parameter Dq using the Racah parameters $B = 50\text{meV}$ and $C = 434\text{meV}$, calculated in the framework of the Tanabe-Sugano model (solid lines). Experimental points for $\text{Zn}_{0.9}\text{Mn}_{0.1}\text{S}$ bulk and $\text{Zn}_{0.7}\text{Mn}_{0.3}\text{S}$ nanoparticles of 3, 6 and 9 nm.

Figure 3-23 gives a comparison of the energy positions of the band gaps of three different DMS nanoparticles series with different diameters as a function of Mn-content x . The quantum confinement of the excitons in the nanoparticles evokes an increase in the direct band gap of about 350 meV for 3 nm $\text{Cd}_{1-x}\text{Mn}_x\text{Se}$ nanoparticles compared to bulk. For the corresponding $\text{Cd}_{1-x}\text{Mn}_x\text{S}$ nanoparticles the confinement is only about 200 meV. In case of the 3 nm $\text{Zn}_{1-x}\text{Mn}_x\text{S}$ the confinement energy compared to bulk is about 180 meV. The decrease of the confinement energy going from (Cd,Mn)Se via (Cd,Mn)S to (Zn,Mn)S has two major reasons: (1) the exciton Bohr radius decreases throughout the series and (2) the corresponding bulk band gap increases, *i.e.* reduces the height of the confining potential given by the band gap difference between the SiO_2 barrier and (II,Mn)VI semiconductor. The (Cd,Mn)S as well as the (Zn,Mn)S nanoparticle series clearly show, as mentioned above, that the confinement effects increase with decreasing

particle diameter. For both series the energy positions for the 9 nm particles correspond almost to those of the bulk band gaps.

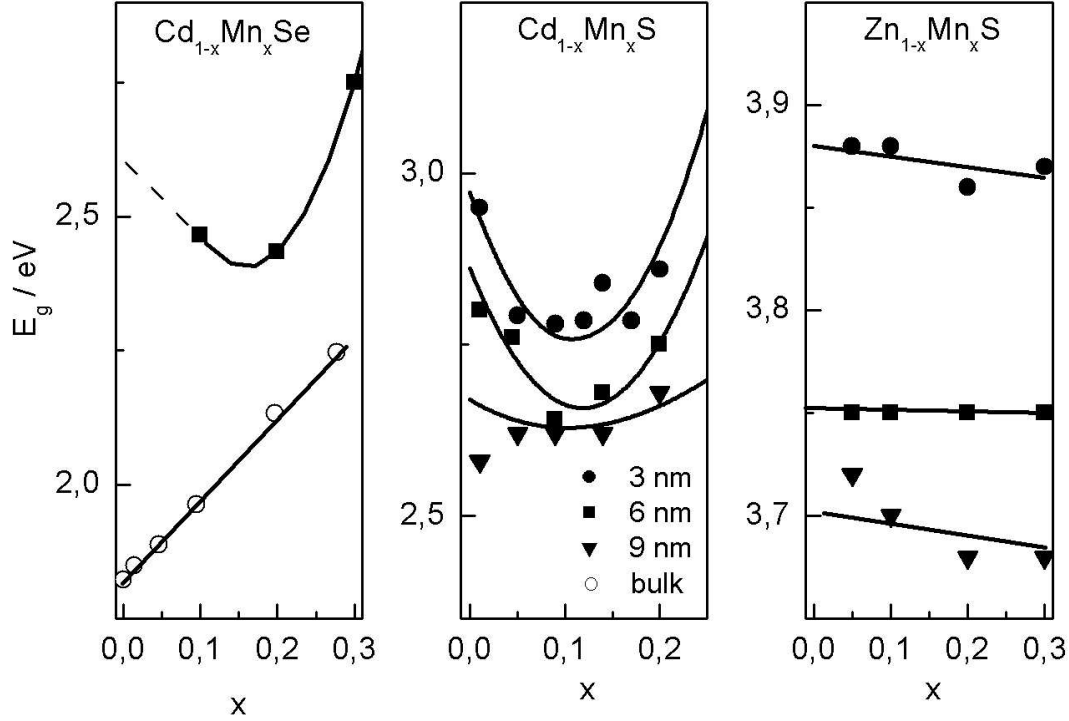


Figure 3-23: Band gaps of $\text{Cd}_{1-x}\text{Mn}_x\text{Se}$ nanoparticles (left), $\text{Cd}_{1-x}\text{Mn}_x\text{S}$ nanoparticles (middle) and $\text{Zn}_{1-x}\text{Mn}_x\text{S}$ nanoparticles (right) of different diameters as a function of composition x at $T = 10$ K. The solid lines are guide to the eye.

An interesting result is that both Cd-based systems exhibit a larger bowing of the band gap depending on the Mn-concentration than do the corresponding bulk samples. This agrees with results reported for (Cd,Mn)S quantum dots by Levy et al. [95], who also showed that the exchange interaction-induced band gap bowing becomes stronger with decreasing diameter for (Cd,Mn)S quantum dots synthesised in reverse micelles. Such a bowing is known for various bulk wide-gap (II,Mn)VI semiconductors [136-139]. Bylsma et al. derived the following expression for the band gap as a function of temperature T and Mn-concentration x in DMS [140]:

$$E_g(x, T) = E_0 + \Delta E x - \frac{AT^2}{T+B} - C\chi T \quad \text{Equation 3-3}$$

where E_0 is the band gap energy of the binary II/VI compound, ΔE the linear shift towards the band gap energy of MnS and A, B and C are Varshni-parameters. The first three terms represent the commonly used description of the energy gap of a semiconductor compound comprising a linear shift in composition and a Varshni-like temperature dependence. The last term is specific to DMS and causes the bowing. It describes a contribution due to the magnetic susceptibility χ of the Mn ions. Both, the coupling constant C as well as magnetic susceptibility χ , may be affected by the reduction of the lateral dimensions. The coupling constant C is given by:

$$C \propto 3m_c\alpha^2 + \left(m_{hh} + \frac{2}{3}m_{lh}\right)\beta^2 \quad \text{Equation 3-4}$$

where m_c , m_{hh} and m_{lh} are the conduction-band and valence-band masses and α and β are the s - d and p - d coupling parameters. As $\alpha \ll \beta$ and $m_{hh}, m_{lh} > m_c$ in (II,Mn)VI, the magnitude of C is mainly determined by β for which Larson et al. give the following expression [141]:

$$\beta = -32 \frac{V_{pd}^2}{N_0} \left[\frac{1}{E_v + U_{eff} - E_{3d}} + \frac{1}{E_v - E_{3d}} \right] \quad \text{Equation 3-5}$$

where V_{pd} and U_{eff} are hopping parameters depending on the manganese-anion distance and an electron-electron interaction parameter in the Hubbard fashion. E_v and E_{3d} are representative energies of the p -like valence-band edge states and the Mn $3d$ related valence-band states, respectively.

The p - d coupling parameter β strongly depends on the energy separation between the p -like and d -like valence-band states (see Equation 3-5). The modified positions (compared to bulk) of the p - and d -related bands in the band structure of the nanoparticle causes an increase of the p - d exchange interaction, resulting in a possible contribution to the enhanced band-gap bowing in the nanostructures (Figure 3-24). Due to the quantum confinement, the lowest valence-band state of the $\text{Cd}_{1-x}\text{Mn}_x\text{S}$ nanostructures may shift significantly towards the Mn $3d$ states, which are positioned

about 3 eV below the valence-band edge of bulk material. This enhancement effect is similar to that in bulk $\text{Cd}_{1-x}\text{Mn}_x\text{Y}$ with $\text{Y} = \text{Te, Se, S}$ where an increased p - d hybridization is observed with increasing band gap going from Te to S [142]. Similar results were also reported for the corresponding Zn-series where the main Mn 3d photoemission feature was found at 3.5, 3.6 and 3.8 eV below the valence-band maximum of (Zn,Mn)Te, (Zn,Mn)Se and (Zn,Mn)S, respectively [143].

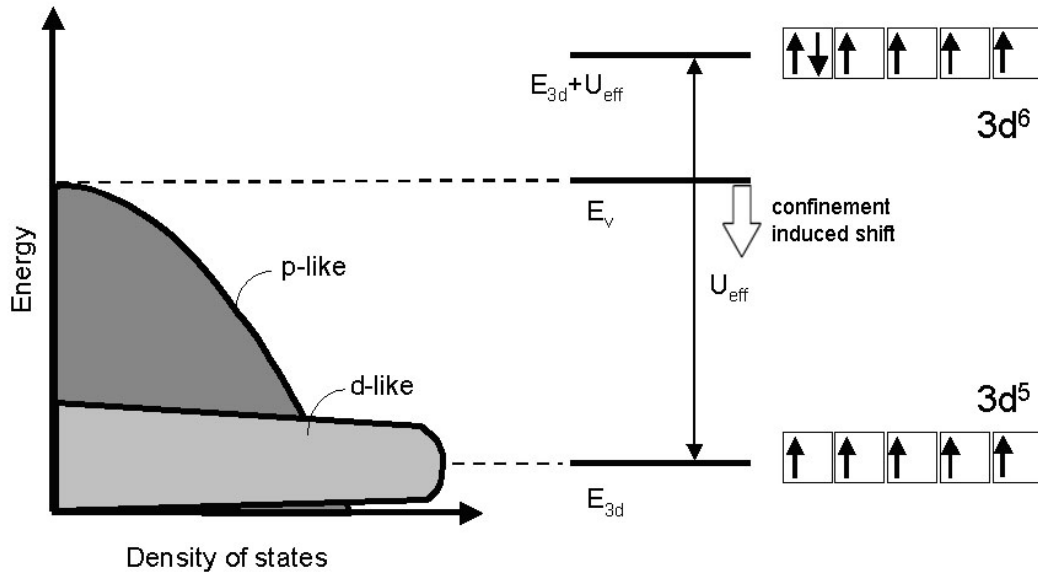


Figure 3-24: Schematic representation of the parameters contributing to the p - d exchange parameter β in the model by Larson et al. [141].

The susceptibility χ itself is also affected by the reduced dimensionality. In virtual crystal and mean-field approximation, the expression for χ is given by:

$$\chi = x_{\text{eff}} \frac{N_A S(S+1) g^2 \mu_B^2}{3k_B (T + \Theta(x))} \quad \text{Equation 3-6}$$

with S = spin of the 3d electrons, μ_B = Bohr magneton and Θ = Curie-Weiss parameter.

x_{eff} (which is an magnetically effective Mn concentration accounting for antiferromagnetic pairing) as well as $\Theta(x)$ are modified in a nanostructure due to the increase of the surface-to-volume ratio. The number of nearest neighbours on the cation

sublattice is reduced at the surface leading to an increase of the effective x . This also causes a reduction of the Curie-Weiss parameter Θ in a similar fashion (see also *Chapter 3.2.8*). The combination of both effects results in a stronger increase of χ with x in the nanostructures compared to bulk.

Therefore, both the dependence of the p - d exchange parameter β and that of the susceptibility χ on reduced dimensionality are in concordance with the observed enhancement of the band gap bowing in $\text{Cd}_{1-x}\text{Mn}_x\text{S}$ and $\text{Cd}_{1-x}\text{Mn}_x\text{Se}$ nanostructures as a function of x . It is worth mentioning here that the former effect is probably of less importance because a good description of the magnetic properties of the paramagnetic phase of the (II,Mn)VI nanostructures is obtained (see *Chapter 3.2.8*), assuming that the coupling between adjacent Mn-ions J_{mn} (which is proportional to β^2) is not altered in the nanostructures. However, the dependence of the band gap of bulk $\text{Zn}_{1-x}\text{Mn}_x\text{S}$ and the corresponding nanostructured samples on the Mn-concentration x seems to be an exception from a general rule. Although bulk (Zn,Mn)Te [136,144] as well as (Zn,Mn)Se [137,140] exhibit considerable bowing effects, neither the bulk $\text{Zn}_{1-x}\text{Mn}_x\text{S}$ [145] nor the nanostructured samples in *Figure 3-23* exhibit significant bowing effects with increasing x .

The signal of the band-to-band transition of the nanoparticles is only observed because of the efficient energy transfer from the band states into the internal $\text{Mn}^{2+} 3d^5$ shell (see above and also *Figure 2-5*). However, the mechanism of this energy transfer in wide band gap (II,Mn)VI semiconductors – although known for decades – is not at all understood [146-149]. As demonstrated, the Mn^{2+} ions are incorporated on cation sites of the II/VI hosts. The tetrahedral crystal field of the cation site shifts and splits the $3d$ states in energy compared to the free Mn^{2+} ion. The ^6S ground state of the free Mn^{2+} ion (which according to Hund's rule has all five electron spins aligned in parallel, giving rise to a total spin $S = 5/2$) is shifted down in energy by the crystal field and is referred to as $^6\text{A}_1$. The first excited quartet state ^4G of the free ion is split into four states which with increasing energy are labelled according to the irreducible representation of T_d symmetry by $^4\text{T}_1$, $^4\text{T}_2$, $^4\text{A}_1$ and ^4E (all having a total spin of $S = 3/2$). In wide-gap

(Cd,Mn) and (Zn,Mn) chalcogenide compounds the effective energy transfer is manifested by the broad yellow luminescence band due to the transition from the 4T_1 first excited state to the 6A_1 ground state of the $Mn^{2+} 3d^5$ shell. This transition occurs although the internal optical transitions within the $3d$ shell are in principle forbidden by parity and spin selection rules. Various mechanisms for a weakening of these selection rules have been discussed, which eventually lead to finite transition probabilities and finite lifetimes. The most likely mechanisms for the relaxation of the selection rules are the spin-orbit coupling, the p - d hybridization of the Mn $3d^5$ -states with the p -states of the surrounding anions and the lack of inversion symmetry [83,84]. For smallest Mn-concentrations and dominantly isolated Mn-ion centres the decay time of the $^4T_1 \rightarrow ^6A_1$ transition was found to be about 1.8 ms [150] and reduces into the μs range with increasing Mn-concentration, mainly caused by the so called "concentration quenching" [151,152]. At higher doping levels x the energy can be transported between different Mn-ion sites by a non-radiative resonant energy-transfer process [153].

It can be anticipated that the energy transfer from the band states (or excitonic states) into the Mn-internal transitions as well as the energy transfer within the Mn-subsystem will strongly depend on the dimensionality of the system. Quantum confinement of the excitons might increase the overlap of the excitonic wavefunction with the Mn-ions in the dot and thus make the energy transfer more efficient. On the other hand, the reduction of the dimensionality reduces the number of neighbouring Mn-ions at a given doping level x probably leading to a suppression of the concentration quenching. There are a few preliminary results along these lines in the literature, which have to be considered very cautiously as the non-radiative processes at the surface will also become more important as the dimensions are further reduced [89,91,154,155].

3.2.8. Magnetic properties of nanostructured DMS compounds

3.2.8.1. General discussion of the EPR data

The magnetism of atoms, molecules and solids is based on the coupling between the spin and the angular orbital momentum of the electrons. The different types of magnetism can be described as the different relative orientations of these magnetic momentums. By reducing the size of a solid the collective behaviour of all magnetic momentums ("macromagnetism") passes through a phase transition at the Curie-temperature (for ferro- and ferromagnetic compounds, T_C) or the Néel-temperature (for antiferromagnetic compounds, T_N) to an individual behaviour of single magnetic momentums ("nanomagnetism"). *Figure 3-25* gives a schematic representation of this process.

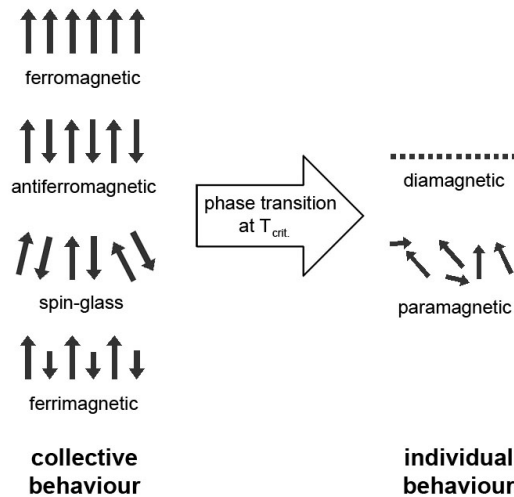


Figure 3-25: Schematic representation of the phase transition from macromagnetism to nanomagnetism.

At what size this phase transition takes place is dependent on the strength and scope of the magnetic interactions, as well as on the local symmetry. Diluted magnetic semiconductors are ideal model systems for the investigation of magnetic effects at reduced dimensions. They exhibit unusual magnetic properties, like the so-called giant Zeeman splitting and have rich magnetic phase diagrams. Besides, in the case of (II,Mn)VI semiconductors the manganese serves as a useful probe, because of its half filled 3d shell with its $S = 5/2$ spin and the internal transitions.

Undoped II-VI semiconductors ($x = 0$) are diamagnetic whereas Mn-VI compounds ($x = 1$) are paramagnetic at high temperatures and exhibit an antiferromagnetic phase at low temperatures. The degree of magnetic coupling between the spins of the Mn-ions depends strongly on the average distance between them, *i.e.* on x . Consequently, a very rich magnetic phase diagram as function of x and T arises for a typical (II,Mn)VI semiconductor compound such as (Cd,Mn)S (see *Figure 3-26*). Decreasing the concentration x of magnetic ions in diluted magnetic II-VI compounds restricts the spin ordering effects to the lower temperature region. Nevertheless, phases determined by collective magnetic behaviour such as antiferromagnetic (AF) phases as well as a spin-glass phase (SG) are commonly observed in addition to the paramagnetic phase (P). The P-phase extends to lower temperatures with decreasing x . For example, for (Cd,Mn)S, a (disordered) AF-phase which has a long-range spin ordering occurs below a critical temperature $T_N(x)$ for a sufficiently high Mn-concentration $x > 0.8$ (beyond the miscibility gap). The corresponding phase transition is characterised by peaks at T_N in both the magnetic susceptibility and the specific heat. For Mn-concentrations below the miscibility gap a SG-phase is observed for temperatures below $T_{SG}(x)$. In the case of (Cd,Mn)Te even a transition to the AF-phase has been reported for $x = 0.7$ [156], which means that it is still below the miscibility gap. The spin-glass phase is characterised by an antiferromagnetic short-range ordering of the spins, as well as by frustration effects. The somewhat diffuse phase transition from the paramagnetic into the spin-glass phase leads to a peak at $T_{SG}(x)$ in the temperature dependence of the magnetic susceptibility, but no anomaly in the specific heat is observable. Neutron-scattering experiments have shown that small antiferromagnetically ordered clusters already appear above T_{SG} , which grow in size with decreasing temperature. Another surprising fact is that a spin-glass phase is observable not only above the percolation limit ($x \approx 0.2$), but also below. In the very low concentration range, a rather long-range interaction is necessary, in addition to the short-range superexchange interaction, to yield a spin-glass phase. The spin freezing temperatures below the percolation concentration are very small, for example, between 0.1 K and 1 K for $x \approx 0.01$. The magnetic dipole-dipole interaction between more distant Mn^{2+} -ions is proposed to be the required long-range interaction

responsible for this spin-ordering mechanism, despite the fact that the dipole-dipole interaction might be too weak to cause the ordering at finite temperatures [157].

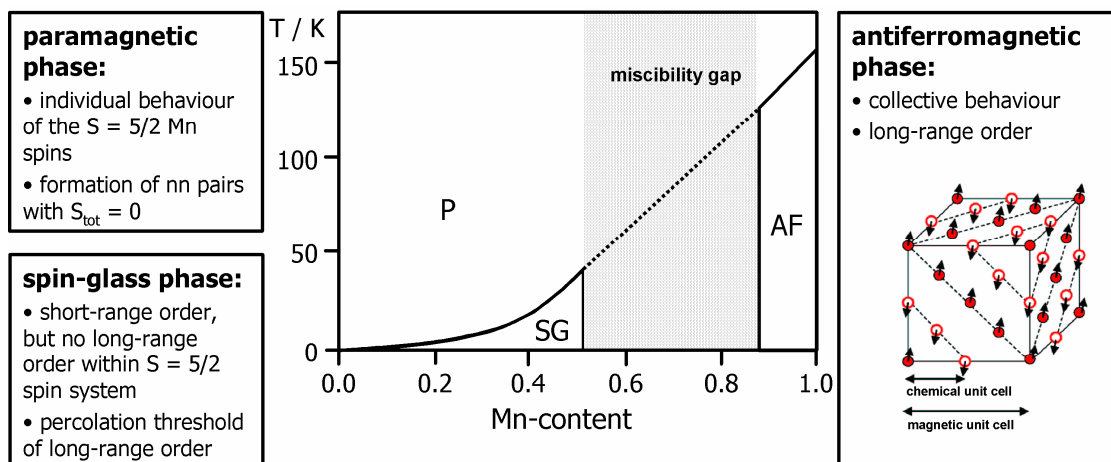


Figure 3-26: Schematic representation of a typical magnetic phase diagram of a (II,Mn)VI semiconductor.

As in bulk (II,Mn)VI materials, the integral EPR signal corresponding to the Mn^{2+} absorption has a Lorentzian lineshape in the paramagnetic regime [158]. The overall intensity I_{tot} as well as linewidth ΔH of the Lorentzian are very sensitive to the spin-spin correlations between the Mn^{2+} ions. Not only changes of the magnetic order with temperature, *e.g.* transitions from the paramagnetic phase to the spinglass phase or from the paramagnetic phase to the antiferromagnetic phase, are reflected by the temperature dependence of ΔH and I_{tot} , but also changes of the magnetic interactions within the paramagnetic phase itself due to a reduction of the lateral dimensions.

The EPR spectra for (II,Mn)VI nanoparticles synthesised either in reverse micelles or inside mesoporous hosts are very similar. As a typical example, the EPR spectra of $\text{Cd}_{1-x}\text{Mn}_x\text{S}$ and $\text{Zn}_{1-x}\text{Mn}_x\text{S}$ nanoparticles with x varying from 0.01 to 0.2 or 0.3, respectively, synthesised inside the 6 nm wide pores of SBA-15 silica are shown in Figure 3-27. All spectra were taken at 4 K and normalised to the same amplitude.

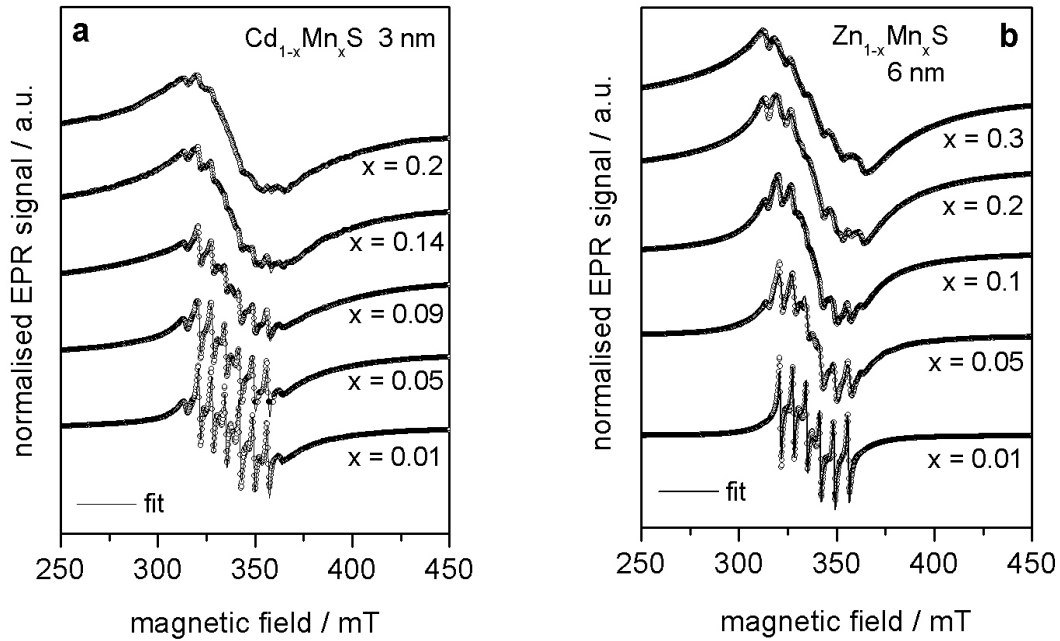


Figure 3-27: EPR spectra of (a) 3 nm $\text{Cd}_{1-x}\text{Mn}_x\text{S}$ and (b) 6 nm $\text{Zn}_{1-x}\text{Mn}_x\text{S}$ nanoparticles with x varying from 0.01 to 0.2 and 0.3, respectively at $T = 4$ K.

The EPR spectra are typical for exchange-coupled Mn^{2+} ions in (Cd,Mn) and (Zn,Mn) chalcogenide mixed crystals [159-161]. The features in the EPR spectra can be best explained in the spectrum of the $x = 0.01$ samples. This spectrum consists of a sextet of sharp lines with a splitting of about 7 mT between neighbouring lines, each line with a pair of satellites at lower magnetic on a broad background, which is well described by a Lorentzian line. The whole spectrum is centred around a g -factor of $g = 2.00(1)$ in the case of the Cd-sample and $g = 1.999$ in the case of the Zn-sample. The sharp lines and their satellites correspond to the “allowed” ($\Delta m_S = \pm 1$, $\Delta m_I = 0$) and the “forbidden” ($\Delta m_S = \pm 1$, $\Delta m_I = \pm 1$) hyperfine transitions of the six Zeeman-split $m_S = -5/2, \dots, +5/2$ levels (see also Figure 2-3) of the $^6\text{S}_{5/2}$ (or $^6\text{A}_1$) ground state of the Mn^{2+} 3d-electrons. The hyperfine structure arises from the interaction between the $S = 5/2$ spin of the unpaired 3d-electrons with the $I = 5/2$ spin of the ^{55}Mn nucleus. The hyperfine splitting characteristic for Mn^{2+} in ZnS amounts about $\delta\mathcal{B}_{\text{HFS}} = 7.0$ mT between neighbouring allowed transitions in zincblende as well as in wurtzite structure [162]. The splitting observed in the spectrum of the sample with 1% Mn agrees well with this value. The $\Delta m_S = \pm 1$ transition energies between the Zeeman levels $m_S = \pm 5/2$

and $m_S = \pm 3/2$ as well as $m_S = \pm 3/2$ and $m_S = \pm 1/2$ vary with changing crystal orientation in the range of about 2 mT with respect to the $m_S = -1/2$ to $m_S = +1/2$ transitions [159]. Therefore, the corresponding sextets of lines cannot be distinguished in the spectrum of powdered samples, but their averaging determines the width of the six resonance lines. The spectrum of $x = 0.01$ is typical for Mn^{2+} ions in the tetrahedral environment of a zincblende crystal [159,163]. Thus, the crystal structure of the nanoparticles with $x = 0.01$ is zincblende, which is often found for (II,Mn)VI nanoclusters containing only little manganese [159].

With increasing Mn content the dipolar interaction and exchange coupling merge the hyperfine structure into one broad resonance line due to the increasing superexchange interaction between the Mn^{2+} ions [158,164]. This is documented best for $x = 0.3$, but this broad line can already be identified for $x = 0.01$. The spectrum for $x = 0.01$ is satisfactorily described by the sum of the broad line and the hyperfine structure of six lines. Both the broad line and the hyperfine lines were assumed to be of Lorentzian shape. With increasing x the broad background line strongly increases and the “forbidden” hyperfine transitions become more prominent for $x \geq 0.1$. These are typical features of Mn^{2+} on a Cd- or Zn-site in a wurtzite crystal [158,161], which is also tetrahedrally coordinated, but with a strong tetragonal distortion. Such a tetragonal distortion gives rise to a much stronger crystal-field splitting of the Mn^{2+} ground state compared to that in a zincblende structure. Due to the stronger crystal field the orientation dependent EPR spectrum in wurtzite extends over a field range of about 150 mT [159]. In the powder average this yields a resonance line, approximately 30 mT broad. Besides the hyperfine structure described above, a second hyperfine structure with a larger splitting of about 9 mT can be distinguished and gains weight with respect to the first one at higher Mn concentrations. This feature is assigned to Mn loosely aggregated at the surface of the nanostructure (It should not be confused with Mn incorporated into the crystal lattice in the vicinity of the surface).

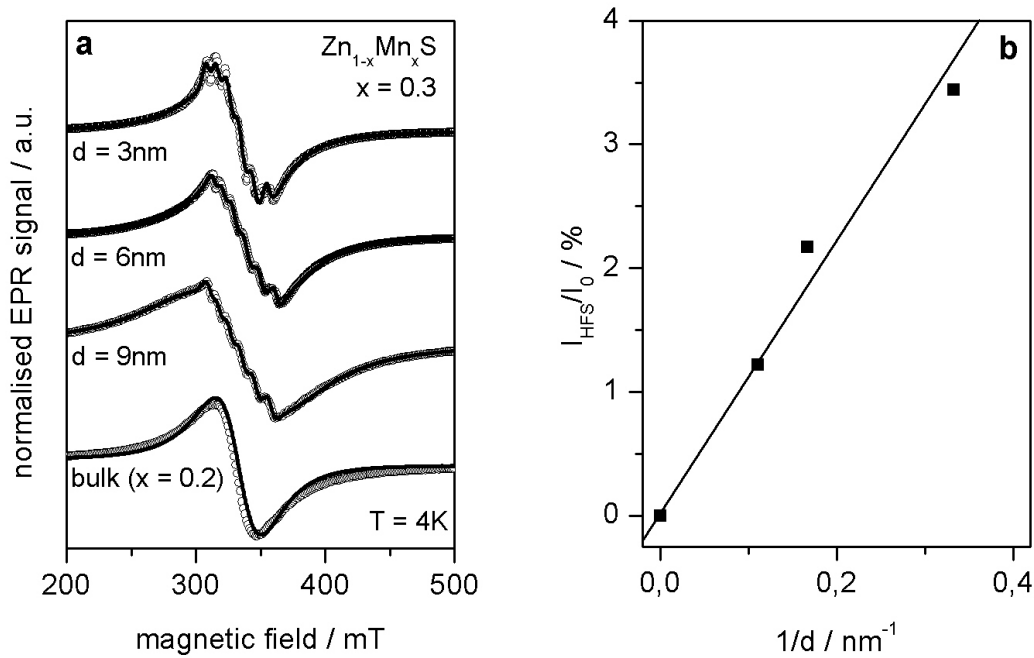


Figure 3-28: (a) Normalised EPR spectra of bulk $\text{Zn}_{0.8}\text{Mn}_{0.2}\text{S}$ and nanostructured $\text{Zn}_{0.7}\text{Mn}_{0.3}\text{S}$ in MCM-41 silica ($d = 3\text{ nm}$), SBA-15 silica ($d = 6\text{ nm}$), SBA-15 silica ($d = 9\text{ nm}$); (b) Plot of intensity ratio I_{HFS}/I_0 between hyperfine structure and full spectrum as a function of the inverse pore diameter $1/d$.

To clarify this, the spectra of $\text{Zn}_{0.7}\text{Mn}_{0.3}\text{S}$ nanostructures with different pore sizes were compared, as shown in Figure 3-28 a. All spectra were taken at 4 K, where the hyperfine structure can be best identified in the nanostructures, because with increasing temperature it becomes more and more smeared out. In the bulk sample $\text{Zn}_{0.8}\text{Mn}_{0.2}\text{S}$, which was used for comparison, no hyperfine structure was visible at all. The spectra were again fitted by the sum of one broad Lorentz curve and a hyperfine structure of six Lorentz curves. All spectra can be satisfactorily described in this way. The intensity, which is proportional to the spin susceptibility and hence to the number of spins, corresponds to the area below the absorption curve. It is given by the two-fold field integration of the EPR signal, which itself represents the field derivative of the absorption. The fit allows to separate the intensity of the hyperfine structure I_{HFS} from the intensity of the full spectrum I_0 and hence to determine the relative number of Mn^{2+} -ions, which give rise to the hyperfine structure. Figure 3-28 b exhibits a linear dependence of the intensity ratio I_{HFS}/I_0 on the inverse pore diameter $1/d$. This corroborates the assumption that the hyperfine structure arises from manganese spins on

the surface of the nanoparticles instead of interstitial positions, because the surface-to-volume ratio also varies with $1/d$. For the bulk sample this is by far smaller than for the nanoparticles and therefore the hyperfine structure vanishes. The absolute value of the intensity ratio is only about 20 % of the value, which one would expect for the full surface layer of approximately 0.3 nm thickness, *i.e.* only 20 % of the Mn ions at the surface are bound weakly enough to give rise to the hyperfine structure. From the EPR results we can deduce that the majority of the Mn^{2+} ions is well incorporated into the nanostructures and only a small amount remains weakly bound at their surface. This amount of aggregated Mn-ions at the surface of the nanoclusters corresponds to less than 4 %, 2 % and 1 % of the total Mn-content for the 3 nm, 6 nm and 9 nm nanoparticles, respectively.

3.2.8.2. Analysis of the Curie-Weiss parameter Θ

The Curie-Weiss parameter Θ of the paramagnetic phase is a measure for the type and strength of the interaction between the manganese ions. It can be obtained experimentally either from plots of the inverse EPR intensity I_{tot}^{-1} versus temperature T or from plots of the inverse susceptibility χ^{-1} versus temperature determined by SQUID measurements. It is found that the experimentally determined Curie-Weiss parameter is usually well described using *Equation 3-7* [165,166].

$$\Theta(x) = -\frac{2}{3k_B} S(S+1)x \left[J_{nn} z_{nn}^b + J_{nnn} z_{nnn}^b \right] \quad \text{Equation 3-7}$$

J_{nn} and J_{nnn} are the exchange parameters, z_{nn}^b and z_{nnn}^b are the number of next neighbours and next-nearest neighbours on the cation lattice, respectively. For both wurtzite and zincblende crystals z_{nn}^b and z_{nnn}^b are 12 and 6 respectively, in the bulk.

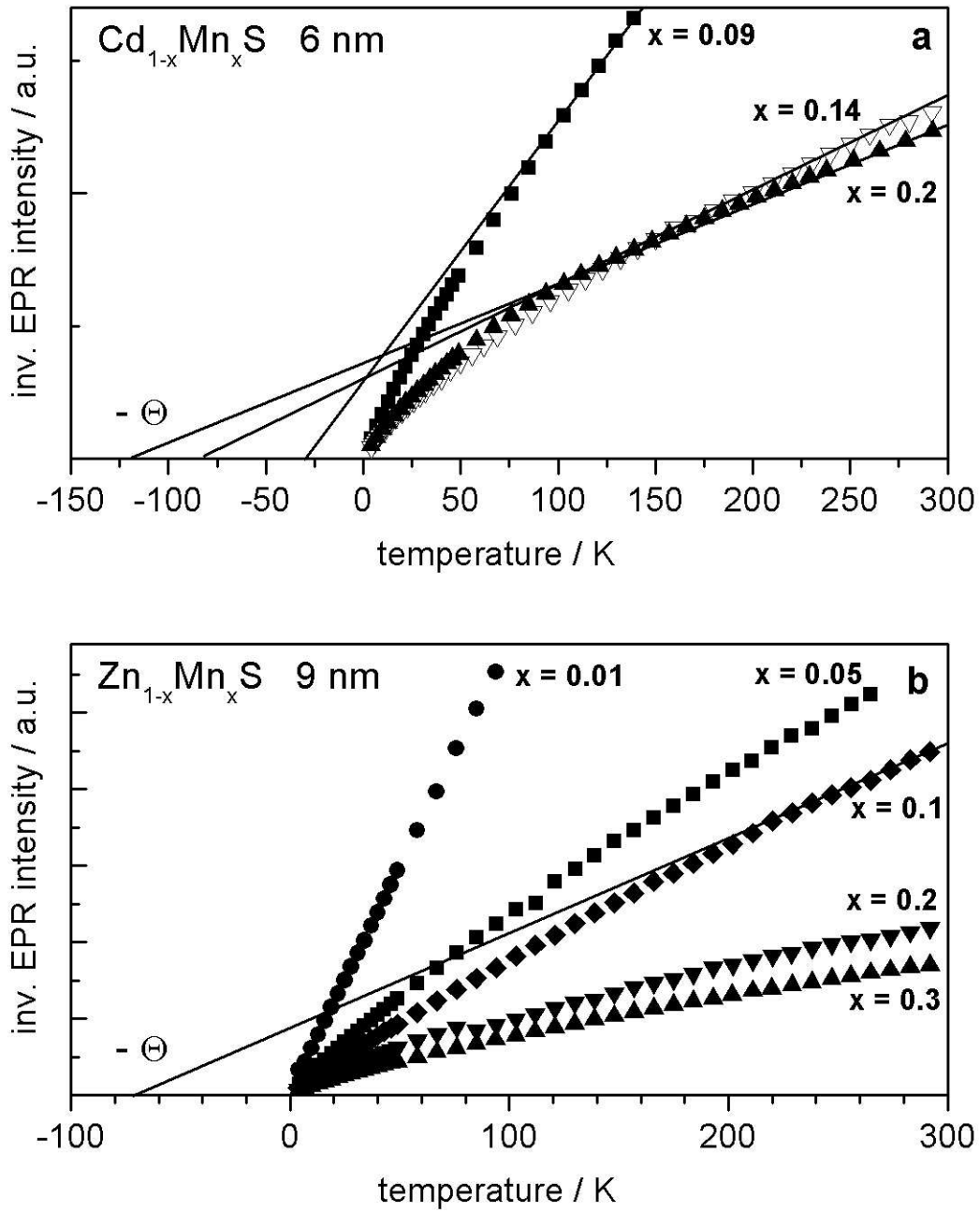


Figure 3-29: Temperature dependence of the inverse EPR intensity I_{tot}^{-1} of (a) 6 nm $\text{Cd}_{1-x}\text{Mn}_x\text{S}$ nanoparticles and (b) 9 nm $\text{Zn}_{1-x}\text{Mn}_x\text{S}$ nanoparticles.

Figure 3-29 shows exemplarily plots of the inverse EPR intensity I_{tot}^{-1} of 6 nm $\text{Cd}_{1-x}\text{Mn}_x\text{S}$ nanoparticles with x ranging from 0.09 to 0.2 (a) and of 9 nm $\text{Zn}_{1-x}\text{Mn}_x\text{S}$ nanoparticles with x ranging from 0.01 to 0.3 (b) as a function of the temperature. Similar results were also obtained for all other nanostructured samples. As in the case of bulk (II,Mn)VI, the slope of the $I_{tot}^{-1}(T)$ curve decreases with increasing doping level x

and, at low temperatures, deviates from the Curie-Weiss behaviour giving the curves a somewhat negative curvature. At first sight surprisingly, the $\text{Zn}_{1-x}\text{Mn}_x\text{S}$ particles with $x \geq 0.2$ do not show any indication for a phase transition into a spin-glass phase, in contrast to bulk material [167]. This result will be discussed further, when the EPR linewidth is analysed. Fitting the $I_{\text{tot}}^{-1}(T)$ plots in the high temperature regime (150 K to 300 K) following the Curie-Weiss dependence

$$I_{\text{tot}}^{-1}(T) \sim \chi^I(T) \sim (T + \Theta) \quad \text{Equation 3-8}$$

yields the Curie-Weiss parameter Θ as a function of x .

The corresponding plots for various particle diameters D (obtained by analysing the corresponding EPR data) are shown in *Figure 3-31* and show some clear trends. As expected, $|\Theta|$ increases with increasing x in each series. The $|\Theta|$ -values obtained for the nanostructures are considerably lower than those found in corresponding bulk (II,Mn)VI samples. These are represented by the solid lines in *Figure 3-31* and are calculated using *Equation 3-7*. The exchange parameters are taken from the literature [166,168]. Moreover, in the figure, it appears that the $|\Theta|$ -values show a tendency to decrease with decreasing particle diameter d at constant x . Both effects are due to the reduced lateral dimensions of the nanostructures. They occur because Mn-ions on the surface of the (II,Mn)VI nanostructures incorporated inside the mesoporous SiO_2 matrices have reduced numbers of nearest neighbours $z_{nn}^s \approx z_{nn}^b/2$ and next-nearest neighbours $z_{nnn}^s \approx z_{nnn}^b/2$ compared to the bulk of the material. This becomes significant as the surface-to-volume ratio is strongly increased in the nanostructures. *Figure 3-30* shows a schematic drawing of this effect.

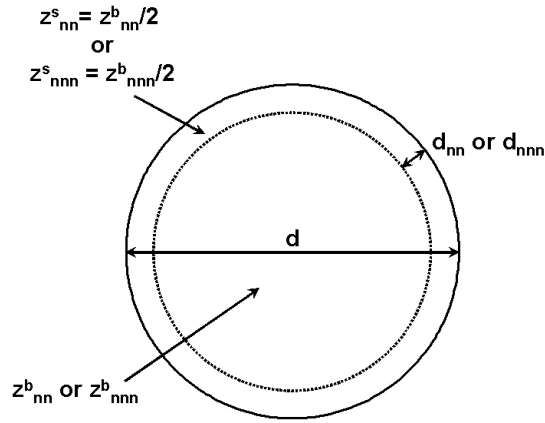


Figure 3-30: Schematic drawing of the reduced number of next neighbours (z_{nn}) and next-nearest neighbours (z_{nnn}) at the surface (s) and in the bulk-like (b) volume of a nanoparticle.

The effect can be estimated by dividing the volume V of the nanostructure into a volume V^s close to the surface (where the exchange effects differ from bulk) and a remaining bulk-like volume $V^b = V - V^s$. The choice of the two volumes will differ for nearest neighbours and next-nearest neighbours because the length scales involved, *i.e.* the nearest neighbour distance d_{nn} and the next-nearest neighbour distance d_{nnn} , are different. In the following the wurtzite structure is approximated by a zincblende structure for simplicity. This is a good approximation here as only nearest and next-nearest neighbours are considered. It holds $d_{nn} = (1/2)^{0.5}a$ and $d_{nnn} = a$ where a is the lattice constant of the zincblende lattice. It is $a \approx 0.55$ nm for (Zn,Mn)S and $a \approx 0.58$ nm for (Cd,Mn)S [126]. These values of the lattice constant were used for $\text{Cd}_{1-x}\text{Mn}_x\text{S}$ and $\text{Zn}_{1-x}\text{Mn}_x\text{S}$ independent of x in the following because its dependence on x is not known for the zincblende modification. Two limiting cases for the shape of the nanostructure shall be considered:

- (i) an ideal wire structure of infinite length and diameter d and
- (ii) a spherical nanoparticle with diameter d where d is the pore diameter of the SiO_2 host matrix.

The following definitions are obtained:

$$V_{nn}^s = V \left(1 - \left(\frac{d - 2d_{nn}}{d} \right)^\delta \right) \quad V_{nnn}^s = V \left(1 - \left(\frac{d - 2d_{nnn}}{d} \right)^\delta \right) \quad \text{Equation 3-9}$$

with $\delta = 2$ for infinite wires and $\delta = 3$ for spheres. In both cases it holds that $V_{nn}^b = V - V_{nn}^s$ and $V_{nnn}^b = V - V_{nnn}^s$.

Rewriting *Equation 3-7* including surface effects yields [134]:

$$\Theta(x, d) = -\frac{2S(S+1)x}{3Vk_B} \left[J_{nn} (V_{nn}^b z_{nn}^b + V_{nn}^s z_{nn}^s) + J_{nnn} (V_{nnn}^b z_{nnn}^b + V_{nnn}^s z_{nnn}^s) \right] \quad \text{Equation 3-10}$$

Using *Equations 3-7* and *3-10* the Curie-Weiss parameters have been calculated for $\text{Cd}_{1-x}\text{Mn}_x\text{S}$ and $\text{Zn}_{1-x}\text{Mn}_x\text{S}$ nanostructures assuming a wire-like and a spherical shape. The results of the calculation are also plotted in *Figure 3-31*. In both graphs, the dotted and dashed lines represent the results for a wire-like and a spherical shape, respectively. In the right graph, there are three calculated Θ -curves for wire-shaped and three calculated Θ -curves for sphere-shaped nanoparticles. In both series the curves are assigned as follows to the corresponding d -values. The steepest curve corresponds to $d = 9$ nm, the intermediate curve to $d = 6$ nm and the least steep curve to $d = 3$ nm. Comparing experimental data and theoretical curves indicates that the theoretically derived reduction of the Curie-Weiss parameter Θ due to surface effects are, as expected, larger for spherical nanoparticles compared to wire-shaped nanoparticles. The calculated reductions are of the right magnitude, but still smaller than those found in the experiment. Assuming spherical particles yields a better but yet not perfect agreement, which is in concordance with the TEM analysis of the (II,Mn)VI nanostructures (see *Figure 3-10 b* and *f*). It can be concluded, that the particles are of elongated spherical or ellipsoidal shape.

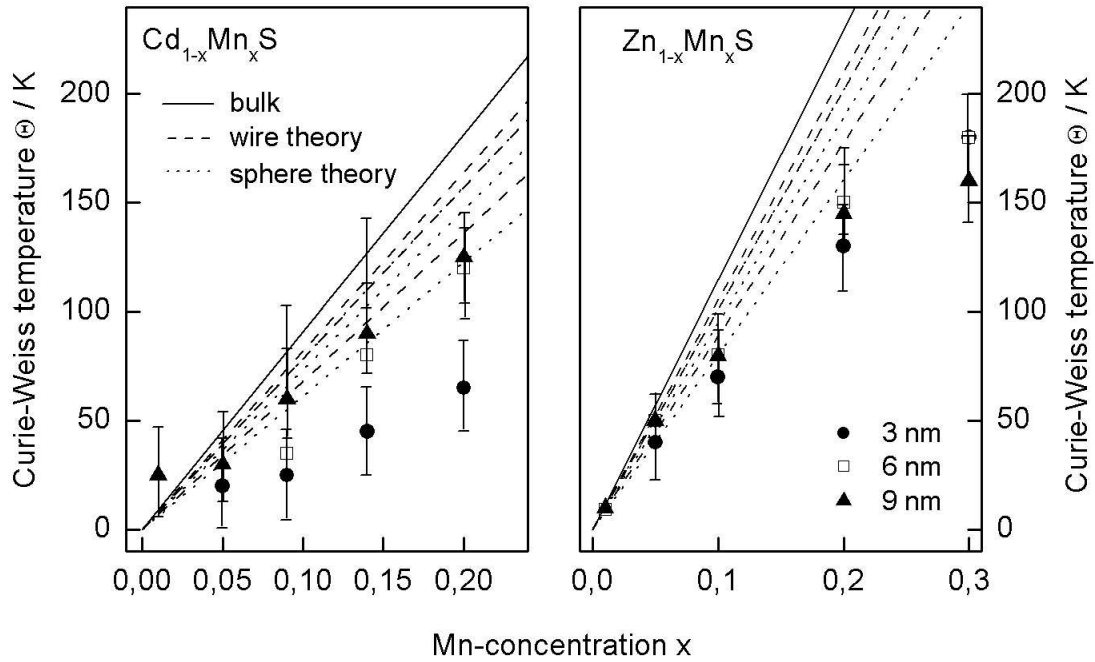


Figure 3-31: Plots of the Curie-Weiss temperature $|\Theta|$ versus Mn-content x obtained by analysing the EPR data of 3, 6 and 9 nm $\text{Cd}_{1-x}\text{Mn}_x\text{S}$ nanoparticles (left) and $\text{Zn}_{1-x}\text{Mn}_x\text{S}$ nanoparticles (right). The solid line is calculated using Equation 3-7, the dashed and dotted lines are calculated using Equation 3-10.

3.2.8.3. Analysis of the EPR linewidth

In paramagnetic systems such as the (II,Mn)VI semiconductors, the EPR linewidth behaviour depends intimately on the physics of the inter-manganese spin-spin interactions. The EPR linewidth of bulk (Cd,Mn)- and (Zn,Mn)-chalcogenides has been widely studied [158,169-172]. The experimental results give a consistent picture, which can be summarized as follows:

- (i) In general, the EPR linewidth is found to increase with increasing Mn-content and with decreasing temperature. The EPR lineshape is Lorentzian for all samples in the paramagnetic regime.
- (ii) The EPR linewidth depends very strongly on the anion, *i.e.* Te, Se and S. For comparable Mn-contents x and temperature T , it is found that the EPR line becomes broader as the atomic number of the anion increases from S via Se to Te [158,169].

(iii) There is a much weaker dependence on the type of non-magnetic cation. The EPR line broadens as the atomic number of the cation decreases, *e.g.* $\text{Zn}_{1-x}\text{Mn}_x\text{S}$ signals are somewhat weaker and broader than $\text{Cd}_{1-x}\text{Mn}_x\text{S}$ signals for the same x and T [169].

As a further complication in (II,Mn)VI semiconductors with a high doping level x , the EPR linewidth is found to diverge at low temperatures T due the magnetic phase transition from the paramagnetic phase to the spin-glass phase, in particular for $x > 0.2$, *i.e.* above the percolation threshold in three dimensions. This additional broadening of the EPR linewidth occurs due to the divergence of the spin-spin correlation length in the vicinity of the paramagnetic to spin-glass phase transition. It is accompanied by a change of the EPR lineshape which becomes asymmetric.

The divergence of the EPR linewidth is often accounted for empirically by adding a contribution ΔH_{sg} of the form [172]:

$$\Delta H_{sg} = \frac{C}{(T - T_{sg})^\nu} \quad \text{Equation 3-11}$$

where T_{sg} is the spin-glass transition temperature, C is a constant and ν is a critical exponent. As already indicated in the discussion of the magnetic susceptibility data, none of the $\text{Zn}_{1-x}\text{Mn}_x\text{S}$ and $\text{Cd}_{1-x}\text{Mn}_x\text{S}$ nanoparticle samples with $x \leq 0.3$ show signs of the paramagnetic to spin-glass transition. This is further corroborated by the corresponding EPR linewidths data in *Figure 3-32* where the linewidth remains finite even at the lowest temperature. The critical Mn-concentration x , above which the phase transition occurs, corresponds to the percolation threshold for the Mn-ions on the cation sublattice. Obviously, the percolation threshold is increased due to the reduction of the lateral dimensions of the nanostructures and, thus, the magnetic phase transition is suppressed. Therefore, the linewidth behaviour in the nanoparticles is solely determined by the spin-spin interactions within the paramagnetic Mn-subsystem.

Based on spin-spin interactions, Samarth and Furdyna explained qualitatively the experimental findings for the EPR linewidth in bulk paramagnetic (II,Mn)VI

semiconductors in the high temperature regime (*i.e.* $T \gg T_{sg}$) [158]. Their explanations were confirmed on a more quantitative basis by theoretical calculations of Larson and Ehrenreich [173]. At high temperatures, the isotropic exchange interaction, in the sense of motional narrowing, suppresses the broadening of the EPR-line due to the anisotropic interactions, dipolar and a contribution due to anisotropic exchange. At low temperatures, the nearest neighbour Mn-ions form antiferromagnetic pairs with $S_{tot} = 0$ due to the isotropic exchange interaction and thus are no longer magnetically active. Therefore, the linewidth narrowing due to the interplay of dipolar interaction and exchange interaction is reduced. This explains the general temperature dependence of the EPR linewidth.

The dependence on Mn-concentration is explained in the same fashion: The linewidth increases with increasing x at low temperatures because the anisotropic interactions become stronger as the mean distance between Mn-ions is reduced. The observed dependence on the type of group II cation can be explained as well along these lines. Broadening effects for (Zn,Mn)-chalcogenides are bigger than for corresponding (Cd,Mn)-chalcogenides as the lattice constants are smaller for the Zn-based compounds. The observed dependence of the linewidth on the anion is at first sight counter-intuitive as the linewidth decreases (*i.e.* the interactions become weaker) with decreasing anion size. The reason is that different anisotropic spin-spin interactions contribute to the linewidth and their relative importance changes with the anion type.

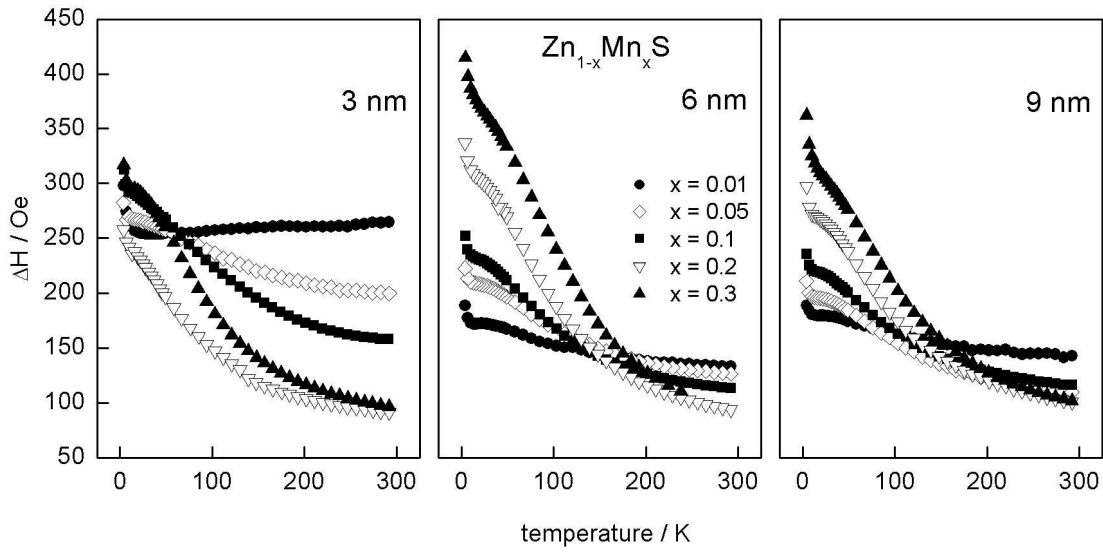


Figure 3-32: Plots of the EPR linewidth ΔH versus temperature for $\text{Zn}_{1-x}\text{Mn}_x\text{S}$ nanoparticles of different doping levels x and diameters of 3 nm (left), 6 nm (middle) and 9 nm (right).

Figure 3-32 depicts plots of the EPR linewidth ΔH versus temperature for various $\text{Zn}_{1-x}\text{Mn}_x\text{S}$ nanoparticle samples with different doping levels x and diameters. The temperature trends of ΔH for these samples can be explained qualitatively in the same fashion as for bulk $(\text{II},\text{Mn})\text{VI}$. At low temperatures, when nearest-neighbour Mn-ions have dimerised to antiferromagnetic pairs, dipolar broadening dominates for the remaining unpaired Mn-spins. With increasing temperature, an exchange-narrowing effect is observed due to the nearest-neighbour exchange at temperatures, when the thermal energy is sufficient to break up antiferromagnetically coupled nearest-neighbour pairs.

In the following, the concentration dependence of the linewidth at low temperatures ($T = 30$ K) and at high temperatures ($T = 290$ K) will be analysed in more detail. Figure 3-33 shows plots of the linewidth at these temperatures for $\text{Cd}_{1-x}\text{Mn}_x\text{S}$ and $\text{Zn}_{1-x}\text{Mn}_x\text{S}$ nanoparticles with different diameters. It can be seen from the left graph of the figure that, at $T = 30$ K, the linewidth depends almost linearly on x . This can be understood as follows. At these temperatures the broadening is determined by a dipolar contribution in addition to an almost constant hyperfine contribution H_{HF} . Exchange narrowing effects

due to nearest-neighbour exchange J_{nn} are negligible as basically all Mn-ions with manganese nearest neighbours have formed antiferromagnetic pairs.

The linewidth at low temperature can be described as:

$$\Delta H = H_{HF} + H_{dip} \approx H_{HF} + C_{dip} \cdot x \quad \text{Equation 3-18}$$

where H_{dip} is the dipolar field at the site of a Mn-ion in mean-field approximation and C_{dip} is a proportionality factor used as fitting parameter [174].

Dipolar effects seem to be smaller for the 3 nm nanostructures. Moreover an additional constant broadening effect whose origin is unclear at present, occurs in these very small nanostructures. Nevertheless, the fits in the left graph of *Figure 3-33* show that the low temperature approximation in *Equation 3-18* well describes the observed linewidth behaviour in the nanoparticles, in particular for the 6 nm and 9 nm samples of both series. For the (Zn,Mn)S system, the value of H_{HF} of about 150 Oe determined for the 6 nm and 9 nm samples corresponds to half the extension of the six fine structure satellites in *Figure 3-27*. The value for the 3 nm samples is slightly larger. The linewidths of the $\text{Cd}_{1-x}\text{Mn}_x\text{S}$ nanoparticles show a similar dependence as the corresponding Zn-based series, but the linewidth is always smaller. It is worth pointing out that, as in bulk material, this simply reflects the difference in the cation size.

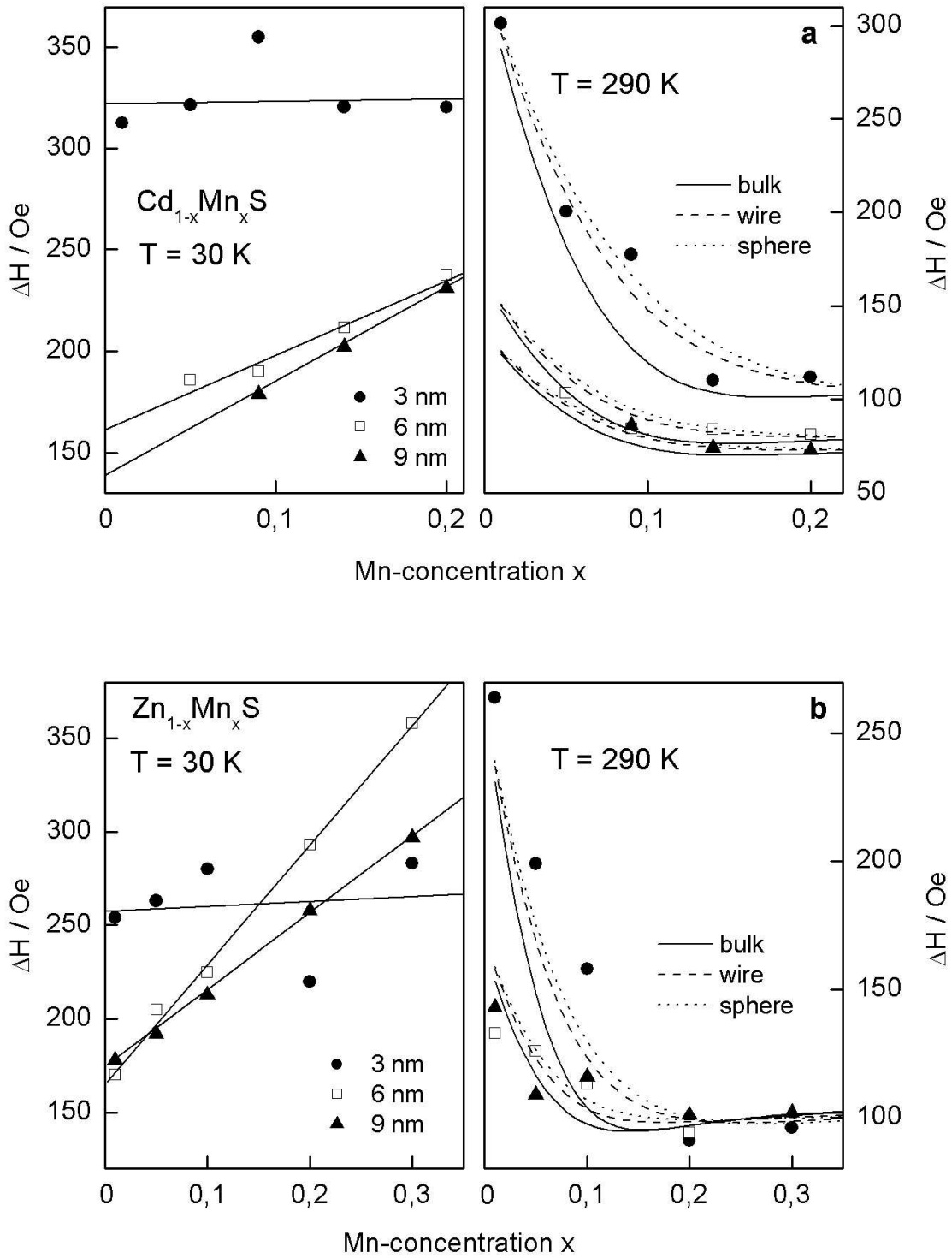


Figure 3-33: (a) Left: Plots of the EPR linewidth ΔH as a function of the doping level x at $T = 30\text{ K}$ for $\text{Cd}_{1-x}\text{Mn}_x\text{S}$ nanoparticles with different diameters. The solid lines are linear fits. Right: Plots of the EPR linewidth ΔH as a function of the doping level x at $T = 290\text{ K}$ for $\text{Zn}_{1-x}\text{Mn}_x\text{S}$ nanoparticles with different diameter. The lines depict the results of model calculations described in the text. (b) corresponding graphs for $\text{Zn}_{1-x}\text{Mn}_x\text{S}$ nanoparticles with different diameters.

The high temperature behaviour can be explained semi-quantitatively by considering the effect of the nearest-neighbour interaction J_{nn} , which determines the linewidth behaviour at temperatures, where the Mn nearest-neighbour pairs are broken up. For this purpose, the Mn-ions in the nanostructure can be divided up into two classes:

- (i) isolated (*is*) Mn-ions without Mn nearest neighbours (*nn*) and
- (ii) Mn-ions with one or more nearest neighbours.

Furthermore, as in the case of the discussion of the Curie-Weiss parameter $|\Theta|$, the volume of the nanostructure will be divided into a volume close to the surface V_{nn}^s and a bulk-like volume V_{nn}^b (see *Equation 3-9*) and the discussion will again be based on a zincblende lattice for simplicity.

The probabilities for the occurrence of the two classes of Mn-ions as a function of x at the surface and in the bulk of the nanostructure are given by:

$$\begin{aligned} p_{is}^b &= (1-x)^{z_{nn}^b} & p_{nn}^b &= 1 - p_{is}^b \\ p_{is}^s &= (1-x)^{z_{nn}^s} & p_{nn}^s &= 1 - p_{is}^s \end{aligned} \quad \text{Equation 3-19}$$

where $z_{nn}^b = 12$ is the number of nearest neighbours on the cation lattice in the bulk of a zincblende or a wurtzite lattice and $z_{nn}^s \approx z_{nn}^b/2$.

It is assumed that in both volumes the linewidth contribution ΔH_{is} of the isolated Mn ions is well described by fits of the low temperature linewidth data according to *Equation 3-18*. The linewidth contribution of the Mn ions with nearest neighbours is calculated in the same fashion as in *Reference 175*, but extended to account for additional broadening effects due to anisotropic exchange. In both regions it holds:

$$\Delta H_{nn} = \frac{\frac{10}{3} H_{dip,nn}^2 + H_{HF}^2 + (H_{ex,nn}^a)^2}{H_{ex,nn}^i} \quad \text{Equation 3-20}$$

where $H_{dip,nn}$ is the mean dipolar field for a Mn-ion with at least one Mn nearest neighbour. For the bulk-like volume, it is defined as:

$$(H_{dip,nn}^b)^2 \approx \frac{3}{4} S(S+1) \mu_0^2 \mu_B^2 g^2 \left[\frac{1}{d_{nn}^6} + x^2 \left(\frac{z_{nn}^b - 1}{d_{nn}^6} + \frac{z_{nnn}^b}{d_{nnn}^6} + \frac{z_{nnnn}^b}{d_{nnnn}^6} \right) \right] \quad \text{Equation 3-21}$$

where only the nearest neighbours ($z_{nn}^b = 12$, $d_{nn} = (1/2)^{0.5}a$), next-nearest neighbours ($z_{nnn}^b = 6$, $d_{nnn} = a$), and next next-nearest neighbours ($z_{nnnn}^b = 24$, $d_{nnnn} = (3/2)^{0.5}a$) are taken into account. In the surface region $(H_{dip,nn}^s)^2$ is obtained by replacing the bulk neighbour numbers z^b of each shell by the corresponding value z^s for the surface region. For simplicity, all the neighbour-numbers z^s are set to half the bulk value. H_{HF} is the constant value for the hyperfine and crystal-field broadening determined at low temperatures for each series, and $H_{ex,nn}^a$ and $H_{ex,nn}^i$ are the anisotropic and isotropic nearest-neighbor exchange fields. The latter is calculated according to Anderson and Weiss [175]:

$$H_{ex,nn}^i = 2.83 \frac{J_{nn}}{g\mu_B} \sqrt{S(S+1)} \quad \text{Equation 3-22}$$

Using $|J_{nn}| = 10.6$ K for (Cd,Mn)S and $|J_{nn}| = 16.1$ K for (Zn,Mn)S yields an isotropic nearest-neighbour exchange-field of about 60000 Oe, or 90000 Oe, respectively. The total linewidth as a function of x and diameter d is calculated according to:

$$\Delta H(x, d) = V^b \sqrt{(\Delta H_{is}^b p_{is}^b)^2 + (\Delta H_{nn}^b p_{nn}^b)^2} + V^s \sqrt{(\Delta H_{is}^s p_{is}^s)^2 + (\Delta H_{nn}^s p_{nn}^s)^2} \quad \text{Equation 3-23}$$

For both (II,Mn)VI systems, H_{nn}^a is the only free parameter in the calculation. Its value is determined by the linewidth limit at high x in the right graphs of *Figure 3-33*. It is assumed that in both volumes the linewidth contribution ΔH_{is} of the isolated manganese ions is well described by fits of the low temperature linewidth data according to *Equation 3-18*.

The calculations were carried out for all nanoparticles. In each case, they were performed for bulk as well as for spherical and wire-like nanostructures. Constant values for the anisotropic exchange field ΔH_{nn}^a were used throughout for both materials.

In the case of the Zn-based nanostructures, the best agreement was obtained for $\Delta H_{nn}^a = 3000$ Oe, while, for the Cd-based series, the best agreement was obtained for smaller values assuming 2500, 2200, and 2100 Oe for the 3, 6, and 9 nm series, respectively. This suggests that the anisotropic nearest-neighbour exchange-field might increase slightly with decreasing diameter for these nanostructures. For both materials, the value is about one order of magnitude larger than the corresponding dipolar field $\Delta H_{\text{dip},nn}^b$ for $x = 0.3$ and in reasonable agreement with the theoretical findings of Larson and Ehrenreich [173].

The theoretical curves for $\text{Cd}_{1-x}\text{Mn}_x\text{S}$ nanoparticles as well as for $\text{Zn}_{1-x}\text{Mn}_x\text{S}$ nanoparticles are also plotted in the right graphs of *Figure 3-33*. It can be seen that in all three cases the agreement between theory and experiment is best when a spherical shape of the magnetic nanoparticles is assumed. In particular, the linewidth decrease with increasing x is too rapid when a bulk-like situation is considered. The corresponding slope is reduced by surface effects as the probability for Mn-ions with manganese nearest neighbours is much lower in the surface region V_{nn}^s than in the bulk-like volume V_{nn}^b for $0 < x < 0.2$.

In conclusion, changes of the macroscopic observables, *e.g.* the Curie-Weiss parameter $|\Theta|$ and the EPR linewidth ΔH of the paramagnetic phase of (II,Mn)VI nanoparticles with sizes below 10 nm due to reduced dimensions are observable. It appears that the microscopic coupling between the Mn-ions (*e.g.* the nearest neighbour and next-nearest neighbour exchange-constants J_{nn} and J_{nnn}) is not altered to a first approximation. The macroscopic modifications arise mainly due to geometrical restrictions, *i.e.* the number of neighbours in the various shells around a manganese ion in the surface region are considerably reduced compared to a manganese ion in the bulk

of the structure. This effect becomes increasingly important with decreasing lateral dimensions of the nanostructure.

3.2.9. Magnetic properties of nanostructured binary MnS

Apart from the careful investigation of the manganese doped II/VI semiconductors, described in the previous chapters, the pure binary compound MnS was incorporated into different mesoporous host structures as well^a.

Bulk samples of zincblende MnS and MnSe (α -modifications) are known to be antiferromagnets of the *ccp* type III with Néel-temperatures of 100 K and 70 K, respectively. Even the stable rocksalt modification exhibits antiferromagnetism with Néel-temperatures of about 150 K. EPR measurements can be used to study the magnetic phase transitions of nanoparticles. The method is based on the divergence of the Mn^{2+} EPR linewidth due to the corresponding decrease in the spin-spin relaxation time [176-179], which is correlated with the divergence of the correlation length. The temperature dependence of the critical part of the linewidth can be written as

$$\Delta H \propto \frac{C}{(T - T_N)^\nu} \quad \text{Equation 3-24}$$

where ν is a critical exponent. This expression is somewhat similar to *Equation 3-11* for the paramagnetic to spin-glass transition. In the bulk samples, as expected, the linewidth ΔH of the EPR signal diverges at the Néel-temperature T_N when approaching it from higher temperatures, as can be seen in the top graph of *Figure 3-34*. In contrast, ΔH of the EPR signal of the corresponding nanoparticles does not diverge down to the lowest achievable temperatures of about 1.6 K, as shown in the bottom graph. Thus, no phase transition is observed, for either nanostructured MnS or MnSe samples. It is worth noting that both, the linewidth ΔH as well as the Curie-Weiss parameters $|\Theta|$ derived

^a For comparison reasons, MnSe was incorporated in the 3 nm pores of MCM-41 silica as well.

from inverse plots of the EPR intensity as a function of temperature, are about one order of magnitude smaller in the nanoparticles compared with bulk.

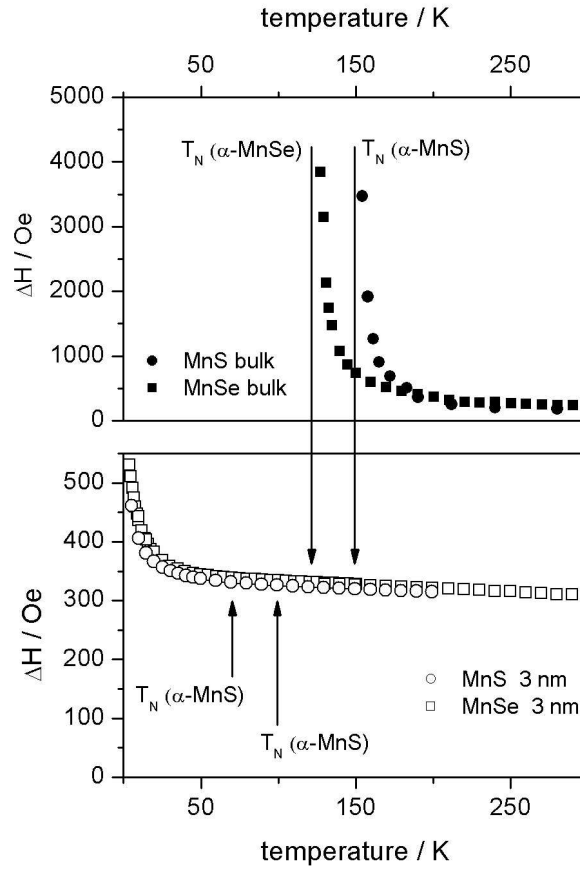


Figure 3-34: Comparison of the EPR linewidth of 3 nm MnS and MnSe nanoparticles with corresponding results for α - and β -MnS and α - and β -MnSe bulk samples.

The results are further corroborated by studying the evolution of the linewidth and the inverse intensity (which corresponds to the inverse susceptibility) of the EPR signal with increasing particle diameter. *Figure 3-35* depicts corresponding results for nanostructured MnS particles with diameters of 3, 6 and 8 nm. In agreement with the previous figure, the EPR linewidth of the 3 nm MnS particles only shows a weak tendency to diverge at the lowest temperature and the corresponding plot of the susceptibility shows basically a Curie-Weiss behaviour according to *Equation 3-8* in the entire temperature range. Both clear indications that the 3 nm MnS nanoparticles are paramagnetic down to 4 K, the lowest temperature accessible in the experiment. The situation changes for the 6 nm and 8 nm series. Although the linewidth of the 6 nm sample shows, like the 3 nm sample, only a weak tendency to diverge at low

temperatures, the corresponding inverse susceptibility starts to deviate from the Curie-Weiss behaviour at temperatures below 150 K. The 8 nm and 11 nm MnS nanoparticles show clear signs of a phase transition again. The corresponding EPR linewidths $\mu_0\Delta H$ show a maximum at about 130 K, corresponding to the shape of the graph for bulk α -MnS with its Néel-temperature of 100 K. The corresponding inverse susceptibilities show a clear deviation from the Curie-Weiss behaviour below 150 K. Thus, it can be concluded, that the phase transition from the paramagnetic to the antiferromagnetic phase is suppressed for nanoparticles < 6 nm and with increasing particle diameter the long range order of the magnetic moments is coming back.

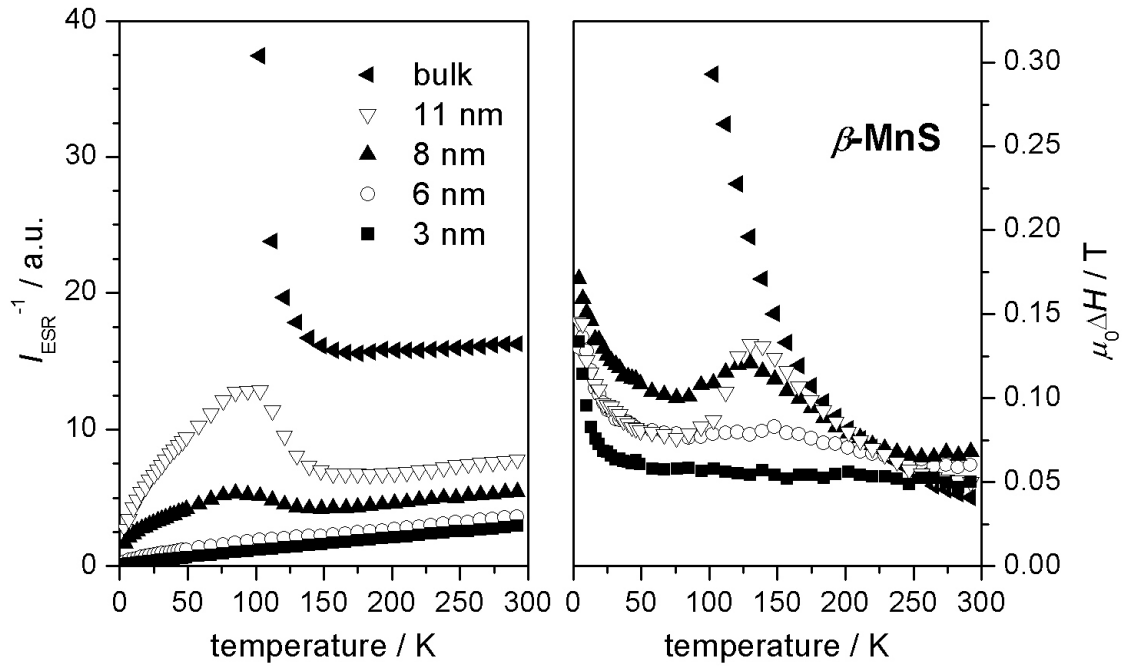


Figure 3-35: Results of EPR measurements of MnS nanoparticles with 3, 6 and 8 nm diameter. Left: Inverse EPR intensity (inverse susceptibility) as a function of temperature. Right: EPR linewidth as a function of temperature.

Optical spectroscopic studies prove that only β -MnS (*i.e.* the wurtzite *hcp*-modification) is present in the host/guest systems. The corresponding PL spectra only show the so called yellow emission band centred at about 2.2 eV. It corresponds to the Mn-internal transition between the first excited 4T_1 and the 6A_1 ground state of the Mn $3d^5$ -shell in β -MnS. This is further confirmed by the corresponding PLE spectra (Figure 3-36 a) which show a series of transitions which are typical for β -MnS and correspond

to the transitions from the ${}^6A_1({}^6S)$ ground state to the excited states ${}^4T_1({}^4G)$, ${}^4T_2({}^4G)$, ${}^4A_1({}^4G)$, ${}^4E({}^4G)$ and ${}^4T_2({}^4D)$ (abbreviated as ${}^4T_2^*$) [84,130,180].

In the following the temperature behaviour and the dependence on the nanoparticle dimensions of the Mn-internal transitions in the different MnS series will be discussed in the context of magnetic order. As pointed out previously, in bulk wide-gap antiferromagnetic manganese chalcogenides a strong correlation between the energy positions of the Mn-internal transitions and the magnetic phase transition from the paramagnetic phase into the antiferromagnetic phase is observed [180-182]. With decreasing temperature the Mn-internal transitions shift almost abruptly to higher energies at a critical temperature T_{crit} . In bulk material, $T_{crit} = T_N$ is found to be a very good approximation ($T_N(\beta\text{-MnS}) = 100$ K). Assuming that this strong correlation is also valid in nanostructures implies:

- (i) that, at low temperatures, the Mn-internal transitions of the MnS series with diameters > 6 nm (which are in the antiferromagnetic state) should be shifted to higher energies with respect to those of the 3 nm series (which are in the paramagnetic state), and
- (ii) that the energies of the Mn-internal transitions in the paramagnetic 3 nm MnS series should be independent of temperature.

Both implications are not fulfilled as can be seen in *Figure 3-36*. Part (a) shows a comparison of PLE spectra detected on the yellow luminescence at $T = 10$ K for the MnS samples with diameters of 3 to 9 nm. The peaks in the spectra correspond to the Mn-internal transitions in $\beta\text{-MnS}$. It can be clearly seen that the spectra are almost identical, *i.e.* independent of the particle diameter. In particular, there is no shift to higher energy for any of the internal transitions of the 9 nm sample with respect to those of the 3 nm sample. Furthermore, the features of the Mn-internal transitions in temperature-dependent absorption spectra of a 3 nm $\beta\text{-MnS}$ sample (which is paramagnetic down to the lowest temperature) show clear indications of an abrupt shift at a critical temperature $T_{crit} = 80$ K as can be seen in part (b) and (c) of *Figure 3-36*.

Thus the critical temperature T_{crit} is lower but very close to the Néel temperature T_N of bulk β -MnS of 100 K. It is also worth noting that the magnitude of the shift ΔE of the ${}^6A_1 \rightarrow {}^4T_2$ transition in the 3 nm sample of 21 meV is somewhat reduced compared to that reported for a bulk-like β -MnS film of about 30 meV [180]. The shift of the ${}^6A_1 \rightarrow {}^4A_1, {}^4E$ in the nanoparticle sample is only about 13 meV.

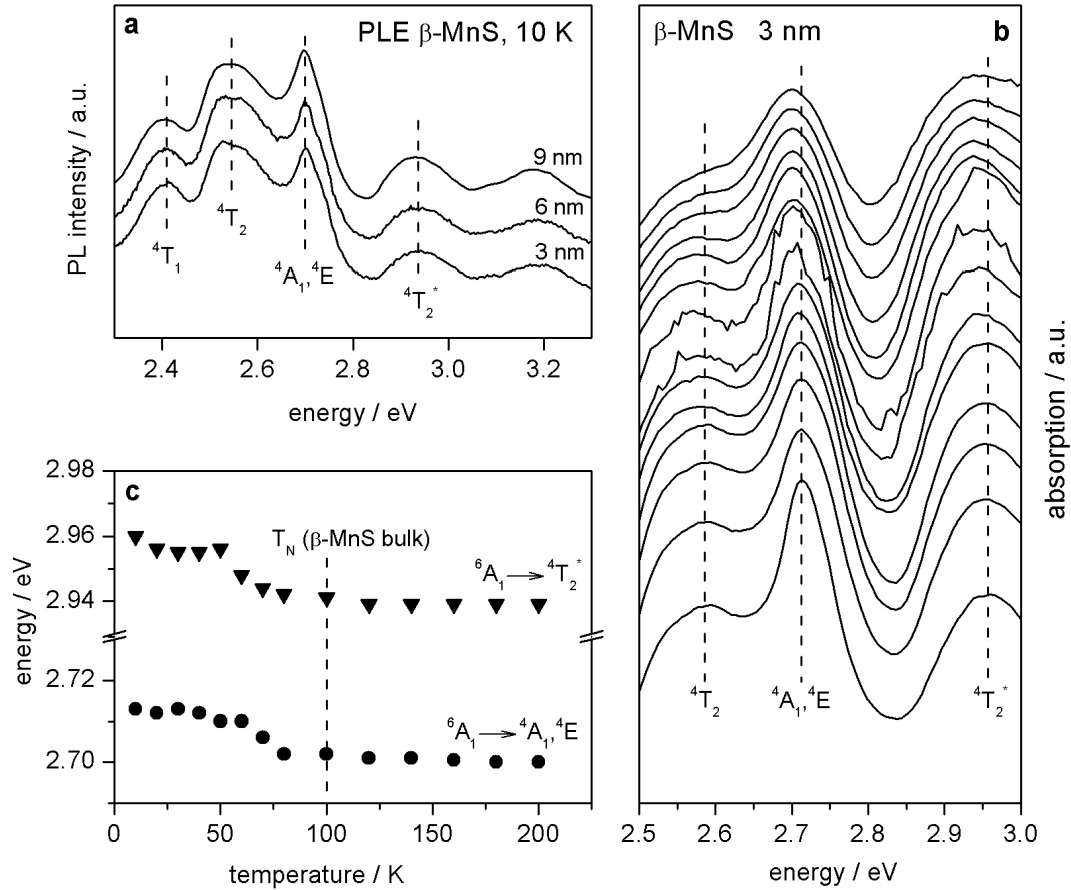


Figure 3-36: (a) Comparison of PLE results recorded at $T = 0$ K on the yellow emission band of β -MnS nanoparticles with different diameters. (b) Temperature dependent absorption spectra obtained from 3 nm particles of β -MnS in the temperature range from 10 K (bottom spectrum) to 200 K (top spectrum). The respective temperatures can be obtained from part c of this figure. The dashed lines mark the energetic positions of the internal transitions ${}^6A_1 \rightarrow {}^4T_1$, ${}^6A_1 \rightarrow {}^4A_1, {}^4E$ and ${}^6A_1 \rightarrow {}^4T_2^*$. (c) Temperature dependence of the ${}^6A_1 \rightarrow {}^4A_1, {}^4E$ and ${}^6A_1 \rightarrow {}^4T_2^*$ transitions deduced from the absorption spectra of the 3 nm β -MnS particles. The dashed line indicates the Néel-temperature of bulk β -MnS.

The spin-ordering-induced energy relaxation for a Mn^{2+} ion in the ground state ($S = 5/2$) in $\beta\text{-MnS}$ is given by

$$E_{gr}(0 \text{ K}) = (4J_{nn} - 2J_{nn}) S^2 \approx 4J_{nn} S^2 \quad \text{Equation 3-25}$$

At sufficiently low excitation densities an excited (single) Mn^{2+} ion can be assumed to be placed in an unchanged mean spin field of neighbouring Mn^{2+} ions. For the spin-ordering-induced energy relaxation $E_{ex}(0)$ of such an excited Mn^{2+} ion in one of the lowest energy states ($S' = 3/2$) one derives for $\beta\text{-MnS}$

$$E_{ex}(0 \text{ K}) = (4J_{nn}^{ex} - 2J_{nnn}^{ex}) S S' \approx 4J_{nn}^{ex} S S' \quad \text{Equation 3-26}$$

where J_{nn}^{ex} and J_{nnn}^{ex} denote the various exchange interaction parameters between the considered excited Mn^{2+} ion and a nearest neighbored or next-nearest neighbored Mn^{2+} ion in the ground state.

The measured total spin-ordering-induced shift of the various excitation peaks, $\Delta E = (E_{ex} - E_{gr})_{T=0} - (E_{ex} - E_{gr})_{T=T_{crit}}$, is then given by

$$\begin{aligned} \Delta E &= 4S (J_{nn} S - J_{nn}^{ex} S') - 2S (J_{nnn} S - J_{nnn}^{ex} S') \\ &\approx 25J_{nn} - 15J_{nn}^{ex} \end{aligned} \quad \text{Equation 3-27}$$

Equation 3-27 indicates that the observed shift of the Mn-internal transitions at T_{crit} is to a first approximation determined by a local magnetic ordering effect. In particular, it can be seen that in the case of $\beta\text{-MnS}$ a non-zero shift is still anticipated even if nearest-neighbour coupling only is accounted for. This means that the length scale of magnetic ordering defining T_{crit} is much smaller (less than a magnetic unit cell) than the length scales (several magnetic unit cells) of the long-range magnetic order defining T_N , which is detected in the EPR experiment by the divergence of the spin correlation length. In bulk MnS (where the magnetic unit cell is small compared to the lateral dimensions of the crystal) even the long-range magnetic order is basically determined by the local magnetic ordering, *i.e.* site symmetry, because of the high symmetry and periodicity of the lattice and because no additional constraints due to shape and surfaces

are present. This leads to $T_{crit}(bulk) \approx T_N(bulk)$ although the relevant length scales are different. The additional constraints due to the reduced dimensions lift this quasi-degeneracy and results in $T_N(nano) \ll T_{crit}(nano)$, as observed for the 3 nm MnS particles where the diameter approaches the extension of a magnetic unit cell. In summary, the results indicate that the long range antiferromagnetic coupling between the Mn^{2+} spins in the MnS nanoparticles can be strongly suppressed because of their reduced dimensions, in agreement with the results on the corresponding DMS $Zn_{1-x}Mn_xS$ and $Cd_{1-x}Mn_xS$ nanoparticles described in *Chapter 3.2.8*. However, the local coupling of a Mn^{2+} spin to the neighbouring spins (expressed by the nearest neighbour and the next-nearest neighbour coupling constants J_{nn} and J_{nnn}) is approximately the same as in bulk. This is somewhat expected as there is no change of the average local site symmetry in the MnS nanoparticles compared to bulk MnS.

3.2.10. Conclusions

In *Chapter 3.2* the successful syntheses of various semiconductor compounds within the pores of different mesoporous materials with varying pore diameters were shown.

Powder X-ray diffraction proved the preservation of the host compounds and showed that the formation of the respective guest compounds had taken place preferentially inside the respective pore system. Nitrogen physisorption measurements indicated the slow filling of the pores and the distortion of the cylindrical pore geometry due to incorporated nanoparticles. TEM investigation also proved the preservation of the host structures and gave a first hint of elongated spherical (or ellipsoidal) particles inside the pores.

The conversion of the acetates to the sulphides was proved by IR spectroscopy and the crystallinity of the nanoparticles was demonstrated via Raman investigations. The latter also proved the existence of elongated particles inside the pore systems. The doping of the binary semiconductor with Mn^{2+} was proved by X-ray absorption

spectroscopy which also revealed the local structure around the randomly distributed manganese inside the II/VI compound is of a distorted "MnS" geometry kind.

Optical photoluminescence measurements showed the dependence of the band gap on particle size and doping level x . Finally the magnetic properties of the nanostructured DMS compounds were investigated via electron paramagnetic resonance spectroscopy. A dependence of the EPR linewidth and the Curie-Weiss parameter $|\Theta|$ on the size and the doping level x in the nanoparticles was observed for all DMS samples. The antiferromagnetic-paramagnetic phase transition in MnS was found to be suppressed for particle smaller than 6 nm. Although the long range antiferromagnetic coupling between the Mn^{2+} spins is suppressed, the local coupling of a Mn^{2+} spin to the neighbouring spins remains unaffected by the reduced dimensions of the MnS nanoparticles.

4. Summary

Mesoporous materials have opened new pathways for the formation of nanostructured host/guest compounds. At first highly ordered mesoporous materials with pore sizes of about 3 nm were accessible through the M41S family with either hexagonal (MCM-41) or cubic symmetry (MCM-48). By using different amphiphilic structure directing agents such as triblock copolymers (Pluronic[®]) hexagonally ordered mesoporous materials containing large pores with diameters up to 10 nm or more could be synthesised (so called SBA-15). Fine tuning the pore size of SBA-15 from 5 to 30 nm is possible just by varying the synthesis temperature, according to literature. The synthesis of nanostructured guest compounds within a mesoporous matrix was at first interesting only due to possible application of the host/guest compounds in the field of catalysis.

The preparation of nanoparticles and the careful study of the unusual physical properties has also become a mayor field of research for chemists and physicists. Rare-earth and transition-metal doped II-VI semiconductors and semiconductor nanostructures are especially of interest because of their optical and magnetic properties. Magnetic semiconductors and semiconductor nanostructures are possible candidates for spin aligners and spin injectors in future spintronic devices. The family of $\text{II}_{1-x}\text{Mn}_x\text{VI}$ compounds are a subgroup of the so called diluted magnetic semiconductors (DMS). These DMS materials have gained considerable interest due to their unusual magneto-optical properties. The reduction of the lateral dimensions of magnetic semiconductor nanostructures does significantly affect their magnetic properties. An understanding of the magnetism at reduced dimensions is essential for device miniaturisation. The magnetic properties of a $\text{A}_{1-x}\text{Mn}_x\text{B}$ nanoparticle – similar to the optical properties – strongly depend on the distribution of the manganese within the nanoparticle and thus on the synthesis procedure. Most of the procedures to obtain 1D- or 2D-nanostructures, *i.e.* quantum dots and quantum wells, require non-equilibrium growth conditions, which can be realised by molecular beam epitaxy under ultra high

vacuum. In order to fabricate 3D quantum wires the easiest way is to start with two-dimensional quantum wells and to use a subsequent etching procedure.

The utilisation of mesopores as a kind of "nano-reactor" is a relatively new approach for the synthesis of highly ordered arrays of well size-defined nanostructures. In a comparatively simple synthesis approach nanoparticles with well-defined diameters are accessible only by choosing a mesoporous material with the "right" pore size. Furthermore, the hexagonal order of MCM-41 and SBA-15 silica provides the possibility of growing quantum wires inside the channels. The incorporation of semiconductors into the pores is also promising to that effect, that the silica wall structure of the host materials with its large band gap then serves as a barrier between single particles or wires.

In this work the successful formation of several DMS materials inside various mesoporous host matrices is shown. For that purpose, different high quality mesoporous silicas were synthesised. Because of the possibility to obtain nanostructured quantum wires inside the respective pore systems, hexagonally ordered structures of the MCM-41 and SBA-15 kind were chosen as hosts for the intra-pore formation of the DMS nanoparticles. Later on it became obvious though, that the formation of nanowires inside the pore systems was not successful. Instead, particles with an elongated spherical or ellipsoidal shape were formed. With powder X-ray diffraction the hexagonal order of the silica was proved. The diffraction patterns of the pristine host structures could all be indexed according to a hexagonal phase. The peaks at diffraction angles $2\theta > 2^\circ$ indicated a high degree of long range order. This was further substantiated by TEM analysis. Over several hundreds of nanometres a perfect hexagonal arrangement of the pores was clearly visible. Physisorption showed the high specific surface areas of the respective materials. Depending on the pore size, surface areas of over $1000 \text{ m}^2/\text{g}$ could be obtained. From the sorption experiments the pore diameters of the host compounds were calculated using the well established algorithm of Barrett, Joyner and Halenda. Although this theory underestimates the pore diameters in the small mesopore range of about 1 nm, it allows the comparison of different pore

sizes and revealed that all host materials had narrow pore size distributions with well-defined maxima at 3, 6 and 9 nm. With these highly ordered and pore size defined materials available, reasonable host structures for the intra-pore synthesis of nanoparticles can be synthesised. The following investigation, regarding the dependence of the physical properties of the nanostructures on their size, could now be carried out within a very defined size range.

The successful incorporation of the respective DMS compounds was shown by X-ray diffraction, TEM and physisorption. The diffraction patterns revealed the preservation of the mesoporous host matrices even after several incorporation/conversion cycles. The absence of peaks at higher angles 2θ indicated that no bulk material had formed and that the formation of the DMS compounds had taken place preferentially inside the respective pore systems. This was also apparent from the TEM pictures: the hexagonal arrangement of the pores was still clearly visible and no bigger particles were lying on the outer surface. Furthermore it could be seen from the TEM pictures with a cross sectional view of the host/guest compounds that the particles inside the pores are of an elongated spherical or ellipsoidal shape. The sorption studies also revealed the remaining mesoporosity of the samples and showed that the specific surface area was decreasing with each impregnation/conversion cycle. The remaining pore diameter remained nearly the same as in the pristine mesoporous material but the total number of freely accessible pores was found to be decreasing with every impregnation/conversion step. This was an indication for a blocking of the entrances of the pores with the nanoparticles which were formed inside the pore system.

The conversion of the acetates, which were the starting materials, to the sulphides was demonstrated by IR spectroscopy. The corresponding bands of the C=O valence vibration ($1420\text{--}1580\text{ cm}^{-1}$) in the spectra had completely vanished in the finished product. Raman spectroscopy proved the good crystallinity of the nanoparticles and showed a red-shift of the peak positions with decreasing particle diameter due to quantum confinement. By analysing the lineshape of the LO-phonon with the model of

Campbell and Fauchet the shape of the nanoparticles was – as already indicated in the TEM pictures – found to be of an elongated spherical or ellipsoidal shape.

X-ray absorption spectroscopy revealed that no binary sulphides were formed inside the pore systems and the nanoparticles were really doped with randomly distributed manganese, resulting in a $A_{1-x}Mn_xS$ kind of structure. The local structure around the localised Mn^{2+} ions was found to be of a distorted "MnS" geometry. EPR measurements also showed, that a $A_{1-x}Mn_xS$ structure was formed and that the crystal structure is wurtzite for $x > 0.01$ for all samples.

PL measurements were carried out to investigate the optical properties of the nanostructured DMS particles. The internal Mn transitions were analysed with the Tanabe-Sugano-model, which revealed that the crystal structure of the nanoparticles was comparable to that of bulk crystals. The band gap related feature in the PLE spectra showed an increasing blue-shift with decreasing particle size due to quantum confinement. For the $Cd_{1-x}Mn_xS$ nanoparticles the blue shift was found to be of about 200 meV, for the $Zn_{1-x}Mn_xS$ it was about 180 meV. The largest shift of about 350 meV was found for 3 nm $Cd_{1-x}Mn_xSe$ particles. Also an increased band gap bowing was found for the nanoparticles of $Cd_{1-x}Mn_xS$ and $Cd_{1-x}Mn_xSe$, whereas no bowing was observed for the $Zn_{1-x}Mn_xS$ particles. This effect could be explained by the dependence of the $p-d$ exchange parameter β and the susceptibility χ on the reduced dimensions in nanoparticles and was found to be consistent to literature.

The magnetic behaviour of the DMS compounds was investigated with the analysis of the EPR data. It was found that the susceptibility χ and the Curie-Weiss parameter $|\Theta|$ are strongly affected by the reduced lateral dimensions of the nanoparticles (< 10 nm). Here, a better agreement with theoretical values was obtained, if a wire-like structure of the nanoparticles was assumed. However a perfect agreement was not observed, hence, it can still be presumed that the particles are of an ellipsoidal shape. The microscopic coupling between the Mn-ions (*e.g.* the nearest neighbour and next-nearest neighbour exchange-constants J_{nn} and J_{nnn}) though was not found to be altered. The observed macroscopic modifications could be explained by geometrical

restrictions in the nanoparticles: the number of neighbours in the various shells around a manganese ion in the surface region is considerably reduced compared to a manganese ion in the bulk of the structure. This effect was found to become increasingly important with decreasing lateral dimensions of the nanostructure.

Furthermore a suppression of the paramagnetic to antiferromagnetic phase transition was found for MnS nanoparticles with lateral dimensions < 6 nm. While the long range antiferromagnetic coupling between the Mn^{2+} spins was found to be suppressed, *i.e.* $T_N \rightarrow 0$, the local coupling of a Mn^{2+} spin to the neighbouring spins remained unaffected by the reduced dimensions of the MnS nanoparticles, *i.e.* $T_{crit.} (nanoparticle) \approx T_{crit.} (bulk)$.

5. Zusammenfassung (German summary)

Mesoporöse Materialien haben ein neues Feld für die Synthese von nanostrukturierten Wirt/Gast-Systemen geöffnet. Hochgeordnete mesoporöse Substanzen mit Porendurchmessern von circa 3 nm wurden zuerst in der Familie der sogenannten M41S Materialien hergestellt. Verschiedene flüssigkristalline Phasen der verwendeten Strukturdirigenten führten zu hexagonal (MCM-41) oder kubisch (MCM-48) geordneten Systemen. Durch die Verwendung anderer Amphiphile, wie Triblock-Copolymeren (Pluronic[®]), konnten hexagonal geordnete Porensysteme mit Porendurchmessern von bis zu 10 nm hergestellt werden. Bei diese sogenannten SBA-15 Phasen läßt sich der Porendurchmesser durch geeignete Variation der Synthesetemperatur zwischen 5 und 30 nm "frei" einstellen. Die Synthese von nanostrukturierten Wirtsverbindungen innerhalb der Mesoporen einer Wirtsmatrix war zunächst nur in Hinblick auf spätere katalytische Eigenschaften der fertigen Wirt/Gast-Verbindung interessant.

Die Herstellung von Nanopartikeln und die sorgfältige Untersuchung ihrer ungewöhnlichen physikalischen Eigenschaften ist ebenfalls zu einem großen Betätigungsfeld von Chemikern und Physikern geworden. II/VI Halbleiter, die mit Seltenerd- oder Übergangsmetallen dotiert sind, sind wegen ihrer speziellen optischen und magnetischen Eigenschaften von besonderem Interesse. Magnetische Halbleiter und Halbleiternanostrukturen könnten später in der "Spintronik" Einsatz finden. Verbindungen des Typs $\text{II}_{1-x}\text{Mn}_x\text{VI}$ bilden die Klasse der sogenannten magnetisch-dotierten Halbleiter (*diluted magnetic semiconductors*, DMS). Diese DMS Materialien haben in der letzten Zeit wegen ihrer speziellen magneto-optischen Eigenschaften Aufmerksamkeit erregt. Die Miniaturisierung der lateralen Dimensionen von DMS-Nanostrukturen wirkt sich deutlich auf ihre magnetischen Eigenschaften aus. Das Verständnis dieser magnetischen Eigenschaften in einer derartig verkleinerten Struktur ist von fundamentaler Bedeutung für die Miniaturisierung von Bauteilen. Die magnetischen Eigenschaften eines $\text{A}_{1-x}\text{Mn}_x\text{S}$ Nanoteilchens, ähnlich wie auch seine optischen, hängen stark von der Verteilung des Mangans innerhalb des Nanopartikels

ab. Darauf hat auch die Art der Synthese maßgeblichen Einfluß. Herkömmliche 1D- oder 2D-Nanostrukturen, sogenannte *quantum dots* und *quantum wells*, werden im Ultrahochvakuum mittels Molekülstrahl-Epitaxie hergestellt. Um 3D-Strukturen in Form von "Quantendrähten" (*quantum wires*) herzustellen, wird normalerweise von einer 2D-Struktur ausgegangen, die dann mit einer Ätztechnik in eine 3D-Struktur umgewandelt wird.

Die Verwendung von Mesoporen als größenlimitierender "Mini-Reaktor" ist eine relativ neue Methode für die Synthese von hochgeordneten Feldern von größendefinierten Nanostrukturen. In dem vergleichsweise einfachen Syntheseansatz werden die unterschiedlichen Größen der Nanopartikel durch die Wahl einer mesoporösen Matrix mit der "richtigen" Porengröße realisiert. Außerdem bieten die hexagonal geordneten Porensysteme von MCM-41 und SBA-15 die Möglichkeit Quantendrähte innerhalb der Poren herzustellen. Des weiteren bieten die Silica-Wände der Wirtstrukturen den Vorteil, daß sie mit ihren großen Bandlücken als eine Art Barriere zwischen den einzelnen Partikeln oder Drähten wirken.

In dieser Arbeit wurde die erfolgreiche Synthese unterschiedlicher DMS Materialien innerhalb verschiedener mesoporöser Wirtmatrices gezeigt. Zu diesem Zweck wurde zunächst mesoporöses Silica hoher Qualität synthetisiert. Wegen der Möglichkeit Quantendrähte innerhalb des jeweiligen Porensystems zu erhalten, wurden für die Synthese von Nanopartikeln innerhalb der Mesoporen die hexagonalen Strukturen von MCM-41 und SBA-15 Silica verwendet. Die hexagonale Ordnung der Poren wurde mittels Röntgenpulverdiffraktometrie bewiesen. In den jeweiligen Diffraktogrammen konnten alle Reflexe einer hexagonalen Phase zugeordnet werden. Die Reflexe im Winkelbereich von $2\theta > 2^\circ$ zeigten die hohe langreichweitige Ordnung der Poren an. Letzteres wurde auch in den TEM Aufnahmen deutlich, in denen eine hexagonale Ordnung der Poren über mehrere hundert Nanometer deutlich erkennbar war. Aus Physisorptionsmessungen konnte eine hohe innere Oberfläche der Materialien errechnet werden. Je nach Porengröße konnten Oberflächen von über $1000 \text{ m}^2/\text{g}$ realisiert werden. Außerdem wurde nach der Theorie von Barrett, Joyner und Halenda

der Porendurchmesser der Wirtstrukturen bestimmt. Obwohl es bekannt ist, daß dieser Ansatz Porendurchmesser im unteren Mesoporenbereich um ungefähr einen Nanometer zu klein berechnet, ist er doch vorzüglich geeignet um Vergleiche verschiedener Durchmesser anzustellen. Alle untersuchten Wirtstrukturen zeigten schmale Porendurchmesserverteilungen mit gut definierten Maxima von 3, 6 und 9 nm. Die so synthetisierten und charakterisierten mesoporösen Materialien stellten hervorragende Wirtstrukturen für die Synthese von Nanopartikeln innerhalb der Poren dar. Die folgenden Untersuchungen in bezug auf die Größenabhängigkeit der physikalischen Eigenschaften der Nanopartikel konnten nun innerhalb eines sehr gut definierten Größenbereichs durchgeführt werden.

Die erfolgreiche Einlagerung der unterschiedlichen DMS Materialien wurde mittels Röntgenpulverdiffraktometrie, TEM und Sorptionsmessungen gezeigt. Die Diffraktogramme zeigten auch nach mehreren Einlagerungsschritten noch den Erhalt der hexagonalen Ordnung der jeweiligen Wirtstruktur an. Auch zeigte das völlige Fehlen von Reflexen bei höheren Winkeln 2θ an, daß kein bulk-Material^a auf der äußeren Oberfläche gebildet wurde und die Synthese der DMS-Verbindungen ausschließlich innerhalb der Poren stattgefunden hatte. Dies wurde wiederum auch aus den TEM-Aufnahmen deutlich: die hexagonale Anordnung der Poren war weiterhin deutlich erkennbar und keinerlei größere Partikel lagen auf der äußeren Oberfläche. Des weiteren konnte man bei einem Blick auf den Querschnitt der Poren erkennen, daß die eingelagerten Partikel eine elongiert-sphärische oder ellipsoide Form aufwiesen. Die Sorptionsmessungen zeigten ebenfalls an, daß auch nach den verschiedenen Einlagerungsschritten noch Mesoporosität vorhanden war und die innere Oberfläche der Wirtstrukturen nahm mit jedem Einlagerungsschritt weiter ab. Die Porendurchmesser blieben nach den jeweiligen Einlagerungen fast die gleichen wie in den reinen mesoporösen Materialien, allerdings nahm die Anzahl der frei zugänglichen Poren mit jedem Einlagerungsschritt ab. Dies konnte als Hinweis darauf gedeutet werden, daß die in den Poren gebildeten Nanopartikel die Eingänge zu den Poren blockierten.

^a Der Begriff "bulk" beschreibt im internationalen Sprachgebrauch die kompakte Form eines Stoffes.

Die Umwandlung der als Edukte verwendeten Acetate zu den Sulfiden wurde mittels IR-Spektroskopie bewiesen. Die zugehörigen Banden der C=O Valenzschwingung ($1420\text{-}1580\text{ cm}^{-1}$) in den Spektren fehlten im fertigen Produkt völlig. Mit Hilfe von Raman-Spektroskopie konnte die gute Kristallinität der DMS-Partikel gezeigt werden und die aufgrund von Größenquantisierung auftretende Rotverschiebung der Peak-Positionen. Durch Analyse des Linienprofils der LO-Phononbande nach dem Modell von Campbell und Fauchet konnte – wie auch schon aus den TEM-Aufnahmen ersichtlich – gezeigt werden, daß es sich bei den eingelagerten Nanopartikeln um elongiert-sphärische oder ellipsoide Teilchen handelt.

Durch Röntgenabsorptionsspektroskopie wurde ersichtlich, daß es sich bei den eingelagerten Nanoteilchen tatsächlich um dotierte ternäre Strukturen der Formel $A_{1-x}Mn_xS$ handelt und keine binären Verbindungen gebildet wurden. Die lokale Struktur um die einzelnen Manganionen entsprach einer verzerrten "MnS"-Geometrie. EPR Messungen zeigten weiterhin, daß die Kristallstruktur aller $A_{1-x}Mn_xS$ Nanopartikel für $x > 0.01$ Wurtzit ist.

Photolumineszenz-Messungen wurden durchgeführt, um die optischen Eigenschaften der nanostrukturierten DMS-Teilchen zu untersuchen. Die Energien der internen Manganübergänge wurden mit Hilfe des Tanabe-Sugano-Modells untersucht und es wurde ein dem bulk-Material ähnliches Kristallfeld in den Nanostrukturen gefunden. Die aus den PLE-Spektren bestimmte Bandlücke zeigte aufgrund von Größenquantisierung eine zunehmende Blauverschiebung mit abnehmendem Teilchendurchmesser. Für die $Cd_{1-x}Mn_xS$ Nanopartikel wurde eine Blauverschiebung von ungefähr 200 meV gefunden, für die $Zn_{1-x}Mn_xS$ Nanopartikel lag der Wert bei ungefähr 180 meV. Die größte Verschiebung von ungefähr 350 meV wurde für die 3 nm $Cd_{1-x}Mn_xSe$ Partikel gefunden. Des weiteren wurde eine verstärkte Bandlückenverbiegung für die Nanopartikel von $Cd_{1-x}Mn_xS$ und $Cd_{1-x}Mn_xSe$ gefunden, während für die $Zn_{1-x}Mn_xS$ Partikel keine solche Verbiegung beobachtet wurde. Dies konnte durch die Abhängigkeit des p - d Austauschparameters β und der Suszeptibilität χ

von den reduzierten Dimensionen in Nanopartikeln erklärt werden und war in Übereinstimmung mit der Literatur.

Die magnetischen Eigenschaften der DMS-Partikel wurden untersucht, indem die EPR-Daten analysiert wurden. Es wurde eine deutliche Beeinflussung der Suszeptibilität χ und des Curie-Weiss-Parameters $|\Theta|$ durch die verkleinerten lateralen Dimensionen der Nanopartikel (< 10 nm) festgestellt. Hierbei wurde eine bessere Übereinstimmung mit theoretischen Werten festgestellt, wenn eine draht-ähnliche Form der Nanostrukturen angenommen wurde. Eine perfekte Übereinstimmung gab es allerdings auch hier nicht und es kann weiterhin angenommen werden, daß es sich bei den Partikeln um ellipsoide Strukturen handelt. Es wurde gefunden, daß die mikroskopische Kopplung zwischen den Manganionen (also die Kopplungskonstanten für die nächsten und übernächsten Nachbarn J_{nn} und J_{nnn}) nicht verändert wird. Die beobachteten makroskopischen Veränderungen konnten durch die auftretenden geometrischen Einschränkungen in den Nanopartikeln erklärt werden: Die Zahl der Nachbarn in den unterschiedlichen Schalen um ein Manganion an der Oberfläche eines Nanopartikels ist deutlich geringer, verglichen mit einem Manganion im bulk-artigen Volumen eines solchen Partikels. Es wurde gefunden, daß dieser Effekt zunehmend wichtig wird, je kleiner die lateralen Dimensionen des Nanoteilchens werden.

Des weiteren konnte ein Unterdrückung des antiferromagnetisch-paramagnetischen Phasenübergangs für MnS-Nanopartikel mit Durchmessern < 6 nm festgestellt werden. Während diese langreichweitige antiferromagnetische Kopplung der Mn^{2+} -Spins unterdrückt wurde, also $T_N \rightarrow 0$, blieb die lokale Kopplung eines Mn^{2+} -Spins mit einem benachbarten Spin unberührt von den verkleinerten Dimensionen der MnS-Nanopartikel, also $T_{crit.}(\text{Nanopartikel}) \approx T_{crit.}(\text{bulk})$.

6. References

- [1] K.S.W. Sing, D.H. Everett, R.A.W. Haul, L. Mouscou, R.A. Pierotti, J. Rouquerol, T. Siemieniewska *Pure & Appl. Chem.* **1985**, 57, 603.
- [2] C.T. Kresge, M.E. Leonowicz, W.J. Roth, J.C. Vartuli, J.S. Beck *Nature* **1992**, 359, 710.
- [3] J.S. Beck, J.C. Vartuli, W.J. Roth, M.E. Leonowicz, C.T. Kresge, K.D. Schmitt, C.T.-W. Chu, D.H. Olson, E.W. Sheppard, S.B. McCullen, J.B. Higgins, J.L. Schlenker *J. Am. Chem. Soc.* **1992**, 114, 10834.
- [4] P. Behrens *Adv. Mater.* **1993**, 5, 127.
- [5] A. Corma *Chem. Rev.* **1997**, 97, 2373.
- [6] J.Y. Ying, C.P. Mehnert, M.S. Wong *Angew. Chem. Int. Ed.* **1999**, 38, 56.
- [7] R. Köhn, M. Fröba *Catal. Today* **2001**, 68, 227.
- [8] P.J. Branton, P.G. Hall, K.S.W. Sing *J. Chem. Soc., Chem. Commun.* **1993**, 1257.
- [9] P.J. Branton, P.G. Hall, K.S.W. Sing, H. Reichert, F. Schüth, K. K. Unger *J. Chem. Soc., Faraday Trans.* **1994**, 90, 2965.
- [10] J. H. Petropoulos *Langmuir* **1996**, 12, 4814.
- [11] K. Morishige, H. Fujii, M. Uga, D. Kinukawa *Langmuir* **1997**, 13, 3494.
- [12] M. Kruk, M. Jaroniec, R. Ryoo, J. M. Kim *Chem. Mater.* **1999**, 11, 2568.
- [13] P. I. Ravikovitch, A. V. Neimark *Langmuir* **2000**, 16, 2419.
- [14] M. Thommes, R. Köhn, M. Fröba *J. Phys. Chem. B* **2000**, 104, 7932.
- [15] J.C. Vartuli, A. Malek, W.J. Roth, C.T. Kresge, S.B. McCullen, *Microporous Mesoporous Mater.* **2001**, 44-45, 691.
- [16] K. Moller, T. Bein *Chem. Mater.* **1998**, 10, 2950.
- [17] Q. Huo, D.I. Margolese, U. Ciesla, P. Feng, T.E. Gier, P. Sieger, R. Leon, P.M. Petroff, F. Schüth, G.D. Stucky *Nature* **1994**, 368, 317.
- [18] Q. Huo, D.I. Margolese, U. Ciesla, D.G. Demuth, P. Feng, T.E. Gier, P. Sieger, A. Firouzi, B.F. Chmelka, F. Schüth, G.D. Stucky *Chem. Mater.* **1994**, 6, 1176.
- [19] P.T. Tanev, T.J. Pinnavaia, *Science* **1995**, 267, 865.
- [20] S.A. Bagshaw, E. Prouzet, T.J. Pinnavaia, *Science* **1995**, 269, 1242.
- [21] D. Zhao, J. Feng, Q. Huo, N. Melosh, G.H. Fredrickson, B.F. Chmelka, G.D. Stucky *Science* **1998**, 279, 548.

- [22] Q. Huo, D.I. Margolese, U. Ciesla, P. Feng, T.E. Gier, P. Sieger, R. Leon, P.M. Petroff, F. Schüth, G. Stucky *Nature* **1994**, 368, 317.
- [23] A. Sayari *Chem. Mater.* **1996**, 8, 1840.
- [24] X.S. Zhao, G.Q. Lu, G.J. Millar *Ind. Eng. Chem. Res.* **1996**, 35, 2075.
- [25] J.S. Beck, J.C. Vartuli *Curr. Opin. Solid State Mater. Sci.* **1996**, 1, 76.
- [26] P. Behrens *Angew. Chem. Int. Ed.* **1996**, 35, 515.
- [27] D. Zhao, P. Yang, Q. Huo., B.F. Chmelka, G.D. Stucky *Curr. Opin. Solid State Mater. Sci.* **1998**, 3, 111.
- [28] M. Linden, S. Schacht, F. Schüth, A. Steel, K.K. Unger *J. Porous. Mater.* **1998**, 5, 177.
- [29] U. Ciesla, F. Schüth *Microporous Mesoporous Mater.* **1999**, 27, 131.
- [30] S. Inagaki, Y. Fukushima, K. Kuroda *J. Chem. Soc., Chem. Commun.* **1993**, 680.
- [31] Q. Huo, R. Leon, P.M. Petroff, G.D. Stucky *Science* **1995**, 268, 1324.
- [32] G.D. Stucky, D. Zhao, P. Yang, W. Lukens, N. Melosh, B.F. Chmelka *Stud. Surf. Sci. Catal.* **1998**, 117, 1.
- [33] D. Zhao, Q. Huo, J. Feng, B.F. Chmelka, G.D. Stucky *J. Am. Chem. Soc.* **1998**, 120, 6024.
- 34 D. Zhao, P. Yang, N. Melosh, J. Feng, B.F. Chmelka, G.D. Stucky *Adv. Mater.* **1998**, 10, 1380.
- [35] F. Brieler, M. Brehm, L. Chen, P.J. Klar, W. Heimbrod, M. Fröba *Stud. Surf. Sci. Catal.* **2001**, 135, 160.
- [36] M.S. Morey, A. Davidson, G.D. Stucky *J. Porous Mater.* **1998**, 5, 195.
- [37] A. Firouzi, D. Kumar, L.M. Bull, T. Besier, P. Sieger, Q. Huo, S.A. Walker, J.A. Zasadzinski, C. Glinka, J. Nicol, D. Margolese, G.D. Stucky, B.F. Chmelka *Science* **1995**, 267, 1138.
- [38] M.E. Davis, C.-Y. Chen, S. Burkett, R.F. Lobo *Mat. Res. Soc. Symp. Proc.* **1994**, 346, 831.
- [39] C.-F. Cheng, Z. Chan, J. Klinowski *Langmuir* **1995**, 11, 2815.
- [40] T. Yanagisawa, T. Shimizu, K. Kuroda, C. Kato *Bull. Chem. Soc. Jpn.* **1990**, 63, 988.
- [41] T. Yanagisawa, T. Shimizu, K. Kuroda C. Kato *Bull. Chem. Soc. Jpn.* **1999**, 63, 988.
- [42] G.S. Attard, J.C. Glyde, C.G. Göltner *Nature* **1995**, 378, 366.

- [43] F. Kleitz, S.H. Choi, R. Ryoo *Chem. Commun.* **2003**, 2136.
- [44] F. Kleitz, D. Liu, G.M. Anilkumar, I.-S. Park, L.A. Solovyov, A.N. Shmakov, R. Ryoo *J. Phys. Chem. B* **2003**, *107*, 14296.
- [45] S.K. Jana, R. Nishida, K. Shindo, T. Kugita, S. Namba *Microporous Mesoporous Mater.* **2004**, *68*, 133.
- [46] C. Petit, P. Lixon, M.P. Pileni *J. Phys. Chem.* **1990**, *94*, 1598.
- [47] C. Petit, T.K. Jain, F. Billoudet, M.P. Pileni *Langmuir* **1994**, *10*, 4446.
- [48] L. Motte, C. Petit, L. Boulanger, P. Lixon, M.P. Pileni *Langmuir* **1992**, *8*, 1049.
- [49] H. Sato, T. Hirai, I. Komasa *Ind. Eng. Chem. Res.* **1995**, *34*, 2493.
- [50] J. Tanori, N. Duxin, C. Petit, P. Veillet, M.P. Pileni *Colloid Polym. Sci.* **1995**, *273*, 886.
- [51] J. Cizeron, M.P. Pileni *J. Phys. Chem.* **1995**, *99*, 17410.
- [52] J. Cizeron, M.P. Pileni *J. Phys. Chem. B* **1997**, *101*, 8887.
- [53] S.K. Haram, A.R. Mahadeshwar, S.G. Dixit *J. Phys. Chem.* **1996**, *100*, 5868.
- [54] M.P. Pileni *Langmuir* **1997**, *13*, 3266.
- [55] M.L. Curri, A. Agostiano, L. Manna, M.D. Monica, M. Catalano, L. Chiavarone, V. Spagnolo, M. Lugara *J. Phys. Chem. B* **2000**, *104*, 8391.
- [56] J.C. Hulteen, C.R. Martin *J. Mater. Chem.* **1997**, *7*, 1075.
- [57] M.P. Pileni *Cryst. Res. Technol.* **1998**, *33*, 1155.
- [58] L.E. Brus *J. Chem. Phys.* **1984**, *80*, 4403.
- [59] L.E. Nair, S. Sinha, K.C. Rustagi *Phys. Rev. B* **1987**, *35*, 4098.
- [60] A. Henglein *Chem. Rev.* **1989**, *89*, 1861.
- [61] P.E. Lippens, M. Lannoo *Phys. Rev. B* **1989**, *39*, 10935.
- [62] Y. Wang, N. Herron *Phys. Rev. B* **1990**, *42*, 7253.
- [63] C.B. Murray, D.J. Norris, M.G. Bawendi *J. Am. Chem. Soc.* **1993**, *115*, 8706.
- [64] T. Vossmeier, L. Katsikas, M. Giersig, I.G. Popovic, K. Diesner, A. Chemseddine, A. Eychmüller, H. Weller *J. Phys. Chem.* **1994**, *98*, 7665.
- [65] A.P. Alivasitatos *J. Phys. Chem.* **1996**, *100*, 13226.
- [66] A.C. Gossard, S. Fafard *Solid State Commun.* **1994**, *92*, 63.
- [67] G.W. Bryant *J. Lumin.* **1996**, *70*, 108.
- [68] R. Nötzel *Semicond. Sci. Technol.* **1996**, *11*, 1365.
- [69] A. Ekimov *J. Lumin.* **1996**, *70*, 1.
- [70] G.A. Prinz *Science* **1998**, *282*, 1660.

- [71] N.B. Brandt, V.V. Moshchalkov *Adv. Phys.* **1984**, 33, 193.
- [72] A. Mycielsky *J. Appl. Phys.* **1988**, 19, 3279.
- [73] A. Twardowski *Diluted Magnetic Semiconductors*; M. Jain, Ed.; p. 276. World Scientific, Singapore **1991**.
- [74] A. Lewicki, A.I. Schindler, J.K. Furdyna, W. Giriat *Phys. Rev. B* **1989**, 40, 2379.
- [75] F. Hamdani, J.P. Lascaray, D. Coquillat, A.K. Bhattacharjee, M. Nawrocki, Z. Golacki *Phys. Rev. B* **1992**, 45, 13298.
- [76] W. Mac, N.T. Khoi, A. Twardowski, J.A. Gaj, M. Demianiuk *Phys. Rev. Lett.* **1993**, 71, 2327.
- [77] T.M. Pekarek, J.E. Luning, I. Miotkowski, B.C. Crooker *Phys. Rev. B* **1994**, 50, 16914.
- [78] G. Bauer *Mater. Res. Soc. Proc.* **1987**, 89, 107.
- [79] A. Lambrecht, N. Herres, B. Spanger, S. Kuhn, H. Bottner, M. Tacke, J. Evers *J. Cryst. Growth* **1991**, 108, 301.
- [80] A. Bruno, J. P. Lascaray, M. Averous, G. Fillion, F. Dumas *Phys. Rev. B* **1988**, 37, 1186.
- [81] R. Boyn *Phys. Status Solidi B* **1988**, 148, 11.
- [82] F.J. Brieler, P. Grundmann, M. Fröba, L. Chen, P.J. Klar, W. Heimbrod, H.-A. Krug von Nidda, T. Kurz, A. Loidl *Eur. J. Inorg. Chem.* **2005**, *accepted*.
- [83] J.K. Furdyna *J. Appl. Phys.* **1988**, 64, R29.
- [84] O. Goede, W. Heimbrod *Phys. Status Solidi B* **1988**, 146, 11.
- [85] J.K. Furdyna, J. Kossut, Eds., *Diluted Magnetic Semiconductors, Semiconductors and Semimetals*; R.K. Willardson, A.C. Beer, Eds.; Vol. 25. Academic Press, San Diego **1988**.
- [86] H. Ohno, F. Matsukura *Solid State Commun.* **2001**, 117, 179.
- [87] H. Ohno *Mater. Sci. Forum* **1995**, 182-184, 443.
- [88] S. Das Sarma, E.H. Hwang, A. Kaminski *Solid State Commun.* **2003**, 127, 99.
- [89] R.N. Bhargava, D. Gallagher, X. Hong, A.V. Nurmikko *Phys. Rev. Lett.* **1994**, 72, 416.
- [90] A.A. Bol, A. Meijerink *Phys. Rev. B* **1998**, 58, R15997.
- [91] A.A. Bol, A. Meijerink *J. Lumin.* **2000**, 87-89, 315.
- [92] D.J. Norris, Nan Yao, F.T. Charnock, T.A. Kennedy *Nanoletters* **2001**, 1, 3.
- [93] M.A. Hines, P. Guyot-Sionnest *J. Phys. Chem. B* **1998**, 102, 3655.

- [94] L. Levy, J.F. Hocheple, M.P. Pileni *J. Phys. Chem.* **1996**, *100*, 18322.
- [95] L. Levy, N. Feltin, D. Ingert, M.P. Pileni *J. Phys. Chem. B* **1997**, *101*, 9153.
- [96] F.J. Brieler, M. Fröba, L. Chen, P.J. Klar, W. Heimbrod, H.-A. Krug von Nidda, A. Loidl *Chem. Eur. J.* **2002**, *8*, 185.
- [97] L. Chen, H. Falk, P.J. Klar, W. Heimbrod, F. Brieler, M. Fröba, H.-A. Krug von Nidda, A. Loidl, Z. Chen, Y. Oka *Phys. Status Solidi B* **2002**, *229*, 31.
- [98] A.V. Kouzema, M. Fröba, L. Chen, P.J. Klar, W. Heimbrod *Adv. Funct. Mater.* **2005**, *15*, 168.
- [99] F.J. Brieler, P. Grundmann, M. Fröba, L. Chen, P.J. Klar, W. Heimbrod, H.-A. Krug von Nidda, T. Kurz, A. Loidl *J. Am. Chem. Soc.* **2004**, *126*, 797.
- [100] L. Chen, P.J. Klar, W. Heimbrod, F. Brieler, M. Fröba, H.-A. Krug von Nidda, T. Kurz, A. Loidl *J. Appl. Phys.* **2003**, *93*, 1326.
- [101] S. Brunauer, P.H. Emmet, E. Teller *J. Am. Chem. Soc.* **1938**, *60*, 309.
- [102] E.P. Barrett, L.G. Joyner, P.P. Halenda *J. Am. Chem. Soc.* **1951**, *73*, 373.
- [103] C. Lastokie, K. E. Gubbins, N. J. Quirke *J. Phys. Chem. B* **1993**, *97*, 4786.
- [104] P.I. Ravikovitch, S.C.O. Domhnaill, A. Neimark, F. Schüth, K.K. Unger, *Langmuir* **1995**, *11*, 4765.
- [105] J.J. Rehr, J. Mustre de Leon, S.I. Zabinsky, R.C. Albers *J. Am. Chem. Soc.* **1991**, *113*, 5135.
- [106] T. Ressler *J. Synchrotron Rad.* **1998**, *5*, 118.
- [107] H. Primas, U. Müller-Herold *Elementare Quantenchemie*, B.G. Teubner, Stuttgart, **1990**.
- [108] K. Schumacher, P.I. Ravikovitch, A. DuChesne, A.V. Neimark, K.K. Unger *Langmuir* **2000**, *16*, 4648.
- [109] A.V. Neimark, P.I. Ravikovitch, M. Grün, F. Schüth, K.K. Unger *J. Colloid Interface Sci.* **1998**, *207*, 159.
- [110] M. Thommes, R. Köhn, M. Fröba *Stud. Surf. Sci. Catal.* **2000**, *128*, 259.
- [111] K.S.W. Sing, D.H. Everett, R.A.W. Haul, L. Moscou, R.A. Pierotti, J. Rouquerol, T. Siemieniowska *Pure & Appl. Chem.* **1985**, *57*, 603.
- [112] S. Inoue, Y. Hanzawa, K. Kaneko *Langmuir* **1998**, *15*, 3608.
- [113] M.W. Maddox, J.P. Olivier, K.E. Gubbins *Langmuir* **1997**, *13*, 1737.
- [114] R. Zana *Colloids Surf. A Physiochem. Eng. Aspects* **1997**, *123*, 27.

- [115] B. Jönsson, B. Lindman, K. Holmberg, B. Kronberg *Surfactants and Polymers in Aqueous Solution*, John Wiley & Sons, Chichester, New York, Weinheim, Brisbane, Singapore, Toronto **1998**.
- [116] M. Janicke, D. Kumar, G.D. Stucky, B.F. Chmelka *Zeolites and Related Microporous Materials: State of the Art*; J. Weitkamp, H.G. Karge, H. Pfeifer, W. Hölderich, Eds.; Elsevier, Amsterdam **1994**.
- [117] W. Hammond, E. Prouzet, S.D. Mahanti, T.J. Pinnavaia *Microporous Mesoporous Mater.* **1999**, 27, 19.
- [118] M. Thommes *Langmuir* **2005**, submitted.
- [119] M. Thommes, R. Köhn, M. Fröba *Appl. Surf. Sci.* **2002**, 196, 239.
- [120] A. Anatassiadou, E. Liarokapis, E. Anastassakis *Solid State Commun.* **1989**, 69, 137.
- [121] E. Jahnke, O. Goede, V. Weinhold *Phys. Status Solidi B* **1988**, 146, K157.
- [122] I.H. Campbell, P.M. Fauchet *Solid State Commun.* **1986**, 58, 739.
- [123] P. Verma, L. Gupta, S.C. Abbi, K.P. Jain *J. Appl. Phys.* **2000**, 88, 4109.
- [124] M. Rajalakshmi, A.K. Arora, B.S. Bendre, S. Mahamuni *J. Appl. Phys.* **2000**, 87, 2445.
- [125] M.L. Curri, A. Agostiano, L. Manna, M. Della Monica, M. Catalano, L. Chiavarone, V. Spagnolo, M. Lugarà *J. Phys. Chem. B* **2000**, 104, 8391.
- [126] *Landolt-Börnstein - Numerical Data and Functional Relationships in Science and Technology*; Vol. 17b, O. Madelung, M. Schulz, H. Weiß, Eds.; Springer, Berlin, Heidelberg, New York **1982**.
- [127] J. Cizeron, M. P. Pileni *J. Phys. Chem. B* **1995**, 99, 17410.
- [128] W. Vogel, J. Urban, M. Kundu, S. K. Kulkarni *Langmuir* **1997**, 13, 827.
- [129] L. Chen, P.J. Klar, W. Heimbrod, F. Brieler, M. Fröba, H.-A. Krug von Nidda, A. Loidl *Physica E* **2001**, 10, 368.
- [130] O. Goede, W. Heimbrod, V. Weinhold *Phys. Status Solidi B* **1986**, 136, K49.
- [131] W. Heimbrod, C. Benecke, O. Goede, H.-E. Gumlich *Phys. Status Solidi B* **1989**, 154, 405.
- [132] D. Theis *Phys. Status Solidi B* **1967**, 79, 125.
- [133] O. Goede, W. Heimbrod, M. Lamla, V. Weinhold *Phys. Status Solidi B* **1989**, 146, K65.

- [134] F.J. Brieler, P. Grundmann, M. Fröba, L. Chen, P.J. Klar, W. Heimbrod, H.-A. Krug von Nidda, T. Kurz, A. Loidl *Chem. Mater.* **2004**, *17*, 795.
- [135] Y. Tanabe, S.J. Sugano *J. Phys. Soc. Jpn.* **1954**, *9*, 753.
- [136] A. Twardowski, P. Swiderski, M. von Ortenberg, R. Pauthenet *Solid State Commun.* **1984**, *50*, 509.
- [137] A. Twardowski, T. Dietl, M. Demianiuk *Solid State Commun.* **1983**, *48*, 845.
- [138] C.T. Tsai, S.H. Chen, D.S. Chuu, W.C. Chou *Phys. Rev. B* **1996**, *33*, 8207.
- [139] M. Ikeda, K. Itoh, H. Sato *J. Phys. Soc. Jpn.* **1968**, *25*, 455.
- [140] R.B. Bylisma, W.M. Becker, J. Kossut, U. Debska *Phys. Rev. B* **1986**, *33*, 8207.
- [141] B.E. Larson, K.C. Hass, H. Ehrenreich, A.E. Carlson *Phys. Rev. B* **1988**, *37*, 4137.
- [142] M. Taniguchi, M. Fujimori, M. Fujisawa, T. Mori, I. Souma, Y. Oka *Solid State Commun.* **1987**, *62*, 431.
- [143] R. Weidemann, H.-E. Gumlich, M. Kupsch, H.-U. Middelmann, U. Becker *Phys. Rev. B* **1992**, *45*, 1172.
- [144] Y.R. Lee, A.K. Ramdas, R.L. Aggarwal *Proc. 18th Int. Conf. on Physics of Semiconductors*, World Scientific **1986**.
- [145] D. Theis *Phys. Lett. A* **1976**, *59*, 154.
- [146] U. Stutenbäumer, H.E. Gumlich, H. Zuber *Phys. Status Solidi B* **1989**, *156*, 561.
- [147] D. Leinen *Phys. Rev. B* **1997**, *55*, 6975.
- [148] D. Some, A.V. Nurmikko *Phys. Rev. B* **1993**, *48*, 4418.
- [149] H. Waldmann, C. Bennecke, W. Busse, H.E. Gumlich, A. Krost *Semicond. Sci. Technol.* **1989**, *4*, 71.
- [150] W. Busse, H.-E. Gumlich, B. Meissner, D. Theis *J. Lumin.* **1976**, *12-13*, 693.
- [151] U. Pohl, H.-E. Gumlich *Phys. Rev. B* **1989**, *40*, 1194.
- [152] O. Goede, W. Heimbrod, D.D. Thong *Phys. Status Solidi B* **1984**, *126*, K159.
- [153] D.L. Dexter *J. Chem. Phys.* **1953**, *21*, 836.
- [154] K. Yan, C. Duan, Y. Ma, S. Xia, J.-C. Krupa *Phys. Rev. B* **1998**, *58*, 13585.
- [155] M. Tanaka, J. Qi, and Y. Masumoto *J. Lumin.* **2000**, *87-89*, 472.
- [156] R.R. Galazka, S. Nagata, P.H. Keesom *Phys. Rev. B* **1980**, *22*, 3344.
- [157] M.A. Novak, O.G. Symko, D.J. Zheng, S. Oseroff *Phys. Rev. B* **1986**, *33*, 6391.
- [158] N. Samarth, J.K. Furdyna *Phys. Rev. B* **1988**, *37*, 9227.
- [159] J. Schneider, S.R. Sircar, A.Z. Räuber *Z. Naturforsch. A* **1963**, *18*, 980.
- [160] J. Lambe, C. Kikuchi *Phys. Rev. B* **1960**, *119*, 1256.

- [161] Y.J. Ishikawa *J. Phys. Soc. Jpn.* **1966**, *21*, 1473.
- [162] S. Kuroda, Y. Terai, K. Takita, T. Okuno, Y. Masumoto *J. Cryst. Growth* **1998**, *184-185*, 971.
- [163] D.M. Hofmann, A. Hofstaetter, U. Leib, B.K. Meyer, C. Cunnio *J. Cryst. Growth* **1998**, *184-185*, 383.
- [164] O. Goede, D. Backs, W. Heimbrod, M. Kanis *Phys. Status Solidi B* **1989**, *151*, 311.
- [165] J.K. Furdyna, N. Samarth, R.B. Frankel, J. Spalek *Phys. Rev. B* **1988**, *37*, 3707.
- [166] C. Chen, M. Qu, W. Hu, X. Zhang, F. Lin, H. Hu, K. Ma, W. Giriat *J. Appl. Phys.* **1991**, *69*, 6114.
- [167] Y.Q. Yang, P.H. Keesom, J.K. Furdyna, W. Giriat *J. Solid State Chem.* **1983**, *49*, 20.
- [168] Y. Shapira S. Foner, D. Heiman, P.A. Wolff, C.R. McIntyre *Solid State Commun.* **1989**, *71*, 355.
- [169] R.E. Kremer, J.K. Furdyna *Phys. Rev. B* **1985**, *31*, 1.
- [170] S.B. Oseroff *Phys. Rev. B* **1982**, *25*, 6584.
- [171] H.A. Sayad, S.M. Bhagat *Phys. Rev. B* **1985**, *31*, 591.
- [172] S.B. Oseroff, R. Calvo, Z. Fisk, F. Acker *Phys. Lett. A* **1980**, *80*, 311.
- [173] B.E. Larson, H. Ehrenreich *Phys. Rev. B* **1989**, *39*, 1747.
- [174] J.H. van Vleck *Phys. Rev.* **1948**, *74*, 1168.
- [175] P.W. Anderson, P.R. Weiss *Rev. Mod. Phys.* **1953**, *25*, 269.
- [176] K. Kawasaki *Prog. Theo. Phys.* **1968**, *39*, 285.
- [177] H. Mori, K. Kawasaki *Prog. Theo. Phys.* **1962**, *28*, 971.
- [178] D.L. Huber *Phys. Rev. B* **1972**, *6*, 3180.
- [179] S. Maekawa *J. Phys. Soc. Jpn* **1972**, *33*, 573.
- [180] W. Heimbrod, C. Benecke, O. Goede, H.-E. Gumlich *Phys. Status Solidi B* **1989**, *154*, 405.
- [181] W. Heimbrod, C. Benecke, O. Goede, H.-E. Gumlich *J. Cryst. Growth* **1990**, *101*, 911.
- [182] M.S. Seehra, R.D. Groves *J. Phys. C: Solid State Phys.* **1983**, *16*, L411.

Thanks

First of all I would like to thank *Prof. Dr. Michael Fröba* for the opportunity to work in his group (in Hamburg and in Gießen) and his supervision and continuous support over the last five years.

Also thanks to all the members of the group in Hamburg and Gießen for the wonderful working conditions and the coffee breaks: *Maximilian Cornelius, Dr. Wolfgang Herrendorf, Dr. Frank Hoffmann, Holger Huwe, Dr. Daniela Kempe, Andreas Lotz, Dr. Ralf Köhn, Jürgen Morell, Sven Kroker, Dr. Olaf Muth, Dr. Nadine Oberender, Vivian Rebbin, Jan Roggenbuck, Uta Sazama, Dr. Michael (Mike) Serafin, Tamara Stumpf and Dr. Michael Tiemann.*

Special thanks to *Petra Grundmann* for her helping hand in the laboratory and to *Günther Koch* for the long hours at the TEM.

This work was financially supported by *Deutsche Forschungsgemeinschaft (DFG)* in the priority programme "*Semiconductor and Metal Clusters as Building Blocks for Organized Structures*" (Fr 1372/4-3).

For their collaboration I would like to thank:

- *Dr. Limei Chen, Martin Güngerich, Dr. Peter J. Klar and Prof. Dr. Wolfram Heimbrod*t from the material science centre at Philipps University in Marburg for all the photoluminescence measurements and the continuous willingness to answer all my "chemist-questions".

- *Thomas Kurz, Dr. Hans-Albrecht Krug von Nidda* and *Prof. Dr. Alois Loidl* from University of Augsburg for the EPR and magnetic measurements.
- *Dr. Matthias Thommes* from Quantachrome Instruments, Florida, for the helpful discussions on sorption phenomena and their interpretation.

Personal thanks go to very different person for various reasons: The whole *Bergedorfer Kammerchor*, *Carsten Brandt*, *Per Breuer*, *Matt Groening*, *Kristin Håkansson*, *Benjamin Hinrichs* and to *Kadda*!

Very special thanks to my family, in particular:

My brother *Philipp* for his never dying interest in my "funny work".

My grandfather *Dr. Adolf Schmidt*, who really started it all – although unfortunately he never lived to see it.

And last but not least, my parents *Dr. Gisela* and *Prof. Dr. Sigurd Brieler* for their believe in my abilities, the constant support even in hard times and the always open ear and door to feel at home.

Full list of publications

Contribution in books

Modified magnetic properties of paramagnetic (Zn,Mn)S at reduced dimensions
P.J. KLAR, L. CHEN, W. HEIMBRODT, F.J. BRIELER, M. FRÖBA, T. KURZ, H.-A. KRUG VON NIDDA, A. LOIDL
in: B. Kramer (Ed.) *Advances in Solid State Physics*, Vol. 44, p. 491-502, Springer-Verlag, Berlin Heidelberg, **2004** (ISBN: 3-540-21148-9)

Peer-reviewed paper

Towards ordered arrays of magnetic semiconductor quantum wires
L. CHEN, P.J. KLAR, W. HEIMBRODT, F. BRIELER, M. FRÖBA
Appl. Phys. Lett. **2000**, 76, 3531-3533.

Magneto-spectroscopy of ordered arrays of magnetic semiconductor quantum wires
L. CHEN, P.J. KLAR, W. HEIMBRODT, F. BRIELER, M. FRÖBA, H.-A. KRUG VON NIDDA, A. LOIDL
Physica E **2001**, 10, 368-372.

Ordered Arrays of II/VI Diluted Magnetic Semiconductor Quantum Wires: Formation within mesoporous MCM-41 Silica
F. BRIELER, M. FRÖBA, L. CHEN, P.J. KLAR, W. HEIMBRODT, H.-A. KRUG VON NIDDA, A. LOIDL
Chem. Eur. J. **2002**, 8, 185-194.

Modification of the Magnetic and Electronic Properties of Ordered Arrays of (II,Mn)VI Quantum Wires Due to Reduced Lateral Dimensions
L. CHEN, H. FALK, P.J. KLAR, W. HEIMBRODT, F. BRIELER, M. FRÖBA, H.-A. KRUG VON NIDDA, A. LOIDL, Z. CHEN, Y. OKA
Phys. Stat. Sol. **2002**, 229, 31-34.

Regular Arrays of (Zn,Mn)S quantum wires with Well-Defined Diameters in the Nanometer Range
L. CHEN, P.J. KLAR, W. HEIMBRODT, F.J. BRIELER, M. FRÖBA
J. Supercond. **2003**, 16, 99-102.

Arrays of (Zn,Mn)S quantum wires with well-defined diameters below 10 nm
L. CHEN, P.J. KLAR, W. HEIMBRODT, F.J. BRIELER, M. FRÖBA, H.-A. KRUG VON NIDDA, T. KURZ, A. LOIDL
J. Appl. Phys. **2003**, 93, 1326-1328.

Formation of $\text{Zn}_{1-x}\text{Mn}_x\text{S}$ Nanowires within Mesoporous Silica of Different Pore Sizes
F.J. BRIELER, P. GRUNDMANN, M. FRÖBA, L. CHEN, P.J. KLAR, W. HEIMBRODT, H.-A. KRUG VON NIDDA, T. KURZ, A. LOIDL
J. Am. Chem. Soc. **2004**, 126, 797-807.

Size Dependence of the Magnetic and Optical Properties of $\text{Cd}_{1-x}\text{Mn}_x\text{S}$ Nanostructures Confined in Mesoporous Silica

F.J. BRIELER, P. GRUNDMANN, M. FRÖBA, L. CHEN, P.J. KLAR, W. HEIMBRODT, H.-A. KRUG VON NIDDA, T. KURZ, A. LOIDL
Chem. Mater. **2005**, *17*, 795-803.

Nanostructured Diluted Magnetic Semiconductors

F.J. BRIELER, P. GRUNDMANN, M. FRÖBA, L. CHEN, P.J. KLAR, W. HEIMBRODT, H.-A. KRUG VON NIDDA, T. KURZ, A. LOIDL
Eur. J. Inorg. Chem. **2005**, *accepted*.

Conference proceedings

Ternary transition metal oxides within mesoporous MCM-48 silica phases: Synthesis and characterization

R. KÖHN, F. BRIELER, M. FRÖBA
Stud. Surf. Sci. Catal. **2000**, *129*, 341-348.

MCM-41 silica monoliths and diluted magnetic semiconductors: a promising union for fabricating nanosized quantum wires

F. BRIELER, M. BREHM, L. CHEN, P.J. KLAR, W. HEIMBRODT, M. FRÖBA
Stud. Surf. Sci. Catal. **2001**, *135*, 21-O-03.

Synthesis Of Manganese Doped II/VI Semiconductor Quantum Wires Within Mesoporous Silica Matrices With Different Pore Diameters

F.J. BRIELER, P. GRUNDMANN, L. CHEN, P.J. KLAR, W. HEIMBRODT, H.-A. KRUG VON NIDDA, T. KURZ, A. LOIDL, M. FRÖBA
Proc. 14th Internat. Zeolite Conf., **2004**, 342-343 (ISBN: 0-958-46636-X).

Reports and extended abstracts

Characterization of ternary transition metal oxides within mesoporous MCM-48 silica by XANES/EXAFS

R. KÖHN, F. BRIELER, M. FRÖBA
Hamburger Synchrotronstrahlungslabor (HASYLAB), Annual Report **1999**, 767-768.

Characterization of nanostructured semimagnetic semiconductors by XANES/EXAFS

F. BRIELER AND M. FRÖBA
Hamburger Synchrotronstrahlungslabor (HASYLAB), Annual Report **2000**, 757-758.

In situ SAXS studies on the template-directed synthesis of the SBA-15 and periodic mesoporous organosilicas (PMOs)

V. REBBIN, F. BRIELER, S.S. FUNARI, M. FRÖBA
Hamburger Synchrotronstrahlungslabor (HASYLAB), Annual Report **2001**, 643-644.

Hybrid structures of (II,Mn)VI semiconductors within mesoporous silica: Characterization by XANES and EXAFS

F. BRIELER AND M. FRÖBA
Hamburger Synchrotronstrahlungslabor (HASYLAB), Annual Report **2001**, 759-760.

Manganese coordination of nanostructured $\text{Zn}_{1-x}\text{Mn}_x\text{S}$ within mesoporous MCM-41 matrices

F.J. BRIELER, M. FRÖBA

Hamburger Synchrotronstrahlungslabor (HASYLAB), Annual Report 2002, 329-330.

EXAFS Investigations of the Local Structure of Mn^{2+} inside Nanostructured $\text{Zn}_{1-x}\text{Mn}_x\text{S}$

F.J. BRIELER, M. FRÖBA

Hamburger Synchrotronstrahlungslabor (HASYLAB), Annual Report 2003, 289-290.

Poster presentations

Nanostrukturierte II/VI Halbleiterverbindungen in mesoporösen MCM-41-Silicaphasen

F. BRIELER, M. FRÖBA, L. CHEN, P.J. KLAR, W. HEIMBRODT

DFG-SPP Meeting "Semiconductor and Metal Clusters as Building Blocks for Organized Structures", Kochel (Germany), March 12-14, **2000**.

Type II-VI Diluted Magnetic Semiconductors (DMS) within Mesoporous M41S Silica Phases: Synthesis and Characterization

F. BRIELER, L. CHEN, P.J. KLAR, W. HEIMBRODT

2nd Conference on Access in Nanoporous Materials, Banff (Canada), May 25-30, **2000**.

Diluted Magnetic Semiconductor Quantum Wires

F. BRIELER, M. FRÖBA, L. CHEN, P.J. KLAR, W. HEIMBRODT

International Conference Solid State Chemistry 2000, Prague (Czech Republic), September 3-8, **2000**.

Diluted Magnetic Semiconductor Quantum Wires

F. BRIELER, M. FRÖBA, L. CHEN, P.J. KLAR, W. HEIMBRODT

Drittes Norddeutsches Doktoranden Kolloquium, Hamburg (Germany), October 5-6, **2000**.

Geordnete semimagnetische Halbleiternanostrukturen: Synthese und Charakterisierung

F. BRIELER, M. FRÖBA, L. CHEN, P.J. KLAR, W. HEIMBRODT

DFG-SPP Meeting "Semiconductor and Metal Clusters as Building Blocks for Organized Structures", Kochel (Germany), October 29-31, **2000**.

Characterisation of Nanostructured Semimagnetic II/VI Semiconductors by XANES and EXAFS

F. BRIELER, M. FRÖBA

HasyLab Users Meeting 2000, Hamburg (Germany), January 26, **2001**.

Utilisation of MCM-41 Silica for the Formation of II/VI Semiconductor Quantum Wires

F. BRIELER, L. CHEN, P.J. KLAR, W. HEIMBRODT

13th German Zeolithe Conference, Erlangen-Nuremberg (Germany), March 7-9, **2001**.

Hybridstrukturen aus Halbleitern in mesoporösen Silicaten: Synthese, Charakterisierung und magnetische Eigenschaften

F. BRIELER, M. FRÖBA, L. CHEN, P.J. KLAR, W. HEIMBRODT

DFG-SPP Meeting "Semiconductor and Metal Clusters as Building Blocks for Organized Structures", Kochel (Germany), October 21-23, **2001**.

Hybrid Structures of (II,Mn)VI Semiconductors within Mesoporous Silica: Characterisation by XANES and EXAFS

F. J. BRIELER, M. FRÖBA

Hasylab Users Meeting 2001, Hamburg (Germany), January 25, **2002**.

Ordered Arrays of Nanostructured (II,Mn)VI Semiconductors: Formation within Mesoporous Silica

F.J. BRIELER, M. FRÖBA

Spring Meeting Material Research Society, San Francisco (USA), April 1-5, **2002**.

Synthese nanostrukturierter (II,Mn)VI Halbleiter: Bildung in den Poren mesoporöser Silicate

F. BRIELER, M. FRÖBA, L. CHEN, P.J. KLAR, W. HEIMBRODT

DFG-SPP Meeting "Semiconductor and Metal Clusters as Building Blocks for Organized Structures", Kochel (Germany), October, **2002**.

Manganese Coordination of Nanostructured (II,Mn)S Diluted Magnetic Semiconductors within Mesoporous Silica Matrices

F. J. BRIELER, M. FRÖBA

Hasylab Users Meeting 2002, Hamburg (Germany), January 31, **2003**.

Formation of Nanowires of $\text{Zn}_{1-x}\text{Mn}_x\text{S}$ inside Mesoporous Silica

F.J. Brieler, M. Fröba

15th German Zeolithe Conference, Kaiserslautern (Germany), March 5-7, **2003**.

Synthese von $\text{Zn}_{1-x}\text{Mn}_x\text{S}$ Nanodrähten in mesoporösen Silicas unterschiedlicher Porengröße

F. BRIELER, M. FRÖBA, L. CHEN, P.J. KLAR, W. HEIMBRODT

DFG-SPP Meeting "Semiconductor and Metal Clusters as Building Blocks for Organized Structures", Kochel (Germany), October 26-28, **2003**.

Oral presentations

MCM-41 Silica Monoliths and Diluted Magnetic Semiconductors: A Promising Union for Fabricating Nanosized Quantum Wires

F. BRIELER

13th International Zeolite Conference, Montpellier (France), July 8-13, **2001**.

Porous Materials in Host/Guest Chemistry – Synthesis and Characterisation

F. BRIELER

invited talk at the department of physics, Philipps university of Marburg, Marburg (Germany), April 25, **2002**.

Charakterisierung poröser Festkörper mittels Physisorption

F. BRIELER

DFG workshop for members of the DFG-SPP *"Semiconductor and Metal Clusters as Building Blocks for Organized Structures"*, Blaubeuren (Germany), May 10-12, **2002**.

Synthesis of Manganese Doped II/VI Semiconductor Quantum Wires within Mesoporous Silica Matrices

F.J. BRIELER, M. FRÖBA, P.J. KLAR, L. CHEN, W. HEIMBRODT

16th German Zeolite Conference, Dresden (Germany), March 5-7, **2003**.

Synthesis of Manganese Doped II/VI Semiconductor Quantum Wires within Mesoporous Silica Matrices

F.J. BRIELER, M. FRÖBA, P.J. KLAR, L. CHEN, W. HEIMBRODT

14th International Zeolite Conference, Cape Town (South Africa), April 25-30, **2004**.

Size Dependence of the Physical Properties of Nanostructured Manganese Doped II/VI Semiconductors

F.J. BRIELER, M. FRÖBA, P.J. KLAR, L. CHEN, W. HEIMBRODT

4th International Mesostructured Materials Symposium, Cape Town (South Africa), May 1-4, **2004**.

Curriculum vitae

Felix Brieler, born February 15, 1975 in Kiel, Germany.

1981 - 1984	Elementary school <i>Hardenberg Grundschule</i> in Kiel
1984 - 1985	Elementary school <i>Katholische Grundschule Bergedorf</i> in Hamburg
1985 - 1994	Grammar school <i>Hansa-Gymnasium</i> in Hamburg
May 1994	<i>Abitur</i>
Oct. 1994 – Feb. 2000	Study of Chemistry at <i>Universität Hamburg</i>
Sept. 1996	<i>Diplomvorprüfung</i>
Apr. - May 1998	Guest study at <i>Exeter University</i> , Great Britain (inorganic chemistry research project in the group of Prof. Dr. Robert C.T. Slade)
June 1999 - Feb. 2000	Work on Diploma thesis " <i>Nanostrukturierte II-VI Halbleiterverbindungen in mesoporösen M41S Silicaphasen</i> " in the group of Prof. Dr. Michael Fröba at <i>Universität Hamburg</i>
Feb. 2000	<i>Diplom</i> in Chemistry at <i>Universität Hamburg</i>
Mar. 2000 - Mar. 2001	Work on <i>Dissertation</i> (PhD thesis) " <i>Nanostructured Diluted Magnetic Semiconductors within Mesoporous Silica</i> " in the group of Prof. Dr. Michael Fröba at <i>Universität Hamburg</i>
Apr. 2001 - June 2005	continued work on <i>Dissertation</i> (PhD thesis) in the group of Prof. Dr. Michael Fröba at <i>Justus-Liebig-Universität Gießen</i>
Mar. 2000 – Apr. 2001	employed as Scientific Assistant at <i>Universität Hamburg</i> , founded by <i>Deutsche Forschungsgemeinschaft</i>
Mar. 2001 - Dec. 2004	employed as Scientific Assistant at <i>Justus-Liebig-Universität Gießen</i> , founded by <i>Deutsche Forschungsgemeinschaft</i>

Hazardous chemicals

Information on potential hazards caused by the chemicals used in this work according to the European Union classification.

compound	hazard category ¹	R phrase ²	S phrase ³
cadmium acetate dihydrate	Xn	20/21/22	22
cadmium sulphide	T	45-46- 20/21/22- 36/37/38	26-36/37/39- 45
hexadecyltrimethyl ammoniumbromide	Xn, N	22-36/38	26-39-61
hydrochloric acid	C	34-37	26-36/37/39- 45
hydrogen selenide	T ⁺ , F ⁺	12-26	1-9-16-33-36- 45
hydrogen sulphide	T ⁺ , F ⁺ , N	12-26-50	9-16-28- 36/37-45-61
manganese sulphide		36/37/38	26-36
tetraethyl orthosilicate	Xi	10-20-36/37	
tetramethyl ammoniumhydroxide	T	25-34	26-36/37/38- 45
zinc acetate dihydrate			24/25

¹ C: corrosive; F⁺: extremely flammable; Xi: irritant; Xn: harmful to health; N: dangerous for the environment; T: toxic; T⁺: highly toxic.

² R10: flammable; R12: explosive when mixed with oxidizing substances; R20: harmful by inhalation; R21: harmful in contact with skin; R22: harmful if swallowed; R25: toxic if swallowed; R26: very toxic by inhalation; R34: causes burns; R36: irritating to eyes; R37: irritating to respiratory system; R38: irritating to skin; R45: may cause cancer; R46: may cause heritable genetic damage; R50: very toxic to aquatic organisms.

³ S1: keep locked up; S9: keep container in a well-ventilated place; S16: keep away from sources of ignition; S22: do not breathe dust; S24: avoid contact with skin; S25: avoid contact with eyes; S26: in case of contact with eyes, rinse immediately with plenty of water and seek medical advice; S28: after contact with skin, wash immediately with plenty of ... (to be specified by the manufacturer); S33: take precautionary measures against static discharges; S36: wear suitable protective clothing; S37: wear suitable gloves; S38: in case of insufficient ventilation, wear suitable respiratory equipment; S39: wear eye/face protection; S45: in case of accident or if you feel unwell, seek medical advice immediately (show the label where possible); S61: avoid release to the environment. Refer to special instructions/safety data sheets.